

FEDERAL UNIVERSITY OF ESPÍRITO SANTO
TECHNOLOGY CENTER
GRADUATE PROGRAM IN ELECTRICAL ENGINEERING

FELIPE BRITTO AZEVEDO SCHNEIDER

**ASSESSMENT OF GLOBAL ORIENTATION ESTIMATION USING REDUNDANT
INERTIAL AND MAGNETIC SENSORS**

Vitória/Brazil

2018

FELIPE BRITTO AZEVEDO SCHNEIDER

**ASSESSMENT OF GLOBAL ORIENTATION ESTIMATION USING REDUNDANT
INERTIAL AND MAGNETIC SENSORS**

Dissertation submitted to the Graduate Program in Electrical Engineering (PPGEE) from the Technology Center of the Federal University of Espírito Santo, as a partial requirement for obtaining Master's Degree in Electrical Engineering.

Supervisor: Prof. Dr. Anselmo Frizera Neto

Co-supervisor: Prof. Dr. Patrick Marques Ciarelli

Vitória/Brazil

2018

Dados Internacionais de Catalogação-na-publicação (CIP)
(Biblioteca Setorial Tecnológica,
Universidade Federal do Espírito Santo, ES, Brasil)

S358a Schneider, Felipe Britto Azevedo, 1990-
Assessment of global orientation estimation using redundant
inertial and magnetic sensors / Felipe Britto Azevedo Schneider.
– 2018.
90 f. : il.

Orientador: Anselmo Frizera Neto.
Coorientador: Patrick Marques Ciarelli.
Dissertação (Mestrado em Engenharia Elétrica) –
Universidade Federal do Espírito Santo, Centro Tecnológico.

1. Sistemas microeletromecânicos. 2. Multisensor para fusão
de dados. 3. Unidade de medição inercial (IMU). 4. Sensores
inerciais. 5. Estimação da orientação. I. Frizera Neto, Anselmo.
II. Ciarelli, Patrick Marques. III. Universidade Federal do Espírito
Santo. Centro Tecnológico. IV. Título.

CDU: 621.3

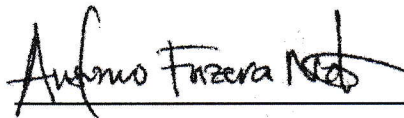
FELIPE BRITTO AZEVEDO SCHNEIDER

**ASSESSMENT OF GLOBAL ORIENTATION ESTIMATION USING REDUNDANT
INERTIAL AND MAGNETIC SENSORS**

Dissertation submitted to the Graduate Program in Electrical Engineering (PPGEE) from the Technology Center of the Federal University of Espírito Santo, as a partial requirement for obtaining Master's Degree in Electrical Engineering.

Committee:

Date: September 6th, 2018



Prof. Dr. Anselmo Frizera Neto

Supervisor. Graduate Program in Electrical Engineering, Federal University of Espírito Santo



Prof. Dr. Patrick Marques Ciarelli

Co-supervisor. Graduate Program in Electrical Engineering, Federal University of Espírito Santo



Prof. Dr. Evandro O. Teatini Salles

Graduate Program in Electrical Engineering, Federal University of Espírito Santo



Prof. Dr. Luiz Eduardo Rodrigues Cheu

Department of Biomedical Engineering, Escuela Colombiana de Ingeniería

Vitória, Brazil

2018

ACKNOWLEDGMENTS

A work of this size is never achieved alone. There are always important people and something else, that I like to name as God that helps the author to reach the finishing line.

Therefore, I would like to thank God for the opportunity to be healthy, alive and in conditions to complete this work.

I must say infinite thanks to my parents, Mauro and Carmen, they gave me much more than I would possibly be able to appreciate. You are a great part of who I am. I also must thank my brother, Flávio, and my sister, Mariana, who always loved me and supported me; you made my life much happier.

A very special person throughout this process is my partner Juliana. Thank you for being by my side, giving me a great love and wisdom, sharing not only the good moments but helping me through the bad ones. The feeling of gratitude extends to my parents-in-law Adalberto e Marli.

I also would like to thank the all Neurony team for, basically, financing this research. Thank you also for the valuable hours that you guys have provided to me. Additionally, I must say that the PPGEE-Ufes (Graduated Program in Electrical Engineering), NTA (*Núcleo de Tecnologia Assistiva*) and the *Núcleo de Engenharia e Inovação em Telessaúde e Telerreabilitação* (FAPES process 80605893) have all largely collaborated to this work, and, for that, I am grateful.

Finally, I would like to thank my advisors Dr. Anselmo Frizera Neto and Patrick Marques Ciarelli for the valuable guidance that has taken me to this point. Additionally, I would like to say thanks to Laura, my laboratory partner and third reader of this work, for her patient, knowledge and help.

You cannot prevent the birds of sadness from passing over your head, but you can prevent their making a nest in your hair.

Chinese proverb.

ABSTRACT

Inertial Measurements Units based on microelectromechanical technologies are extensively used in a vast range of applications due mainly to their reduced size, weight, power consumption and cost. However, the accuracy of the systems that rely on this technology is still the main hampering factor to its broad adoption.

When it comes to global orientation estimation, the number of factors that play an important role in the final accuracy rise. It is possible to identify five important factors: sensor bias, sensor noise, algorithm robustness and tuning, and for the last, system bandwidth.

Therefore this M.Sc. Dissertation details the development of a system with sensor redundancy, aiming to study the relation between inertial and magnetic data proveniente from different sensors, and finally, resulting in an improvement of the orientation estimation accuracy. Five different fusion algorithms were adapted and implemented, having also their parameters properly optimized. Additionally, a two degrees of freedom orientation system is developed and implemented to be used as orientation reference.

The performed tests were also camera recorded for ease of visualization, the videos are available online. The results are presented in terms of Kinematic Tracking Error and angle Root Mean Square Error (RMSE). The proposed system was able to reach orientation errors as low as 1.05° RMS for the yaw axis during static tests (the yaw axis usually presents the highest RMS error), while dynamic experiments showed results as low as 1.17° , 2.30° and 3.03° RMS, respectively, for what has been classified as Slow, Mid and Fast movement profile.

Furthermore, it is presented the hardware project of a semi-commercial system, which would be able to overcome the main issues presented by the actual system, what would be able to promote new researches.

Keywords: IMU, MARG, MIMU, AHRS, Data Fusion Methods, Orientation Estimation.

RESUMO

Unidades de Medição Inercial baseadas no princípio construtivo dos microeletromecânicos são extensivamente utilizadas em uma vasta gama de aplicações, tal fato se deve principalmente as suas reduzidas dimensões, peso e consumo energético. No entanto, a precisão dos sistemas baseados em componentes microeletromecânicos ainda constitui o principal empecilho para a ampla adoção destes sistemas.

Tratando-se de sistemas de orientação global, o número de fatores que diretamente influenciam a acurácia final aumenta. Deve-se destacar cinco: bias e ruído dos sensores, ajuste e robustez do algoritmo utilizado para fundir os dados inerciais e magnéticos, e por último, resposta em frequência do sistema.

Esta Dissertação de Mestrado detalha o desenvolvimento de um sistema com sensoriamento redundante, objetivando estudar a relação de dados inerciais e magnéticos provenientes de diferentes sensores, o que finalmente resulta em um ganho da precisão da estimação da orientação do sistema. Cinco diferentes métodos de fusão foram adaptados e implementados, tendo, inclusive, seus parâmetros propriamente otimizados. Adicionalmente, uma jiga de testes com dois graus de liberdade foi desenvolvida e utilizada como referência de orientação.

Com o objetivo de facilitar a visualização, os testes foram gravados e os vídeos estão disponíveis online. Os resultados são apresentados em *Kinematic Tracking Error* e *Root Mean Square Error* (RMSE). O sistema proposto foi capaz de alcançar erros na ordem de $1,05^\circ$ RMS para o eixo *yaw* (o qual normalmente apresenta maior erro RMS dentre todos os eixos) durante testes estáticos. Testes dinâmicos, previamente classificados em três diferentes perfis de velocidade (baixo, médio e alto), demonstraram, respectivamente, erros tão baixos quanto $1,17^\circ$, $2,30^\circ$ e $3,03^\circ$ RMS.

Ademais, é apresentado o projeto de *hardware* de um sistema semicomercial, o qual seria capaz de superar os principais problemas apresentados pelo sistema atualmente utilizado, promovendo novas pesquisas.

LIST OF FIGURES

Figure 1: Eric Severaid and Stark Draper observe Spire Jr. gimbals on flight from Massachusetts to California, March 7,1958. (Source: C. S. Draper, 1981 [37]).	26
Figure 2: Scale factor stability (i.e., the accuracy of the gyroscope in monitoring the sensed angular velocity), expressed in parts per million (ppm), as a function of the bias stability (intrinsically dependent on the gyroscope technology) for Mechanical Gyroscopes, Ring Laser Gyroscopes (RLG), Interferometric Fiber-Optic gyroscopes (IFOG), Quartz, Dynamically Tuned Gyroscopes (DTG), Rate and Integrating Gyroscopes and MEMS. (Source: Passaro et al., 2017 [1]).	27
Figure 3: Illustration of commercial AHRS and MEMS sensors. a) TechIMU V4, b) MTi-3, c) MTi-30 or MTi-300, d) UM7-LT, e) AHRS380ZA, f) STT-IWS, g) AHRS-8, h) ADIS16490 and i) Minimu v5.	35
Figure 4: Illustration of the RIMU v1 PCB. Top trails are represented in red color while bottom trails are in green. Blue lines represent top silkscreen. Copper (bottom GND and top 3.3V) zones are hidden.	40
Figure 5: RIMU v1 module illustration highlighting the sensors and external communication port.	40
Figure 6: Test Jig (left) and Test Jig Control Board (right)	42
Figure 7: TJ orientation during the DFMs evaluation experiments. The final DFM output will be truncated between -90 and 90° for Roll and -180 to 180° for Pitch and Yaw. The truncation was not performed to facilitate the scenarios comparison.	46
Figure 8: TJ angular speed during the DFMs evaluation experiments.	46
Figure 9: TJ-RIMU alignment and synchronization process flowchart.	48
Figure 10: Excitation data for the Yaw-alignment process.	50
Figure 11: Orientation-dependent misalignment as function of TJ Yaw orientation. Each vertical coordinate of the plots represents the respective orientation error. The red line represents the fourth order fit while the red dashed line represents the 95% confidence intervals.	50
Figure 12: Relative TJ speed error over its all speed range.	51
Figure 13: Setup of the experiment to evaluate the influence of the motors over the magnetometer readings.	53
Figure 14: Magnetometer readings with average removed, a lower resolution of BNO magnetometer can be noticed. The coordinate axes are dimensionless. Minimu represents the LIS magnetometer.	53
Figure 15: Gyroscope measurements during the vibration evaluation test.	55

Figure 16: Accelerometer measurements during the vibration evaluation test.	55
Figure 17: Kinematic Tracking Error as function of each optimizable parameter for their respective data input scenarios (1 to 8) for the Slow-range profile.	58
Figure 18: DFM performances for the Slow-range motion profile using as input the data composition according to scenario 8. Euler angles represented in the zxy rotation order.	59
Figure 19: Deviations from the reference for each DFM for the Slow-range motion profile using as input the data composition according to scenario 8.	60
Figure 20: Error boxplot distribution for each DFM axes considering the Slow-range profile as IDS. A total of 7500 samples are represented in each axis of each DFM.	60
Figure 21: Comparison of estimated pitch by the system proposed by Alam et al. (Source: Alam et al. 2014 [58]).	61
Figure 22: Kinematic Tracking Error as function of each optimizable parameter for their respective data input scenarios (1 to 8) for the Mid-range profile.	63
Figure 23: DFM performances for the Mid-range motion profile using as input the data composition according to scenario 8. Orange zone is zoomed-in and exhibited in Figure 24. Euler angles represented in the zxy rotation order.	63
Figure 24: Zoom of orange zone exhibited in Figure 23. In detail the difference between the TJ's reference (solid blue) and the BNO (orange dashed) estimation during TJ rotation.	64
Figure 25: Deviations from the reference for each DFM for the Mid-range motion profile using as input the data composition according to scenario 8.	65
Figure 26: Error Boxplot distribution for each DFM axes considering the Mid-range profile as IDS. A total of 7000 samples are represented in each axis of each DFM.	65
Figure 27: Kinematic Tracking Error as function of each optimizable parameter for their respective data input scenarios (1 to 8) using as IDS the Fast-range profile.	67
Figure 28: DFM performances for the Fast-range motion profile using as input the data composition according to scenario 8. Euler angles represented in the zxy rotation order.	68
Figure 29: Deviations from the reference for each DFM for the Fast-range motion profile using as input the data composition according to scenario 8.	68
Figure 30: Error Boxplot distribution for each DFM axes considering the Fast-range profile as IDS. A total of 7000 samples are represented in each axis of each DFM.	69
Figure 31: LSM and BNO gyroscopes signals (three first plots) and temperature plot (last graph) during the long-term experiment. The red line indicates the sunrise and the yellow zone the period when the RIMU's bottom side was exposed to direct sunlight.	71
Figure 32: Accelerometers original and uncalibrated data recorded from LSM and BNO confronted against the temperature variation for the long-term experiment.	72

Figure 33: DFM outputs presented after a 10-second moving average window for the long-term experiment. DFM parameters are those selected by the Slow-range experiment.....	72
Figure 34: Setup to test the system performance when it is exposed to ferromagnetic materials.....	74
Figure 35: LIS and BNO readings with their mean value removed. The blue zone indicates the time length when the transformer is close to the RIMU board.....	74
Figure 36: Data Fusion Methods performance while the magnetometers are approximated to a ferromagnetic object. The Slow-range (see Section 4.2.1) coefficients are used.....	75
Figure 37: Data Fusion Methods performance while the magnetometers are approximated to a ferromagnetic object. The Mid-range (see Section 0) coefficients are used.	75
Figure 38: Static perform evaluation experiment setup.	77
Figure 39: DFMs performance during the Static experiments.	77
Figure 40: DFMs yaw deviations for each consecutive RIMU orientation. Transition periods are omitted.	78
Figure 41: Illustration of the Full RIMU PCB. Top trails are represented in red color while bottom trails are in green. Blue lines represent top silkscreen while bottom silkscreen is in pink. Internal copper layers (second [3.3V] and third [GND]) are hidden.	82
Figure 42: Illustrative 3D model of Full RIMU.	82

LIST OF TABLES

Table 1: AHRS and MEMS characteristics. NA stands for “non-applicable”. While “—” stands for “no information is available” .	36
Table 2: Test Jig main characteristics.	43
Table 3: GA individual description and search limits	47
Table 4: Mean of angular speed (in degrees per second – dps) for each step of Figure 15.	56
Table 5: Optimum filter parameter according to the input data scenario for the Slow-range movement profile.	58
Table 6: KTE and RMSE values for each axis and each DFM for the Slow-range profile experiment. RMSE errors are presented in degrees.	61
Table 7: Optimum filter parameter according to the input data scenario for the Mid-range movement profile.	62
Table 8: KTE and RMSE values for each axis and each DFM for the Mid-range profile experiment. RMSE errors are presented in degrees.	66
Table 9: Optimum filter parameter according to the input data scenario for the Fast-range movement profile.	66
Table 10: Kalman Filter coefficients reached during the GA optimization for each experiment.	67
Table 11: KTE and RMSE values for each axis and each DFM for the Fast-range profile experiment, with their optimizable parameters already adjusted, using as IDS the configuration proposed by the scenario 8. RMSE errors are presented in degrees.	69
Table 12: Noise energy according to the DFM and the window size. Units in degrees ² .	73
Table 13: Mean orientation deviation due the temperature variation during the long-term experiment. Units in degrees.	73
Table 14: Peak deviation during the magnetometer disturbance experiments for two different DFMs parameters set. Values are presented in degrees.	76
Table 15: KTE and RMSE error for the Static experiment. σ stands for error standard deviation.	78

LIST OF ABBREVIATIONS AND ACRONYMS

μSD	MicroSD card, Micro Secure Digital card
ADC	Analogic to Digital Converter
AEKF	Additive EKF
AHRS	Attitude and Heading Reference System
BNO	Related to BNO055
bps	Bits per second
CAN	Controller Area Network
CAS	Cross Axis Sensitivity
CCW	Counterclockwise
CF	Complementary Filter
DCM	Direction Cosine Matrix
DFM	Data Fusion Method
DoF	Degrees of Freedom
dps	Degrees per second
DTG	Dynamically Tuned Gyroscopes
EKF	Extended Kalman Filter
FAA	Federal Aviation Administration
FOG	Fiber Optic Gyroscope
FPU	Float Point Unit
FS	Full Scale
FULL RIMU	Related to the second version of RIMU
GA	Genetic Algorithm
GMEKF	Generalized Multiplicative EKF
I ² C	Inter-Integrated Circuit
IC	Integrated circuits
IDS	Input Data Set
IFOG	Interferometric Fiber-Optic gyroscopes
IMU	Inertial Measurement Unit
KF	Kalman Filter
LIS	Related to LIS3MDL
LSM	Related to LSM6DS33
M.Sc.	Master of Science
MARG	Magnetic Angular Rate and Gravity
MEFK	Multiplicative Extended Kalman Filter
MEMS	Microelectromechanical systems

MIMU	Multi-IMU, Multi Inertial System Measurement Unit
OEM	Original equipment manufacturer
PCB	Printed Circuit Board
PCB	Printed Circuit Board
ppm	Partsparts per million
PWM	Pulse-Width Modulation
QUEST	Quaternion Estimation Algorithms
RIEKF	Right Invariant Extended Kalman Filter
RIMU	Redundant Inertial Measurement Unit
RLG	Ring Laser Gyroscope
RMSE	Root Mean Square Error
RS-485	Referred to the standard RS-485 communication protocol
SERCOM	Serial Communication Interface
SLERP	Spherical Linear Interpolation
SoC	System on Chip
SPI	Serial Peripheral Interface
SPS	Samples per second
TC	Timer Counter
TC	Timer Counter
TJ	Test Jig
TWI	Two Wire Interface
UART	Universal Asynchronous Receiver/Transmitter
USART	USART - Universal Synchronous/Asynchronous Receiver/Transmitter
USB	Universal Serial Bus
USD	American Dollar
VRU	Vertical Reference Unit

LIST OF SYMBOLS

θ_0, ω_0	Initial angular position and initial angular velocity
σ^2	Orientation error variance
α	Rotation angle around axis x, often called the roll or bank
β	Rotation angle around axis y, often called the pitch or attitude
γ	Rotation angle around axis z, often called the yaw or heading
θ	Angular position
φ	Mean absolute orientation estimation error
ω	Angular velocity
ϕ	Angle between two successive quaternions
α	Angular acceleration
q_i	i-th element of quaternion vector
\mathbf{q}	Imaginary part of a quaternion
\hat{q}	Actual best quaternion orientation estimation
q_{obs}	Estimation of sensor orientation only considering the accelerometer and magnetometer readings
q^k	Quaternion output at a single k iteration
δq	Quaternion orientation error
dq	Estimated orientation taking into consideration solely the gyroscope readings
Beta	Madgwick's Algorithm optimizable parameter
Kp	Mahony's Algorithm optimizable parameter
mod	Relative to the modulo operation

CONTENTS

1	INTRODUCTION	17
1.1	BACKGROUND AND MOTIVATION	17
1.2	OBJECTIVES.....	17
1.3	JUSTIFICATION	18
1.4	DISSERTATION STRUCTURE	18
2	THEORETICAL BACKGROUND	20
2.1	ROTATION REPRESENTATION IN THREE-DIMENSIONAL SPACE.....	20
2.1.1	Rotation Matrix or Direction Cosine Matrix (DCM)	20
2.1.2	Euler angles	21
2.1.3	Quaternions	22
2.1.3.1	Quaternion principles.....	22
2.1.3.2	Quaternion rotations.....	23
2.1.3.3	Quaternion interpolation	25
2.1.4	Assessment of the orientation representation methods	25
2.2	INERTIAL AND MAGNETIC SENSORS	26
2.3	DATA FUSION METHODS.....	29
2.3.1	Complementary Filter	30
2.3.2	Kalman Filter and its variants	31
2.3.3	Mahony's Algorithm	32
2.3.4	Madgwick's Algorithm	33
2.3.5	Other fusion methods	33
2.4	COMMERCIAL INERTIAL MODULES AND SYSTEMS	34
2.5	REDUNDANT INERTIAL SENSING	37
3	MATERIALS AND METHODS	39
3.1	HARDWARE RIMU v1.....	39
3.2	TWO DEGREES OF FREEDOM TEST JIG	42
3.3	DATA FUSION METHODS AND ERROR MEASUREMENTS METHODOLOGY	44
3.3.1	Cost Function and excitation data	44
3.3.2	Optimization methods	47

3.3.3	Test-Jig-RIMU alignment and synchronization	48
4	EXPERIMENTS AND PERFORMANCE EVALUATION.....	51
4.1	TEST JIG EVALUATION	51
4.1.1	Kinematic reconstruction and Jig speed control performance evaluation	51
4.1.2	Motor influence over Magnetometer readings	52
4.1.3	Jig vibration evaluation and gyroscope calibration.....	54
4.2	SENSOR PERFORMANCE AT THE TEST JIG	57
4.2.1	Slow-range profile experiment	57
4.2.2	Mid-range profile experiment	62
4.2.3	Fast-range profile experiment	66
4.3	RIMU LONG-TERM STABILITY – DATA FUSION METHODS PERFORMANCE OVER TEMPERATURE VARIATION	70
4.4	PERFORMANCE EVALUATION AT EXPOSURE OF FAST MAGNETIC DISTURBANCE	73
4.5	STATIC DFM PERFORMANCE EVALUATION	76
5	CONCLUSIONS AND FUTURE WORK	80
5.1	CONCLUSIONS	80
5.2	CONTRIBUTIONS.....	81
5.2.1	Hardware update: FULL RIMU	81
5.2.2	Applications	83
5.3	PUBLICATIONS	84
5.4	FUTURE WORK.....	84
	REFERENCES	85

1 INTRODUCTION

1.1 BACKGROUND AND MOTIVATION

Considering the constant technology improvements in the area related to Inertial Measurement Units (IMU) based on Microelectromechanical Systems (MEMS) [1]–[3] a large and ever-growing number of MEMS-IMU applications are now technically and costly viable; i.e. tactical navigation [4]–[6], human motion tracking [7]–[11], fall detection in elderly patients [2], automation of mobility tests [12], earthquake [13] and structural vibration monitoring [3], detection of heat period in milky cows [14].

Such a large range of applications is directly related to the most important MEMS-IMU characteristics: low cost, small dimensions, and low power consumption. Such features are constantly mentioned in the works found on the literature (such as the ones cited in the preceding paragraph), and not present in most of inertial and magnetic sensors based on other technologies [1], [15].

Even though MEMS-IMU systems are widely used, precision and accuracy issues are still limiting its application in many fields, for instance, MEMS sensors are not used as inertial guide reference in air planes [1] nor gait analysis' gold standard incorporates MEMS sensors [11]. Which are clear indicators that MEMS-IMU systems still have issues to overcome.

Additionally, most of MEMS commercial solutions are expensive, many present low sampling rates, and work as **black-box** [5], [14]–[19], where the user has none or little control over the orientation estimation process and its dynamics, what may heavily impact on the system performance. This dissertation will discuss the main issues regarding the use and development of MEMS IMU systems. Additionally, a MEMS IMU system is proposed and developed aiming to address the main problems of commercial systems.

1.2 OBJECTIVES

The main goal of this dissertation is to develop systems (including their hardware) able to compare and classify the performance of Data Fusion Methods (DFM) using as input real inertial and magnetic data coming from redundant microelectromechanical sensors. The final goal is to produce a device with accuracy similar to high-end commercial Attitude and Heading Reference Systems (AHRS), but, yet customizable.

More specifically the objectives of the dissertation are summarized as follows:

- To develop a microcontrolled printed circuit board (PCB) having reduced dimensions and capable of acquiring data from different sensors.
- To develop a reference system, named Test Jig (TJ), with at least two degrees of freedom (DoF).

- To reconstruct the kinematic of the TJ.
- To synchronize the data from the inertial sensors along with the kinetic data from TJ.
- To evaluate and adapt existing DFM to use data from the real inertial sensors.
- To develop methods to, fairly, compare the performance and robustness of the selected DFM methods.
- To evaluate the performance gain when redundant sensors are used.
- To provide an opensource database of inertial and magnetic data along with a reference orientation.

1.3 JUSTIFICATION

This dissertation aims to address four main issues that are usually found in commercial, and even in academic, systems; as it is described particularly throughout the Chapter 2. A common aspect among commercial systems is the limitation, or totally incapacity, of customizing filter and system parameters, creating what is known as a **black-box**. As it is evidenced in Section 2.4, high-end commercial IMUs have relatively **high-cost** hampering its broad adoption. Another feature that has been improved by manufacturers over the last years, but still a weakness in many systems is the **low sampling rates**, which is limited to 100Hz in some products.

Finally, the system **accuracy** is still an important topic for those whose sensors have MEMS as main technology. Sensor redundancy has been presented as a viable characteristic to amend this issue, however, there is not a commercial example that uses sensor redundancy with the objective of improving system performance. Moreover, experiments have demonstrated that the performance gain of sensor redundancy has not been fully exploited because of error correlation among sensors of the same vendor, as it is exposed in Section 2.5.

1.4 DISSERTATION STRUCTURE

This M.Sc. dissertation is divided into five chapters. Chapter 1 exposes a brief contextualization along with the research objectives and the outlier of the systems that are proposed. Chapter 2 presents a literature review related to the three most common mathematical tools to represent rotations, focusing on quaternions and its particularities.

Chapter 2 continues with the presentation of different Data Fusion Methods (DFM), followed by a comparison of commercial systems and sensors based on MEMS technology. It finishes addressing a review of some researches related to the use of redundant systems based on MEMS in which the goal of the redundancy is to improve the system performance rather than reliability.

Chapter 3 presents the materials and systems that were developed, besides the optimization methods that were implemented. Chapter 3 ends presenting the methodology used to compare the results of each DFM against the TJ reference.

Chapter 4 contains the results and discussion related to the experiments that were performed and, finally, Chapter 5 presents the conclusions and future work of this MSc Dissertation.

2 THEORETICAL BACKGROUND

2.1 ROTATION REPRESENTATION IN THREE-DIMENSIONAL SPACE

Rotation is a motion of a certain space that preserves at least one point [17]. In geometry, it is possible to express a rotation of a rigid body in a three-dimensional Euclidian space through different mathematical formalisms, in this Section, it is presented the three most common tools: Rotation Matrix, Euler Angles and Quaternions.

2.1.1 Rotation Matrix or Direction Cosine Matrix (DCM)

Diebel [18] defines a rotation matrix as a matrix that when pre-multiplied by a vector expressed in the *global reference coordinate* (also named *world coordinate system*) yields the same vector expressed in the *body-fixed coordinate*, which is a reference system rigidly attached to the object whose orientation we would like to describe.

Such matrix must also preserve the vector length, therefore, the matrix determinant must be equals to 1 or -1 and for this reason, $\mathbf{M}^{-1} = \mathbf{M}^T$. Moreover, the analysis of rotations of rigid-bodies is limited to matrices with determinant equals to 1.

The special orthogonal group of all 3×3 matrices that fit those restrictions is denoted by $SO(3)$. Often, Rotation Matrixes are also referred to as Direction Cosine Matrix (DCM) because its elements may be expressed only by cosines.

A coordinate rotation is a rotation about a single coordinate axis. Equations (2.1), (2.2) and (2.3) are examples of matrices that map coordinate rotations around the x, y and z axes, respectively. A rotation in any direction can be expressed as three successive coordinate rotations and the final rotation matrix is calculated multiplying the coordinate matrices. Equation (2.4) denotes the rotation matrix for the zyx rotation order, where c stands for cosine function and s stands for the sine function.

$$\mathbf{M}_x(\alpha) = \begin{bmatrix} 1 & 0 & 0 \\ 0 & \cos(\alpha) & -\sin(\alpha) \\ 0 & \sin(\alpha) & \cos(\alpha) \end{bmatrix} \quad (2.1)$$

$$\mathbf{M}_y(\beta) = \begin{bmatrix} \cos(\beta) & 0 & \sin(\beta) \\ 0 & 1 & 0 \\ -\sin(\beta) & 0 & \cos(\beta) \end{bmatrix} \quad (2.2)$$

$$\mathbf{M}_z(\gamma) = \begin{bmatrix} \cos(\gamma) & -\sin(\gamma) & 0 \\ \sin(\gamma) & \cos(\gamma) & 0 \\ 0 & 0 & 1 \end{bmatrix} \quad (2.3)$$

$$\mathbf{M} = \mathbf{M}_z \mathbf{M}_y \mathbf{M}_x(\alpha, \beta, \gamma) = \begin{bmatrix} c_\alpha c_\beta & s_\alpha c_\gamma + c_\alpha s_\beta s_\gamma & s_\alpha s_\gamma - c_\alpha s_\beta c_\gamma \\ -s_\alpha c_\beta & c_\alpha c_\gamma - s_\alpha s_\beta s_\gamma & c_\alpha s_\gamma - s_\alpha s_\beta c_\gamma \\ s_\beta & -s_\gamma c_\beta & c_\gamma c_\beta \end{bmatrix} \quad (2.4)$$

2.1.2 Euler angles

Euler angles are probably the most intuitive form to mathematically represent three-dimensional space rotations. Euler stated that “any two independent orthonormal coordinate frames can be related by a sequence of rotations (not more than three) about coordinate axes, where no two successive rotations may be about the same axis” [19]. Therefore, the angles of those three rotations are known as Euler angles.

Euler angles as applied to the Maritime and Aerospace industries are often called the roll or bank angle (α), about the x -axis, the pitch or attitude angle (β), about the y -axis, and the yaw or heading angle (γ), about the z -axis [20]. This work will adopt the roll, pitch and yaw nomenclature.

For a right-handed coordinate system with all three angles defined as positive rotations, there are twelve possible sequences of rotations that do not contravene the Euler statement [21], as it is exhibited in Equation (2.5). These sequences are divided into two sets: the ones with the non-repeated axes (the first two rows of (2.5)) and the ones with the repeated rotation axes (the last two rows of (2.5)).

$$\left(\begin{array}{ccc} xyz & yzx & zxy \\ xzy & yxz & zyx \\ xyx & yzy & zxz \\ xzx & yxy & zyz \end{array} \right) \quad (2.5)$$

From all twelve possible sequences, emphasis must be given to the zyx which is known as the *aerospace sequence* (for the Russian aerospace industry the default in 1966 was yzx [21]), and for the zxx that is known as *orbit sequence* [22].

For any set of Euler angles, where the second rotation aligns the axes of the first and third rotations, there is a singularity, as can be didactically visualized in [23]. For a rotation sequence with repeated rotation axis, singularities occur for second rotation angles at zero and π ; for non-repeated axis sequences, singularities occur at $\pm \pi/2$ [20], [24]. Such singularities can be mathematically exemplified by (2.6), where the operations to extract the Euler angles with zyx rotation order from the DCM matrix (2.4) are exhibited. Equation (2.6) has singularity points for $\beta' = \pm \pi/2$.

$$\begin{aligned}
\beta' &= -\beta \\
\gamma' &= \operatorname{asin} \left(\frac{-\sin(\gamma) \cos(\beta)}{\cos(\beta')} \right) \\
\alpha' &= \operatorname{acos} \left(\frac{\cos(\alpha) \cos(\beta)}{\cos(\beta')} \right)
\end{aligned} \tag{2.6}$$

The singularity here mentioned is also known as gimbal lock. The term gimbal lock originally describes the mechanical phenomenon of the loss of one degree of freedom of a mechanical gimbal, which happens when two spinning rings align at the same plane [24, Sec. 2.3].

It is important to emphasize that gimbal lock is also a phenomenon that is intrinsically present in the representation of rotations by Euler angles [18], [24]. Therefore, even though the orientation of a rigid body is calculated using a mathematical representation that is gimbal-lock-immune (i.e. quaternions or DCM), the conversion to Euler angles may cause gimbal lock issues, as can be visualized in Equation (2.6) when $\cos(\beta')$ tends to zero.

2.1.3 Quaternions

2.1.3.1 Quaternion principles

The interests about an “alternative” mathematical tool, named as quaternions, firstly specified by William Rowan Hamilton in 1843, arose in the middle of the 1950’s decade when the desire of developing an anti-Inter Continental Ballistic Missile faced gimbal-lock issues [22].

Quaternion is defined by Hanson [24] as a four position vector defined as $q = (q_0, q_1, q_2, q_3) = (q_0, \mathbf{q})$, where q_0 and $\mathbf{q} = (q_1, q_2, q_3)$ are named, respectively, the scalar and the vector part of a quaternion [22]. Non-commutative multiplication rule (\star), named as Hamiltonian product, is assigned to quaternions, such rule is presented in Equation (2.7), where p and q are quaternions.

$$\begin{aligned}
p \star q &= (p_0, p_1, p_2, p_3) \star (q_0, q_1, q_2, q_3) \\
&= \begin{bmatrix} p_0 q_0 - p_1 q_1 - p_2 q_2 - p_3 q_3 \\ p_1 q_0 + p_0 q_1 + p_2 q_3 - p_3 q_2 \\ p_2 q_0 + p_0 q_2 + p_3 q_1 - p_1 q_3 \\ p_3 q_0 + p_0 q_3 + p_1 q_2 - p_2 q_1 \end{bmatrix}
\end{aligned} \tag{2.7}$$

This may also be written as Equation (2.8), being (\cdot) the dot product while (\times) represents the cross product:

$$p \star q = (p_0 q_0 - \mathbf{p} \cdot \mathbf{q}, p_0 \mathbf{q} + q_0 \mathbf{p} + \mathbf{p} \times \mathbf{q}) \tag{2.8}$$

There are also other two basic quaternion operations: the inner product (2.9) and the conjugation rule (2.10).

$$p \cdot q = p_0q_0 + p_1q_1 + p_2q_2 + p_3q_3 = p_0q_0 + \mathbf{p} \cdot \mathbf{q} \quad (2.9)$$

$$\bar{q} = (q_0, -q_1, -q_2, -q_3) \quad (2.10)$$

The quaternion conjugate can also be denoted by q^* , q^t or \tilde{q} . It is also common in the literature to represent the complex part of a quaternion using the letters i , j , and k such as presented in [22], [25]. However this work will follow the notation adopted by [24], such notation is also present in [18], [26]–[28].

The analysis of rotations about the origin of three-dimensional Euclidian space are restricted to unit length quaternions, henceforth named only as quaternions, in accordance with (2.11). Equation (2.11) imposes the loss of one degree of freedom to the quaternion representation, limiting the 4D Euclidian Space to a *hypersphere*, formally written as S^3 [24].

$$q \cdot q = (q_0)^2 + (q_1)^2 + (q_2)^2 + (q_3)^2 = 1 \quad (2.11)$$

The inverse of a quaternion is given by Equation (2.12), for the special case of unit length quaternions, the inverse is equal to its conjugate.

$$q^{-1} = \frac{\bar{q}}{\|q\|^2} \quad (2.12)$$

The “classical” (vectorial) addition and subtraction do not have a practical meaning in quaternion, and they are replaced, respectively, by the quaternion multiplication (2.13) and by the multiplication of the inverse (2.14), emphasizing that both operations are order dependent.

$$(x_1 + x_0) \rightarrow q_0 \star q_1 \quad (2.13)$$

$$(x_1 - x_0) \rightarrow (q_0)^{-1} \star q_1 \quad (2.14)$$

2.1.3.2 Quaternion rotations

As the Euler’s theorem states, all 3D rotations (\mathbf{R}_3) have a single real eigenvector and can be written in terms of a single final rotation matrix. Particularly, a rotation can be expressed by a unit length vector $\hat{\mathbf{n}}$, which is parallel to the rotation axis, and a rotation angle θ [24, Sec. 6.2], as it is shown in Equation (3.13).

$$\mathbf{R}_3(\theta, \hat{\mathbf{n}}) \cdot \hat{\mathbf{n}} = \hat{\mathbf{n}} \quad (2.15)$$

Hanson [24] proves that a rotation can be written in a quaternion form (2.16), and the final rotation matrix is, therefore, written as (2.17).

$$\begin{aligned}
q_0 &= \cos(\theta/2) \\
q_1 &= n_1 \sin(\theta/2) \\
q_2 &= n_2 \sin(\theta/2) \\
q_3 &= n_3 \sin(\theta/2)
\end{aligned} \tag{2.16}$$

$$\mathbf{R}(q) = \begin{bmatrix} q_0^2 + q_1^2 - q_2^2 - q_3^2 & 2q_1q_2 - 2q_0q_3 & 2q_1q_3 + 2q_0q_2 \\ 2q_1q_2 + 2q_0q_3 & q_0^2 - q_1^2 + q_2^2 - q_3^2 & 2q_2q_3 - 2q_0q_1 \\ 2q_1q_3 - 2q_0q_2 & 2q_2q_3 + 2q_0q_1 & q_0^2 - q_1^2 - q_2^2 + q_3^2 \end{bmatrix} \tag{2.17}$$

The quaternion rotation operator that takes $v \rightarrow w$ is:

$$w = qvq^* \tag{2.18}$$

It is important to notice that since all terms in Equation (2.17) are second-order terms, it is simple to visualize that the equation (2.19) holds for any rotation represented by quaternions.

$$\mathbf{R}(q) = \mathbf{R}(-q). \tag{2.19}$$

The equality (2.19) is one example of a hampering factor for orientation comparison using quaternions. In order to provide a comprehensive orientation comparison in terms of angular error, a quaternion subtraction should be performed. The resulting quaternion can be then converted to Euler angles, the aforementioned process is described by Bergamini et al. [9] and in this particular Dissertation the native MATLAB `quat2angle` function was used to convert quaternions to Euler angles.

However, such procedure does not result in a fair and intuitive comparison between two orientations. This is because the angle difference calculated in the second rotation may not be equal to the real (intuitive) angle difference, as it was found in practical tests. To better exemplify, consider two orientations with the following orientations:

$$\begin{aligned}
\alpha_1 &= 30^\circ & \alpha_2 &= 35^\circ \\
\beta_1 &= 10^\circ & \beta_2 &= 15^\circ \\
\gamma_1 &= 20^\circ & \gamma_2 &= 25^\circ
\end{aligned} \tag{2.20}$$

Calculating the orientation difference according to the procedure proposed by [9] would result in a difference of 2.37, 4.05 and 6.41 for Yaw, Roll and Pitch orientations. To amend this problem, the orientation difference, in this dissertation, was always calculated in terms of Euler angles, avoiding sequences where gimbal lock would occur and compensating Euler discontinuities through the equation exhibited by (2.21), firstly proposed by Corke [29], where θ_1 and θ_2 are the angles of interest expressed in radians and mod stands for the modulo operation.

$$d = \{[(\theta_1 - \theta_2) + \pi] \bmod 2\pi\} - \pi \tag{2.21}$$

2.1.3.3 Quaternion interpolation

As it is stated by Hanson [24], quaternions domain lies on a hypersphere, hence a linear interpolation of two quaternions might not represent the real distance between them nor produce a normalized quaternion, even though the resulting quaternion could be renormalized. A simple example is the linear interpolation of q and $-q$, the result of a linear interpolation is a zero vector, whereas the correct result is q or $-q$.

The correct method to interpolate two quaternions, q_a and q_b , is named by Hanson [24, Ch. 10] as Spherical Linear Interpolation (SLERP) and it is calculated using Equation (2.22).

$$q(t) = q_a \frac{\sin(1-t)\phi}{\sin(\phi)} + q_b \frac{\sin(t\phi)}{\sin(\phi)} \quad (2.22)$$

$$\phi = \arccos(q_a \cdot q_b)$$

Equation (2.22) is computationally expensive and many fusion algorithms do not implement it. Alternatively, they calculate a quaternion that is an estimative of the rate of change, which should have only a small deviation and perform the vector sum. Some examples are [30]–[32].

Quaternion averaging is an important process, especially to extract the initial orientation of an object; it should also be accomplish using the Spherical Linear Interpolation (SLERP) Equation (2.22). However, Markley et al. [33] proposed a computationally cheaper algorithm based on the extraction of the largest eigenvector of the matrix composed by all quaternions that should be averaged. Such method was implemented by Birdal [34] and will be the method used to obtain average quaternions in this work.

2.1.4 Assessment of the orientation representation methods

Compared to DCM, the representation of rotations through quaternions has the advantages of not being rotation-dependent, moreover, quaternions representation is more compressed than DCM representation – DCM requires 125% more space to be stored and transmitted. The computational burden created by DCM and quaternions rotation are application-dependent and the choice of the optimal representation is not trivial [24, Ch. 16].

Compared to Euler angles, the quaternion representation has the clear drawback of not having a clear physical meaning; therefore, compare the module of the orientation deviation in quaternion is not a trivial task. However, quaternion representation does not have singularities and is not rotation-dependent.

This work has as the main goal the development of inertial fusion system that is oriented to run embedded. The object orientation will be transmitted to a server through a channel that has a low throughput range (i.e. Bluetooth 2.1 or Zigbee). Therefore, the storage size is not directly a

concern, but the amount of data that must be transmitted is; limiting the employment of algorithms with DCM orientation. Another main characteristic of the fusion system is that it will be applied in a generic environment, thus it cannot have a preferred orientation or singularity points, limiting the use of Euler angles.

The superiority of quaternions parameterization with respect to the rotation matrices or the Euler angles representations is broadly documented, both in terms of lower computational burden [35] and of reduction of errors associated with the numerical integration [36]. For all reasons previously presented, quaternion representation is the standard rotation adopted in this work.

2.2 INERTIAL ANG MAGNETIC SENSORS

An inertial system consists of devices that are able to measure angular speed, properly named gyroscopes, and devices that are sensitive to linear accelerations, denominated accelerometers. The inertial system was first applied to the Naval Antiaircraft Fire Control during the World War II [37]. Later, a remarkable application was the Attitude Heading Reference System (AHRS) on the Apollo program. Those systems consisted of spinning wheels and mass-spring systems; Figure 1 shows an example of such system in the late 1950s.

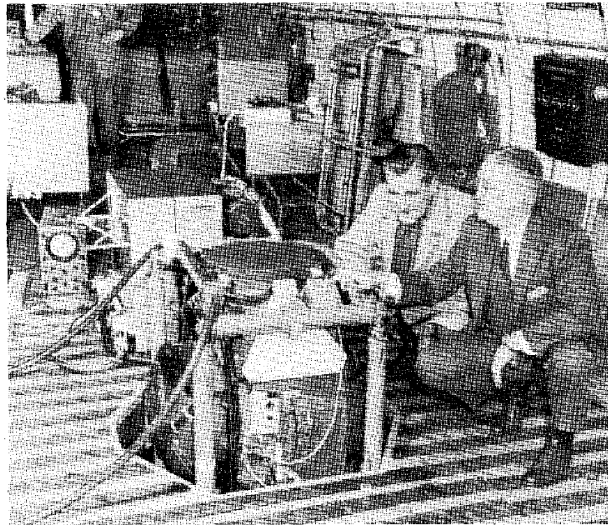


Figure 1: Eric Severaid and Stark Draper observe Spire Jr. gimbals on flight from Massachusetts to California, March 7, 1958. (Source: C. S. Draper, 1981 [37]).

Moderns gyroscopes have its performance directly linked to its principle of operation [1]. For example, the gyroscope bias stability (the amount of deviation from the zero angular velocity along the time) can range over more than six orders of magnitude [15]. Passaro et al. [1], in a review, cite four sets of commercial gyroscopes, classifying them according to the sensing principle which is: mechanical gyroscopes, Fiber Optic Gyroscopes (FOGs), Ring Laser Gyroscopes (RLG), Micro-electromechanical system (MEMS) gyroscopes.

Passaro et al. [1] continue classifying and grouping the gyroscopes according to the scale factory stability, the bias stability and application. Scale factory stability represents the sensitivity of the gyroscope, smaller values indicate a better instrumentation and higher costs. The result is indicated in Figure 2.

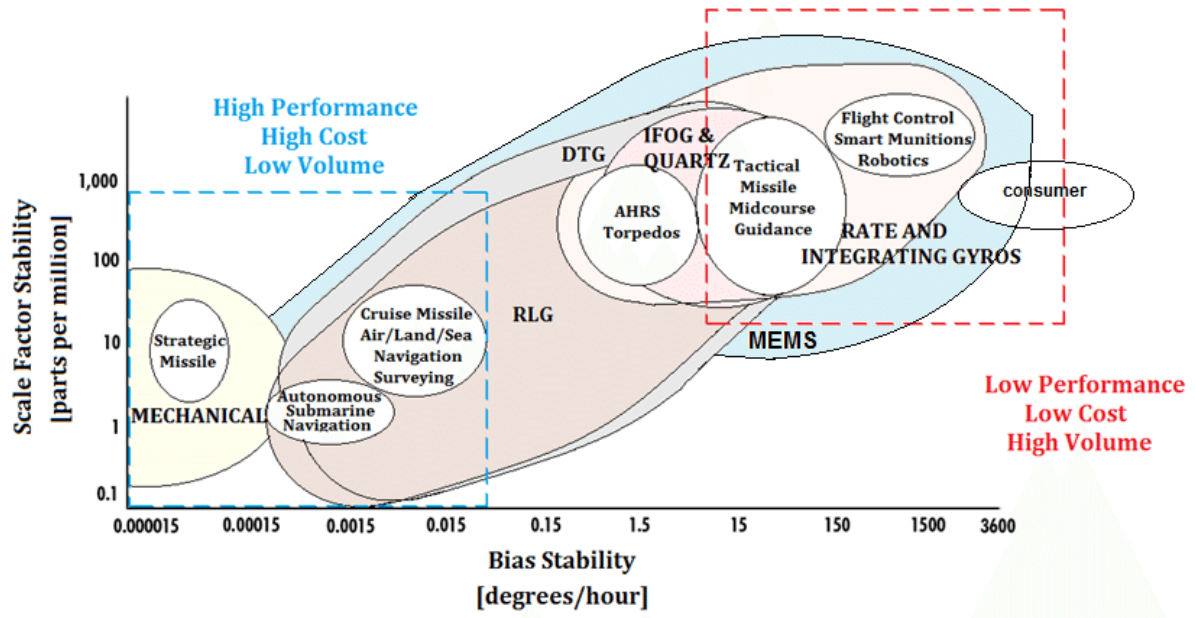


Figure 2: Scale factor stability (i.e., the accuracy of the gyroscope in monitoring the sensed angular velocity), expressed in parts per million (ppm), as a function of the bias stability (intrinsically dependent on the gyroscope technology) for Mechanical Gyroscopes, Ring Laser Gyroscopes (RLG), Interferometric Fiber-Optic gyroscopes (IFOG), Quartz, Dynamically Tuned Gyroscopes (DTG), Rate and Integrating Gyroscopes and MEMS. (Source: Passaro et al., 2017 [1]).

Currently, MEMS sensors are the smallest, lightest and cheapest sensors available; MEMS gyroscopes generally use a vibrating mechanical element for detecting the angular velocity, according to the Coriolis Effect [1]. MEMS technology is the only one that is able to produce commercial wearable gyroscopes and accelerometers; hence, special attention will be given to MEMS sensors.

Xsens [38], a company that develops and manufacture MEMS-AHRS, points out four aspects that must be analyzed during the characterization of a gyroscope, besides Passaro et al [1] indicate another two parameters that should also be taken into consideration when the device is a MEMS gyroscope. Such aspects and parameters are presented in the following paragraphs.

The deviation of a linear best fit curve of the measured data is named **non-linearity**, it is usually expressed in terms of sensor full scale (FS), e.g. 0.1 % FS, the error after a 360° turn can be 0.36° from non-linearity alone.

Bias stability, measured in °/h, also called turn-on to turn-on or bias repeatability is generally caused by relaxation, temperature and start-up effects. Gyroscope bias is characterized by the

offset measured when the sensor is not moving usually given as degrees per second (dps) or radians per second.

The relation between bandwidth and noise is termed **noise density** or rate noise density. Such relation is usually expressed in dps/\sqrt{Hz} . Active elements of the gyroscope are the major contributors to random noise. It is important to notice that increasing the sensor bandwidth increases the noise observed in the sensor outputs.

Full range, also termed measurement range or full scale, is the maximum angular velocity that can be measured by the sensor without saturation.

MEMS gyroscopes are especially **sensitive to temperature variations** resulting in increase of random noise and change of bias offset. Currently, most of them have an internal temperature sensor to compensate drifts.

Finally, it is known that noise and bias offset of gyroscopes also degrade under vibration and shock input, therefore, **shock and vibration sensitivity** constitute the last listed relevant parameter of a gyroscope specification.

Another critical component of an inertial system is the accelerometer. In general, accelerometers are force sensors measuring a specific force due to acceleration and/or gravity applied to a string by a proof mass [2]. Similarly to the gyroscope, accelerometer performance and cost are intrinsically dependent to the principle of operation [39]. Different methods that fit in the definition of a MEMS device have been developed such as piezoresistive, piezoelectric, differential capacitive and surface capacitive accelerometers [2], [39].

Xsens [40] along with Sabato et al. [3] indicate six parameters that should be analyzed before select an accelerometer four of them are similar to the ones pointed out to gyroscopes: non-linearity (%FS), noise-density ($m\cdot s^{-2}\cdot Hz^{-0.5}$), bias stability ($m\cdot s^{-2}$) and measurement range ($m\cdot s^{-2}$), the others two factors are explained in the following paragraph.

Bandwidth, usually measured in Hertz (Hz), is the difference between the upper and lower (for accelerometers it is usually zero Hertz) frequencies in which the device has a response attenuate by less than 3 dB. While **resolution**, usually measured in m/s^2 , is defined as the smallest detectable acceleration.

Modern systems, aside from gyroscopes and accelerometers, contain sensors, named magnetometers, capable of measuring magnetic fields. The addition of a magnetometer is necessary because of the inability of low-end MEMS systems composed of only accelerometer and gyroscope to estimate and maintain the correct yaw direction (along the plane perpendicular to the gravity) [9].

The aforesaid inability is based on the fact that there is no gravitational component to correct the integration errors of angular speed measured by a noisy MEMS gyroscope [30], [32]. The readings

of magnetometers, which ideally are composed only of Earth Magnetic Field, are then used as reference correcting the integration of gyroscopes in the yaw direction.

The integration of these three different sensors are commonly named MARG (Magnetic Angular Rate and Gravity) by some authors [31], [32], [41]. However, the denomination IMU (Inertial Measurement Unit), which was previously given to units that had only gyroscope and accelerometer, has also been attributed to those systems with magnetometer in replacing or as synonym of MARG [10], [16], [26], [27], [30], [42], [43]. Such fact is due to the presence of magnetometers in a vast number of commercial Original Equipment Manufacturer solutions (OEM) [44], final products [45] or even integrated circuits (IC) such as MPU9250, LSM9DS1 and BNO055 [46]–[48]. Therefore, this work also refers to a system containing tridimensional accelerometers, gyroscopes and magnetometers as IMU.

IMUs based on MEMS are projected positioning orthogonally 1D gyroscopes, accelerometers and magnetometers, thus MEMS IMUs do not face physical gimbal lock because there are not mechanical spinning rings. Although, if an inappropriate rotation representation is used, gimbal lock (the mathematical, not the physical one) may occur.

2.3 DATA FUSION METHODS

According to multiple literature reviews [1]–[3] and MEMS manufacturing portfolios [49]–[54], MEMS technology has been evolving in terms of noise and bias variation reduction, robustness, sensing range, power consumption, and other important parameters. Such advances make possible for MEMS sensors to be the core of a new generation of portable and accurate sensors.

However, the increase in precision of MEMS sensors must be followed by an improvement in performance of data processing and orientation extraction algorithms, also named Fusion Algorithms or Data Fusion Methods (DFM). Many of these algorithms along with multiple mathematical complex tasks must be able to run in real time. This section presents a brief review of DFM.

Zamani et al. [55] state that the comparison of DFM is difficult due to the natural process of developing algorithms, different notations, and rotation representations. Moreover, many of the advanced in DFM are still being advertised, demonstrating performance gain versus a not correctly tuned, naive or outdated implementations of Kalman Filters (KF) [55], [56]. Another critical factor is that most modern filters do not have open code access, what can lead to a poor mathematical interpretation of a proposed method or even code mistakes.

Reference systems and jigs for inertial systems are expensive [11], [57], furthermore, no database that would provide uniform data set from which developers could test their fusion algorithms (this is a default procedure in the Computer Science area) was found by the Author of this M.Sc.

Dissertation during his literature review. Instead, authors use as reference what they have in hands, i.e.:

- Alam et al. [58] have compared algorithms manually positioning the IMUs.
- Mahony et al. [30] proposed a novel algorithm using as reference a robotic manipulator combined with a set of synthetic magnetic data.
- Also using a robotic manipulator, Cavallo et al. [59] compared the performance of three DFM.
- Madgwick et al. [32] and Bergamini et al. [9] compared their novel DFM against orientation calculated by an optical reference platform.
- Bancroft and Lachapelle [8] had as reference a tactical IMU and GPS system.

This section aims to present a grounding review of a selected group of DFM that have demonstrated its applicability and performance. Three reviews about DFM are presented in [55], [60], [61].

2.3.1 Complementary Filter

Complementary filters (CF) provide a way to fuse multiple noisy measurements of the same signal that have complementary spectral characteristics. As an example, two measurements of the same signal x represented by $y_1 = x + \mu_1$ and $y_2 = x + \mu_2$, given that μ_1 is a high-frequency noise and μ_2 is predominantly low-frequency disturbance and their spectra do not overlap. Ideally, it would be possible then to filter μ_1 and μ_2 with a low and high-pass filter, respectively, completely reconstructing the x signal [30].

Considering the set of AHRS based on MEMS sensors, angular velocities measured by gyroscopes are composed by high-frequency signals and an additive low-frequency disturbance such as bias and temperature drift, whereas measurements made by accelerometers and magnetometers are composed typically by low-frequency signals and high-frequency noise.

The implementation of a complementary filter in quaternions is described by Alam et al. [58] in a reduced number of equations. Usually, complementary filters have the low-pass filter cutoff frequency (also known as crossover frequency) as the single tuning parameter. Ideally, this frequency matches the accelerometer and magnetometer bandwidth [62]. If one considers that such parameter does not change over time, it is possible to state that the CF faces the fusion problem in a deterministic manner.

A coded version of CF made available by Comotti [63] at her GitHub page. This CF version was developed in collaboration with STMicroelectronics and the Microelectronics Lab of the University of Bergamo.

This implementation has as the equations (2.23) and (2.24) where dq is the estimated sensor (IMU) orientation represented in quaternions taking in consideration, solely, the gyroscope readings $q_{gyro} = [0 \ \omega_\alpha \ \omega_\beta \ \omega_\gamma]$; q_{obs} is an estimation of sensor orientation only considering the accelerometer and magnetometer readings and q is the final estimated orientation.

$$dq = norm\left(0.5 * (q * q_{gyro})\right) \quad (2.23)$$

$$q = norm(dq \cdot crossover + q_{obs} \cdot (1 - crossover)) \quad (2.24)$$

As can be observed in equations (2.23) and (2.24), the version of CF proposed by Comotti [63] implements mathematical operations which are not well defined for quaternions such as the linear weighted average in equation (2.24) and the multiplication by 0.5 presented in equation (2.23). Those are amended solutions to reduce the computational burden of proper quaternion operations. Similar amendments are also present in other DFMs such as the one presented by Mahony et al. [64] and Madgwick et al. [32].

2.3.2 Kalman Filter and its variants

Kalman Filter (KF) dates back to 1960 [65]. It and its variants became the basis for the majority of orientation algorithms and commercial inertial orientation sensors, with applications that vary from human gait analysis to aircraft and satellite orientation [32], [55]. For a didactic review of Kalman Filter and its implementations, one can refer to [66], [67].

KF address the fusion problem in a stochastic manner. To estimate correctly the internal states, KF needs information about the process, such as its dynamic, the expected process noise covariance and the measurement noise covariance. To choose appropriate initial values to these parameters is decisive to the filter performance, while choosing inappropriate values may lead to converging issues as it is stated by Schneider and Georgakis [56].

As it is well known, KF only addresses linear problems. However, the fusion of inertial and magnetic data aiming to estimate the global orientation is a non-linear problem. The most straightforward manner to face a non-linear problem is linearize around the current best estimation, what leads to the extended version of Kalman Filter (EKF) [60].

According to Section 2.1, there are different manners to represent rotation what lead to different implementations of EKF. Even limiting the rotation representation to quaternions, there are many different EKF implementations. The next paragraphs briefly describe the implementations that were highlighted as the most promissory according to [55], [60], [61]. Note that the classic (pure) implementation of EKF is not one of them, because the use of quaternion as the rotation representation demands a set of techniques to deal with quaternions' algebra, otherwise the filter performance is compromised [55].

The Multiplicative Extended Kalman Filter (MEKF) has been used extensively in several NASA spacecraft [60]. Basically, it computes an unconstrained and non-singular three-parameter orientation error $\delta q(\phi)$ using as reference the actual best orientation estimation \hat{q} . The new orientation q is then calculated by (2.25). For more details refer to [68].

$$q = \delta q(\phi) \star \hat{q} \quad (2.25)$$

The Right-Invariant EKF (RIEKF), also named Generalized Multiplicative EKF (GMEKF), is based on the supposition that the state and the output errors are referred to the inertial frame (global reference) rather than the body-fixed frame. Such change in the error reference frame leads to a better stability and conditioning of the EKF equations comparing to those of MEKF. For more details refer to [69].

Similar to the MEKF, the Additive EKF (AEKF) treats a new orientation estimation as a $\delta q(\phi)$, however, the AEKF relaxes the quaternion normalization condition and treats the four components of the quaternion as independent parameters, adding uncertainties to the quaternion norm. The AEKF has proven to have a worse performance when compared to MEKF. For more details refer to [70].

The discussion about fusion methods that apply as a basis the Kalman Filter or its extended version seems somewhat poorly made by papers published in non-specialized journals. Take as an example the novel algorithms proposed in [25], [28]; their results do not compare the performance of the new methods against a standard Kalman Filter method (i.e. MEKF).

Instead, the performance of the new algorithm is validated only against a reference, which is also not a standard reference. Even though a standard reference had been used, qualify the fusion algorithm by its performance alone would not be possible because the final fusion error depends on the correctness of the raw data, which depends on the sensor characteristics. Despite the problems, the algorithms proposed in [25], [28] are used as references by many authors [71], [72] to validate new algorithms.

Another critical factor is the lack of source codes. The examples of Marins et al. [25] and Sabatini et al. [28], who have not made available their source codes, are followed by others authors [71], [72], hampering even further the comparison capability.

2.3.3 Mahony's Algorithm

Mahony et al. [30] propose the orientation estimation problem as a deterministic observation problem likewise to the complementary filter approach, inclusively it has one single tunable parameter named K_p . However, the DFM proposed by Mahony et al., named Explicit Complementary Filter, is non-linear and does not have a frequency domain interpretation.

This observer does not require online algebraic reconstruction of attitude and, as the authors state, is ideally suited for implementation on embedded hardware platforms owing to its low computational complexity.

However, the algorithm proposed by Mahony et al. suffers from possible discontinuities in the bias correction signal when the equivalent rotation angle of the estimated quaternion approaches $\pm\pi$ rad, that could result in systematic errors in the reconstructed attitude [59]. For more details about Mahony's Algorithm, one can refer to [30].

2.3.4 Madgwick's Algorithm

Madgwick et al. [32] presented a DFM with a single tunable parameter designed to be computationally efficient, executing only 109 and 248 scalar arithmetic operations each update for the versions without and with magnetic data, respectively. Madgwick's implementation is based on gradient descent algorithm which has as the optimizable parameter a coefficient similar to the gradient step size. Madgwick's Algorithm also considers that the magnetometer and accelerometer measure only earth magnetic field and gravity, respectively, the data provided by those sensors are used to correct the gyroscope integration. It uses quaternions as rotation representation and was originally designed to track human motion.

Even though it incorporates magnetic distortion compensation as the authors stated [32], a benchmark carried by Feng et al. [73] demonstrated that the gradient descent algorithm suffers from magnetic distortions producing errors not only in the yaw but also in the pitch and roll direction.

Madgwick provides his algorithm source code along with a Mahony's algorithm implementation, and both are available in [74].

2.3.5 Other fusion methods

Poor performance and/or even divergence arising from the linearization implicit in the EKF had led to the development of other filters [60], leading to higher order models or even completely different approaches such as Particle Filters, Fuzzy Logic algorithms, Bootstrap Attitude Filters, Quaternion Estimation Algorithms (QUEST) and Second-Order Optimal Minimum-Energy Filters [55], [60], [61].

Some of these nonlinear approaches have demonstrated performance gain over the standard version of MEKF, therefore reducing the asymptotic root mean square error (RMSE) of the angle estimation in the order of 1 degree for a scenario where low-cost MEMS IMUs are used as sensors [60]. However, their computational burden creates an obstacle for wearable embedded solutions, additionally, throughout the literature review, no implemented version of the aforementioned

filters was found that would be able to handle and fuse angular speed, linear acceleration and magnetic data simultaneously.

As an example, Zamani et al.[55] made available the source code of different DFMs, with different structures. However, they are implemented to fuse and filter angular speed only, therefore, their implementation disregards magnetic and linear acceleration data.

2.4 COMMERCIAL INERTIAL MODULES AND SYSTEMS

Systems that provide information about their pitch and roll angles are usually named Vertical Reference Units (VRU) whereas a system that besides pitch and roll provides information about the yaw angle is named Attitude and Heading Reference System (AHRS).

There is a reasonable amount of commercial AHRS, however, there is a reduced set of those commercial devices based on MEMS and an even smaller ensemble with reduced dimensions. This section provides a comparison of commercial AHRS with reduced size. Additionally, some MEMS sensors have their characteristics listed on Table 1, those will be later used in the project of an AHRS proprietary system.

Technaid (Spain) produces the TechIMU v4 which has its focus at the human movement. With the aid of a HUB, a Controller Area Network (CAN) with 16 sensors can be formed. Technaid states that its sensors implement EKF at sampling rates up to 500Hz with very low orientation error (see Table 1). Although Technaid does not provide further information about the noise characteristics of its sensors, previous works [26], [27] have pointed out larger errors and discrepancies between previous versions (v3) of its sensors.

Xsens (The Netherlands) produces MTi series, including the MTi-3 (Figure 3-b), MTi-30 and MTi-300 (Figure 3-c). Those sensors have wide range of application varying from human track to structure monitoring as it is stated by Xsens [4]. Its sensors are also used as source of raw data (without preprocessing) in some academic papers, such as the presented ones by Madgwick et al. [32]. As well as Technaid, Xsens uses EKF to fusion data, however Xsens provides more information about the noise and bias characteristics of its sensors.

Redshift Labs (Australia) produces the UM7-LT (Figure 3-d) which is a cheap and low precision AHRS previous produced by Pololu (US).

Aceinna (US) is a spinoff of MEMSIC (US). Aceinna is a company specialized in produce high-end MEMS sensors, as it is stated in Aceinna website. It was the first company that earned a certification for a MEMS AHRS from Federal Aviation Administration (FAA). Aceinna produces AHRS380ZA (Figure 3-e), which has a relative low cost and small size (comparing with other Aceinna products).

STT (Spain) produces the STT-IWS (Figure 3-f). Similar to TechIMU, it is an AHRS solution specialized in human motion, sharing inclusive the black-box aspect of TechIMU with no or few information about its sensors. Another similar black-box system is the one provided by Intersense (US), named InertiaCube4.

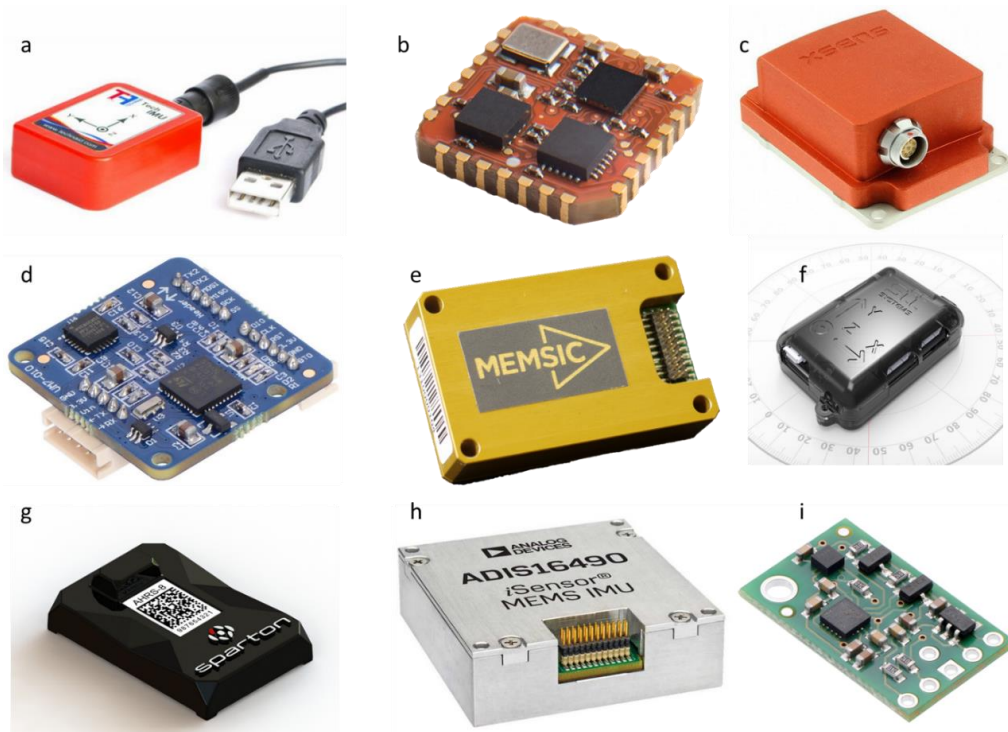


Figure 3: Illustration of commercial AHRS and MEMS sensors. **a)** TechIMU V4, **b)** MTi-3, **c)** MTi-30 or MTi-300, **d)** UM7-LT, **e)** AHRS380ZA, **f)** STT-IWS, **g)** AHRS-8, **h)** ADIS16490 and **i)** Minimu v5.

AHRS-8 (Figure 3-g) is produced by Sparton (US), which is a company that provides tactical solutions. Sparton states that AHRS-8 has a high tolerance to magnetic distortion and embedded 3D adaptive calibration.

Table 1 summarizes the AHRS comparison presenting key parameters of AHRS performance. It is pertinent to observe how the accuracy improvement directly reflects the sensor cost as it is demonstrated by the MTi-3 and MTi-30, both manufactured by Xsens. Such price discrepancy is also observed when gyroscopes and accelerometers with different performances are compared, as it is the case of the ADIS16490, ADIS16465-3 and LSM9DS1.

Additional relevant aspect is the absence of important information, regarding gyroscopes and accelerometers performance, in commercial solutions such as the ones offered by Technaid, Intersense and STT-IWS. None of manufactures explicitly present how the AHRS orientation performance evaluation is conducted nor cite a standard.

It is not feasible to resume all aspects that influence on AHRS performance on a single table; therefore, it is left out of this comparison important parameters such as nonlinearities, sensor misalignment, temperature coefficient, resolution, among others.

Table 1: AHRS and MEMS characteristics. NA stands for “non-applicable”. While “—” stands for “no information is available”.

System	Manuf.	Orientation Perform. Static Dynamic (± deg RMS)		Gyro bias stability (°/h)	Gyro noise density (°/s/√Hz)	Gyro full scale (± °/s)	Acc. Bias stability (mg)	Acc. noise density (μg/√Hz)	Power cons. (mW)	Max. output datarate (SPS)	Size (mm)	Price (USD)
		Pitch and Roll	Yaw									
TechIMU V4 [75]	Technaid	0.7 1.0	0.7 1.0	—	—	2000	—	—	280	500	36x26x11	—
Mti-3 [76]	Xsens	0.75 1.0	2.0 2.0	10	0.01	2000	0.1	200	44	1000	12x12x2.5	335.22 ¹
Mti-30 [77]	Xsens	0.2 0.5	1.0 1.0	18	0.03	450	0.015	60	400~550	2000	57x42x24	1460.00 ¹
Mti-300 [4]	Xsens	0.2 0.3	1.0 1.0	10	0.01	450	0.015	60	600	2000	57x42x24	—
UM7-LT [78]	Redshift Labs	2.0 4.0	5.0 8.0	—	0.005	2000	—	400	250	255	27x27x6.5	144.50
AHRS380ZA [79]	Aceinna	0.2 1.0	1.0 3.0	10	—	400	0.02	—	250	100	24x38x10	591.25 ¹
STT-IWS [80]	STT	0.5 —	2.0 —	—	—	2000	—	—	—	400	64x38x18	—
AHRS-8 [81]	Sparton	0.2 1.0	0.2 1.0	10.8	0.03	500	0.023	126	330	100	42x28x12	1360.00
InertiaCube4 [82]	Intersense	0.25 —	1.0 —	—	—	2000	—	—	240	200	37x28x14	600.00
VN100 Rugged [83]	Vectornav	0.5 1.0	2.0 2.0	10	0.0035	2000	0.04	140	200	800	36x33x9	1200.00 ²
BNO055 [47]	Bosh	—	—	—	0.014	2000	—	150	40	100	5.2x3.8x1.1	10.99 ¹
ADIS16465-3 [84]	A. Devices	NA	NA	6	0.007	2000	0.0036	23	150	2000	22x22x9	643.34 ¹
ADIS16490 [85]	A. Devices	NA	NA	1.8°/h	0.002	100	0.0036	16	300	4250	47x44x14	2417.81 ¹
LSM9DS1 [86]	ST	NA	NA	—	—	2000	—	—	13	952	3.5x3x1	6.14 ¹
Minimu V5 [44]	Pololu	— ³	— ³	—	0.007	2000	—	90	16.5	6664	20x13x3	15.95
MPU9250 [46]	Invensense	NA	NA	—	0.01	2000	—	300	9.25	8000	3x3x1	9.32 ¹

¹ From mouser.com, visualization date: 22/04/2018² Thermally calibrated to -40 to 85°C with USB cable. Price available at <https://www.vectornav.com/purchase/product/vn-100-rugged> accessed at 22/07/2018³ Pololu offers a simple data fusion package with no performance specification

2.5 REDUNDANT INERTIAL SENSING

Recently, the use of redundant inertial sensors, with the aim to improve orientation precision, has been explored by some research groups. In the next paragraphs is presented a list of some groups and their contribution.

Waegli et al. [10] explored real (not simulated) IMU redundancy to minimize orientation error. Their group developed a system using 3 Xsens Mti series (NL) to evaluate the orientation estimation performance gain of during the practice of sports (ski) and the orientation of a vehicle (motorcycle).

Their results showed a performance gain of 45% in the best-case solution, moreover, Waegli et al. indicate that the best geometry for redundant sensors is what they call *skew-redundant*; where the sensors are not at the same plane, although this geometry imposes size restrictions i.e. the sensors must not be at the same PCB.

Bancroft and Lachapelle [8], using Cloudcap Crista MEMS Grade IMU, explored three different methods to fuse the inertial data from the redundant sensors, that in a resumed manner, vary from fusing sensor observations (raw inertial data) to fuse Kalman Filter estimations. In most of the proposed filter configurations, the performance gain stalled for a configuration using more than 2 IMUs.

Skog et al. [87] proposed a Multi-IMU (MIMU) platform containing 14 operational 9DoF MPU9150 SoC (Invensense). Their system aimed to improve the orientation estimation for pedestrian tracking. Skog et al. state that the raw measurement standard deviation for a static sensor was reduced by a factor of $14^{0.5} \approx 3.7$, as it should be for a sensor model where the only error source is a Gaussian additive noise. Although, the dynamics dependent errors, e.g. non-linearities, g-sensitivity, and scale errors, are significant and not reduced by the 3.7 factor, hampering the final MIMU tracking performance.

Clausen et al. [6] proposed a system, named using of 4 NavChip (Intersense, US) sensors (3 axes accelerometer and gyroscope) aiming to improve position estimation during GPS failure during urban and rural traffic conditions. Their system was able to reduce the absolute position error in more than 20% (from 9 to 7 meters) during a 14 seconds GPS failure.

Waegli et al. [10] as well as Skog et al. [87], did not obtain the maximum theoretical performance gain with the aid of redundant sensors, which is a performance gain in the order of the square root of the number of redundant sensors. Such improvement is only possible if the sensor readings are only contaminated with Gaussian noise.

Waegli et al. [10] state that this might be the result of correlations between the inertial measurements as well as the correlations between the filter states, while Skog et al [87] state that the non-linear errors cannot be reduced by using a multi-IMUs platform (MIMU) of the same

brand. Thus, a hypothesis should be evaluated: Does two different IMUs (from two different vendors) creates the possibility to reduce not only the Gaussian noise, but also errors whose sources are non-linear?

It is worth to state that it was not found in the literature, redundant sensors platforms with different part-number sensors. In another words, the redundancy was always the accomplish using the same sensor, with the same non-linearity deviations and similar bias characteristics. The hardware that was developed include two 9 DoF IMU manufactured by different companies – Bosch and STMicroelectronics, such decision was taken aiming to reduce the error cross-correlation among the sensors.

3 MATERIALS AND METHODS

This chapter aims to describe and present the main features of the sensors modules; the orientation reference system and the algorithms that were used for fusing the inertial data providing an estimation of its orientation in reference to a global reference coordinate.

Bearing in mind the points briefly discussed in Section 1.1, a microcontrolled system was proposed with sensor redundancy, aiming to improve the orientation estimation performance. Such system is flexible, operating with different sampling rates and it is able to have its filter parameters edited by the user. The system was applied to different scenarios with different characteristics transmitting fused (orientation estimation) and raw data.

The proposed system runs in an embedded environment, with limited processing capabilities, while acquiring data from redundant sensors of different manufacturers. The last premise arose from the observation in the literature [10], [16] that fault measurements of sensors of the same manufacturer have cross-correlation, hampering the performance gain.

The orientation is transmitted to a server in a compressed form through a channel with limited throughput. It is important to have in mind that in many applications, such as human motion tracking, a sensor network is necessary, or at least, desirable.

Additionally, it was necessary to evaluate the accuracy of different inertial data fusion methods and the influence of sensor redundancy over the system accuracy. To make such evaluation possible, a Test Jig with two degrees of freedom and resolution of 0.1125° and a complete methodology to compare the results were also developed.

It is important to mention that all control loops were externally checked with the aid of oscilloscope, to evaluate if the rules of real-time control were not broken, assuring constancy of sampling rates.

3.1 HARDWARE RIMU v1

With the objective of developing a simple yet effective test platform with redundant IMU sensing capabilities, a two-layer printed circuit board (PCB) named RIMU v1 (Figures 4 and 5), with dimensions of 46x36mm, have been developed. The previously mentioned board has as core the 32-bit Atmel Cortex M0+ SAMC21E18A microcontroller, with the following key features:

- Four independent Serial Communication Interfaces (SERCOM) which may be configured as Two Wire Interface (TWI – also known as Inter-Integrated Circuit, or simply, I²C), Universal Synchronous Asynchronous Receiver Transmitter (USART), Serial Peripheral Interface bus (SPI), RS-485, among others.
- Native Controller Area Network (CAN) peripheral.
- Eight independent 16-bit Timer Counters (TC).

- 5 V tolerance.

The RIMU v1 integrates, as sensors, the BNO055 (Bosch, hereafter treated as BNO), LSM6DS33 and LIS3MDL (STMicroelectronics, hereafter treated as LSM and LIS, respectively). LSM and LIS are attached to the Minimu V5 (Pololu, US) for the ease of the soldering process. This assured a relative low cost of electronic components and PCB (around 35 USD) which can be seen as an interesting advantage for several applications, including human motion monitoring.

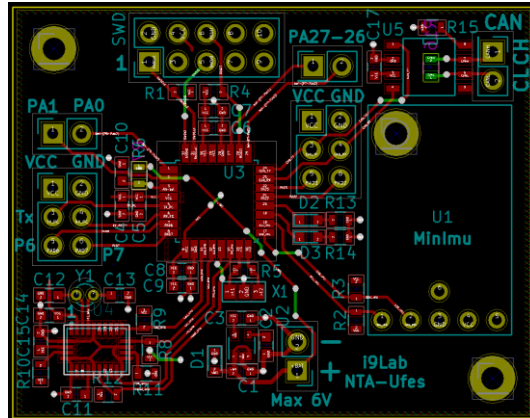


Figure 4: Illustration of the RIMU v1 PCB. Top trails are represented in red color while bottom trails are in green. Blue lines represent top silkscreen. Copper (bottom GND and top 3.3V) zones are hidden.

The BNO is a nine degrees of freedom (DoF) system on chip (SoC) with 3-axis accelerometer, gyroscope and magnetometer in addition to an embedded Cortex M0 that processes the data from the sensors, executes sensor calibration procedures and runs the proprietary BSX 3.0 FusionLib. The BNO may also output fused data in the form of quaternions, Euler angles and linear acceleration – without gravity [47].

The LSM is an integrated circuit (IC) composed of 16 bits 3-axis accelerometer and gyroscope, while the LIS is a 16 bits 3-axis magnetometer. The resulting RIMU v1 system has 18 DoF.

The data collected from these sensors are transferred online to a server using a 2.0 Bluetooth module operating over the SPP protocol or a Serial/UART adapter, both must be able to run at 230400 bps.

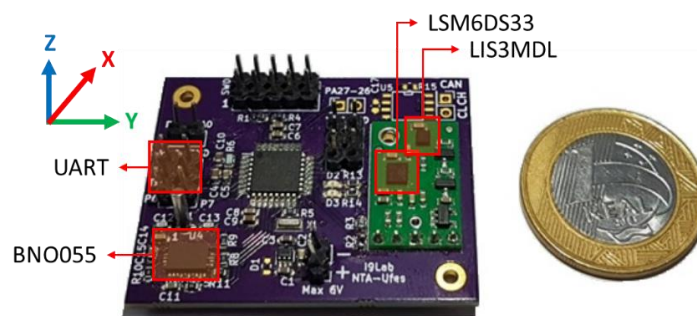


Figure 5: RIMU v1 module illustration highlighting the sensors and external communication port.

The server runs a MATLAB script capable to interpret the transmitted data, extracting inertial information and implement fusion algorithms. Further, the server can request the transmission of different sets of data and sampling rates. All possibilities of transmission configurations are listed as follows:

- a) BNO inertial and magnetic data (3D angular speed, linear acceleration and magnetic field), sampled at 100 Hz.
- b) LSM inertial data, sampled at 1 kHz.
- c) LSM and LIS inertial and magnetic data, sampled at 500 Hz.
- d) LSM and LIS inertial and magnetic data, sampled at 1 kHz and 100 Hz, respectively.
- e) BNO, LSM and LIS inertial, magnetic and fused (quaternion) data, sampled at 100 Hz.
- f) BNO calibration status.

In relation to LSM, its signals are internally sampled at 1 kHz and low-pass filtered before being sent to the server. The cutoff frequency of such filter is equal to half of the data transfer rate (50 or 250 Hz). This dissertation adopted the transmission configuration indicated in **e)** throughout all experiments. This mode was selected because it acquires data from three sensors, what makes possible forthcoming performance comparison, where inertial data comes from different sensors with different contributions.

It is important to mention that the timing of this process is controlled by a SAMC21E18A internal timer, consequently, the sampling frequency remains constant throughout the complete acquisition processes, independently of eventual server's operational system jitter.

During the test and application phase, the most relevant limitation was related to the Minimu's hardware. Due to its simplified design, the Minimu board limits the communication to the I²C interface, therefore, limiting the clock rate to 400 kHz in contrast to 10 MHz for the SPI protocol. As a result, the maximum sampling rates of LSM and LIS were limited to 1 kHz (practical limit), as the time length to read 12 bytes from LSM and 6 bytes from LIS is equal to 604 microseconds.

The Lack of dedicated float point unit (FPU) is also a significant issue, extending the execution time of float point operations. Such fact hampers the implementation of complex DFMs or high-order filters.

Another critical issue is the length of BNO's data reading operation that can vary from 640 microseconds to 4.24 milliseconds. Such fact is possible due to an I²C feature referred to as *clock stretching*. The *clock stretching* is characterized when the I²C slave (in this case the BNO), holds down the I²C clock line, indicating that it cannot provide data at the moment [88], therefore the I²C master must wait, extending the reading time. The BNO is a SoC which has its own Cortex M0 [47], to read data from BNO it is necessary that the master is able to do *clock stretching*.

The long BNO reading operation duration could hamper even further the data transfer rates. This issue was amended using a dedicate TC and I²C peripherals, dedicated interruption vector along with multi-priority interruption controller.

3.2 TWO DEGREES OF FREEDOM TEST JIG

Some previous researchers [27], [41], [58] validated their algorithms against a static reference, manually positioning their IMUs; therefore evaluating only the static performance of the DFM, disregarding the performance during the transition phase between two orientations. However, for many applications, such as gait analysis [89], upper limb human motion analysis [7], unmanned aerial vehicle (UAV) applications [90], the transition performance is also relevant.

Considering the high cost of orientation reference systems [11], [57] and the absence of an inertial database that would make possible compare the performance of the DFM, an orientation reference system was designed and built in this work.

The developed Test Jig (TJ), exhibited in Figure 6, have two DoF, enabling the evaluation of movements in more than one axis simultaneously and independently. The necessary torque to rotate each axis is provided by two step motors: NEMA 17 (part number 17HD34008-22B) and NEMA 23 (part number JK57HS56-2804-01), respectively positioned at the top and base of the TJ. Both motors have 200 steps per revolution. Step motors were adopted in the TJ project because of its elevated holding torque, reduced cost and control simplicity when compared to servomotors.

Two A4988SETTR-T step motor controllers (Allegro MicroSystems – US) [91] are used to electrically drive the NEMA motors (red modules at the right image of Figure 6). These motor controllers allow a 1/16 microstepping reducing motor vibrations [92] while improving the system resolution to 0.1125 degrees. They also provide current control mechanisms, allowing safe motors use.

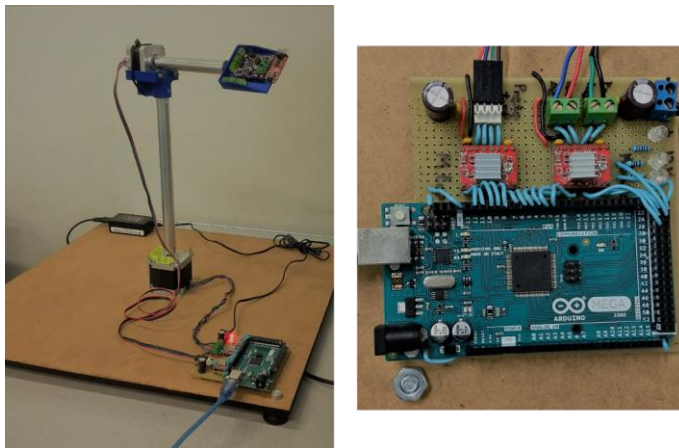


Figure 6: Test Jig (left) and Test Jig Control Board (right)

With the purpose to reduce the magnetic disturbance created by the motors, while preserving the TJ alignment, two machined aluminum shafts with 245 and 115 mm were projected. Furthermore, aiming to improve TJ vertical-align, four bubble levels were installed: two at the base motor frame and two at the RIMU platform.

The operation of TJ is based on an open-loop control system: the user configures a set of commands specifying the sequence of angles that will be described by each motor along with its respective maximum angular speed. This set of commands is then sent through UART to the TJ's microcontroller, an Atmel2560 microcontroller.

Each TJ motor will then uniformly accelerate at a rate of $360 \text{ }^\circ/\text{s}^2$ until reach the configured maximum angular speed. From this point, this specific motor will move at constant angular speed until reach the deceleration point, where it will uniformly decelerate at a rate of $360 \text{ }^\circ/\text{s}^2$ until stopping. The acceleration and deceleration rates were empirically set to enable high-speed transitions while reducing motor vibrations.

As long as each motor runs within its torque specification, the relative position of its shaft (in relation to its initial position) is known at all times without the need of feedback devices [92]. This special characteristic allows offline reconstruction of each motor Kinematic and angular position based on the equations of Angular Uniformly Motion (3.1) and Angular Uniformly Accelerated Motion (3.2), where θ, ω and α stand, respectively, as the angular position, velocity and acceleration.

$$\omega = \Delta\theta / \Delta t \quad (3.1)$$

$$\theta = \theta_0 + \omega_0 t + \alpha t^2 / 2 \quad (3.2)$$

$$\omega = \omega_0 + \alpha t$$

$$\omega^2 = \omega_0^2 + 2\alpha\Delta\theta$$

Table 2: Test Jig main characteristics.

Resolution	0.1125°
Minimum Angular Speed	10°/s
Maximum Angular Speed	720°/s
Acceleration and deceleration rate	360°/s ²
Maximum number of commands per motor	245
Base maximum turn in a single direction	720° (limited by software)

The adoption of the ATmega2560 is justified by the need for three independent TCs and the desire to develop a piece of equipment that is easy to use and maintain. Table 2 presents a set of TJ main characteristics.

The ATmega2560 firmware as well as the MATLAB scripts (those responsible to reconstruct the TJ kinematic) are available at the Author's Github page [93]. The TJ total cost is approximately 110 USD.

3.3 DATA FUSION METHODS AND ERROR MEASUREMENTS METHODOLOGY

Five DFMs were selected to be compared: Madgwick's [32] and Mahony's [30] originals algorithms, a CF version developed by Comotti [63], a MEKF developed by Maximov [94] and the BNO proprietary BSX 3.0 FusionLib. It is relevant to mention that the Maximov algorithm had its gyroscope bias update characteristic removed due to a non-identified error source that would drive the system to an unstable point. Such unstable point was reached after 10 minutes, for the gain matrices values that are used in this dissertation.

Those algorithms were selected, basically, due to their relevance. The papers that describe Madgwick's (2011) and Mahony's (2008) algorithms have, respectively, 377⁴ and 571⁵ citations, a clear indicator of their significance. At least one of different variations of Kalman Filter is analyzed as the fusion method in many papers, i.e., [6], [8]–[10], [28] and in commercial AHRS, i.e., [82], [83], whereas its variations are applied even in Nasa's spacecrafts [60]. Complementary Filters are pointed out as a lightweight alternative to Kalman Filters [58], additionally, Madgwick's and Mahony's algorithms are somehow inspired by CF. To conclude, the use of BNO made available the analysis of a commercial proprietary DFM, additionally, increasing the methods diversity.

Except for the BNO proprietary FusionLib, all algorithms have parameters that can be optimized. In order to carry out a fair and effective DFM performance comparison, each filter parameter must be optimized. Hence, two aspects must be defined: The Cost Function and the set of data that will be used as filter input, namely Excitation Data.

3.3.1 Cost Function and excitation data.

The cost function, also named as loss function, is the function that will map an event to a cost value. In this case, the cost function is the angle deviation between the DFM's output and the correspondent Test Jig (TJ) reference orientation, or simply orientation error. The Kinematic Tracking Error (KTE) has been selected as cost function because it is able to quantify not only the mean error deviation but also the smoothness of the filtering process [95]. The KTE equation is presented in (3.3), where φ represents the mean of the absolute error and σ^2 represents the orientation error variance.

$$KTE = \sqrt{\varphi^2 + \sigma^2} \quad (3.3)$$

The KTE was applied individually for each axis (Pitch, Roll and Yaw), returning a set of 3 costs. To allow the comparison and, consequently, the optimization, a single value must be return for each tested DFM's configuration. The average between the Pitch, Roll and Yaw cost was then taken as

⁴ Number presented by the IEEE Xplore: <https://ieeexplore.ieee.org/document/5975346/> Access date: 15/07/2018

⁵ Number presented by the IEEE Xplore: <https://ieeexplore.ieee.org/document/4608934/> Access date: 15/07/2018

the final cost. In this dissertation, the KTE and where mentioned, RMSE noise, both were always calculated using as basic unit degrees instead of radians.

It is intuitive to think that the DFM performance is directly related to its input data set, particularly, the set of movements that the RIMU performed. In a more accurate analysis, it is expected that, if the input data set includes fast transitions, considering an ideal and adaptive scenario, the DFM would trust more in the gyroscopes measurements, once accelerometer data would be contaminated with non-gravitational information. A similar event should happen when the magnetometer data is contaminated, as it is discussed in Section 4.4.

Alternatively, if the set of movements are composed essentially of very slow movements, one might expect that the accelerometer and magnetometer information should have greater significance than gyroscope information due to the long-term gyroscope bias drift.

Indeed Zamani et al. [55] conclude that the DFM gains are scenario dependent and generally, there is an inherent trade-off between conversion time and asymptotic angle estimation error: the smaller the conversion time, the greater is the asymptotic error.

Aiming to study the relation between DFM performance and gain values according to different movements patterns, the RIMU was exposed to three different angular speed patterns, henceforward named Slow, Mid and Fast-range profiles. The main difference between those patterns is the mean angular speeds, which are 13.45, 44.38 and 66.72 degrees per second for the Slow, Mid and Fast-range profiles, respectively. The set of movements of each pattern was randomly chosen, the only restriction imposed to the movement pattern was to return to the initial orientation in the end of the test.

Figure 7 presents the TJ orientation for the three aforementioned programmed movement patterns, while Figure 8 presents the TJ angular speed history. It is important to mention that the angle values were chosen to have two basic criteria: create three different mean angular speed profiles and have the initial end final orientations equal. Observe that the final pitch angle of the Fast-range profile is 360° , what is the same as the initial orientation after one complete turn.

Taking in consideration that the TJ has two DoF, the roll axis is not present in both figures because it is constant and equals to zero. A better visualization of the experiments can be found in videos uploaded to YouTube⁶.

⁶ Slow-range experiment video: <https://youtu.be/G5aqPF1DhF0>, uploaded at 15/08/2018.
Mid-range experiment video: <https://youtu.be/wQQRgsb8XQM>, uploaded at 15/08/2018.
Fast-range experiment video: <https://youtu.be/s53OG844FJ8>, uploaded at 15/08/2018.

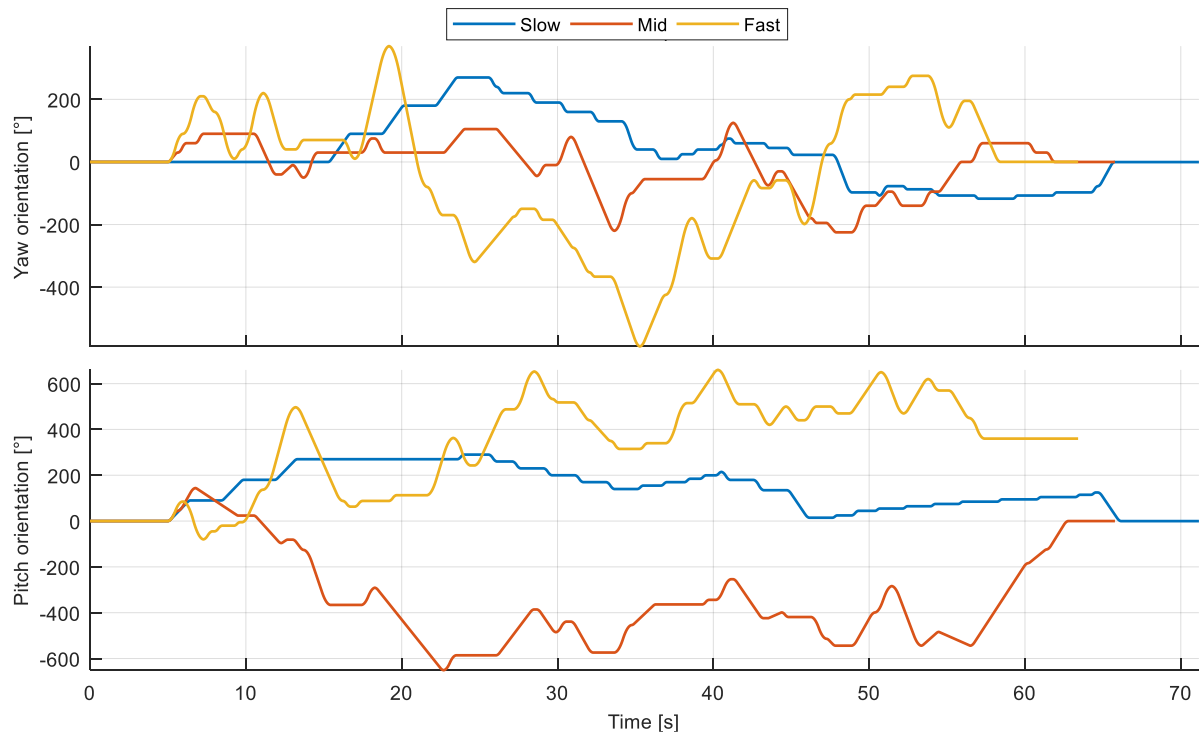


Figure 7: TJ orientation during the DFMs evaluation experiments. The final DFM output will be truncated between -90° and 90° for Roll and -180° to 180° for Pitch and Yaw. The truncation was not performed to facilitate the scenarios comparison.

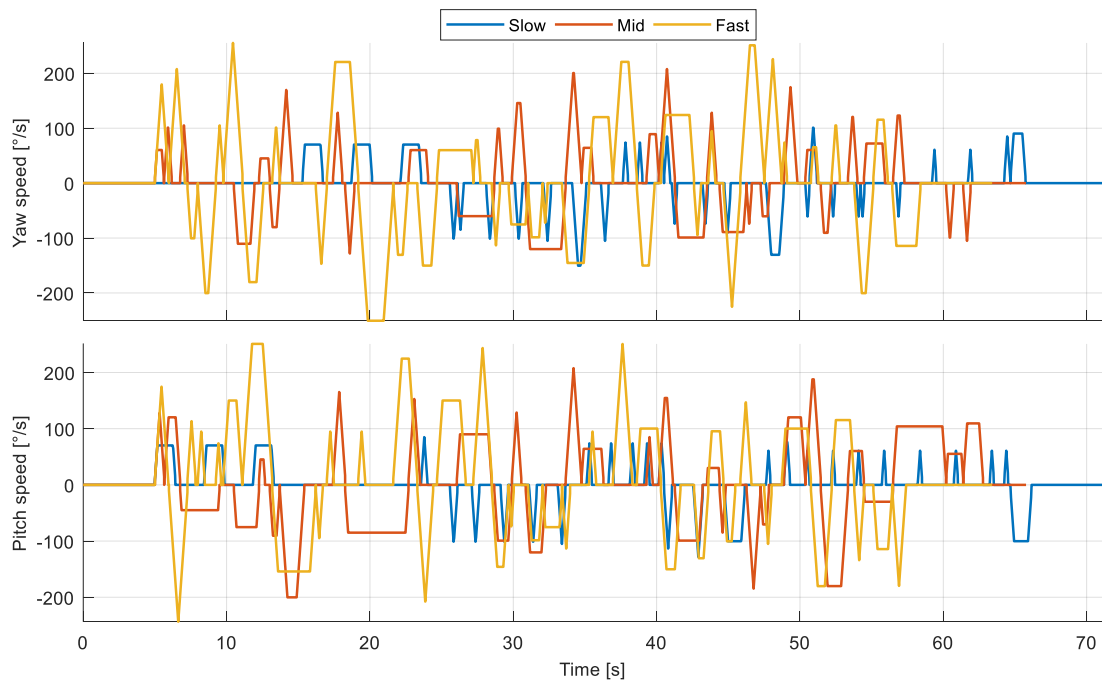


Figure 8: TJ angular speed during the DFMs evaluation experiments.

3.3.2 Optimization methods

Whereas the Madgwick's, Mahony's and CF algorithms have a single optimizable parameter, an exhaustive search was applied to find the parameter values that results in the best performance. The exhaustive search algorithm consists of systematically enumerating a large number of possible candidates for the DFM solution and checking whether each candidate results in a smaller DFM error or not.

For the CF, the exhaustive search had the range of 0.0023 up to 0.999, varying the crossover factor in steps of 0.0033. Madgwick's and Mahony's algorithms had their parameters, respectively Beta and Kp, changed from 0.01 to 3 in steps of 0.01.

For the Kalman Filter optimization, an adapted version of Genetic Algorithm (GA) presented by Eshelman and Schaffer [96] was implemented. This version had a population of 40 individuals; each individual had six chromosomes representing the superior and inferior diagonal elements of Kalman's error and measurement noise covariance matrices, initial gyroscope bias error and initial gyroscope random error, as it is exhibited in Table 4. Table 4 also presents the search limits, that were empirically chosen to contemplate a large search area but not large enough to hamper the GA conversion.

The evolution started from a randomly spread population with uniform density probability throughout the search space. The evolution was realized by means of BLX- α crossover [97], with α equals to 0.25 and mutation rate of 5%. The algorithm is elitist: it always preserves the best solution.

The implemented GA version has an exclusion criterion of Kalman conversion: when it is not possible to calculate the inverse of any matrix, the individual is then substituted by a new one, with randomly selected chromosomes. The stop criterion was 25 generations, a number empirically chosen to allow enough time to the optimization evolve but not exaggeratedly long, what would overly increase the risks of overfit.

Table 3: GA individual description and search limits

		X_{\max}	X_{\min}	
GA individual	X(1)	Sup. diagonal of measurement noise covariance matrix	1	0.005
	X(2)	Inf. diagonal of measurement noise covariance matrix	1	0.005
	X(3)	Sup. diagonal error covariance matrix	0.1	5×10^{-5}
	X(4)	Inf. diagonal error covariance matrix	0.1	5×10^{-5}
	X(5)	Initial gyroscope bias error	0.01	5×10^{-5}
	X(6)	Initial gyroscope random error	10^{-5}	5×10^{-8}

3.3.3 Test-Jig-RIMU alignment and synchronization

Aiming to produce an equitable comparison between the TJ orientation (reference) and the RIMU orientation, which is estimated by each DFM, a Test-Jig-RIMU alignment and synchronization process was developed and is resumed in Figure 9. This process will be explained in this section.

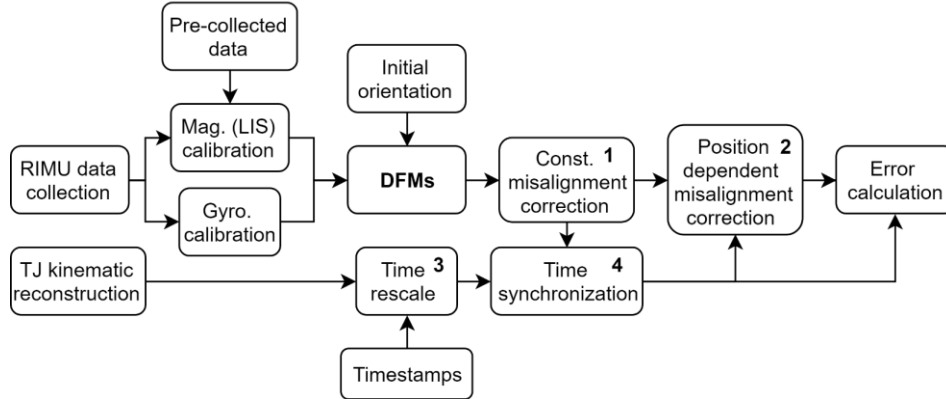


Figure 9: TJ-RIMU alignment and synchronization process flowchart.

Two sources of external errors affect negatively the orientation comparison between the TJ and the sensor (RIMU): physical misalignment and time dis-synchronization. With the purpose of precisely evaluate the performance of the orientation estimation process, it is necessary to reduce the negative influence of those two aspects over the final error evaluation.

There are two types of physical misalignment: a constant factor and a jig-orientation-dependent factor. The constant misalignment factor is due to the difference between the jig orientation-zero (zero yaw, pitch and roll) and what each DFM define as orientation-zero.

The correction of this source of error is completed averaging few seconds of the initial DFM quaternion orientation (using the method proposed by Markley et al. [33] previously explained in Section 2.1.3.3) as shown in equation (3.4). Then, each DFM quaternion output is pre-multiplied by the complement of the averaged initial quaternion, as shown in equation (3.5). Where q_0 is the average initial quaternion orientation, q^k stands for the quaternion output of a single DFM iteration and k is the index of a specific iteration. This process is represented by the box number 1 in Figure 9.

$$q_0 = \text{avgMarkley}(q^{k_0}:q^{k_0+\Delta k}) \quad (3.4)$$

$$q^k = q_0^{-1} \star q^k \mid k = 1: \text{end} \quad (3.5)$$

To reduce the initial DFM conversion time while providing an equitable starting point, a given DFM was fed with the quaternion orientation that this specific DFM would output after a long period resting at that initial position. Therefore, for all DFMs the initial estimation error tends to zero.

The orientation-dependent misalignment has its origins in equipment misalignments and production process deviations, i.e., shaft connection misalignment, motor inclination and sensor misalignment. To reduce the influence of this source of error, a procedure was developed, it is represented by the box number 2 in Figure 9, and it is discussed as follow.

With the sensor already positioned at the TJ, the set was slowly rotated in steps of 10° for each axis separately (Yaw first, then Pitch), with a long rest period between each rotation. The average orientation during the rest phase of each analyzed DMFs was then calculated. The difference between the average of all DMFs and the TJ orientation was considered the orientation-dependent misalignment. A fourth order fit was then calculated for each axis enabling the correction of this error for future tests as function of TJ orientation.

The aforementioned process is illustrated in Figure 10 and Figure 11 that presents the original excitation data and the fourth order fit, respectively. The abrupt transition in the center of yaw plot (top) of Figure 10 is due to the Euler representation, that truncates the angle values between -180 and 180 degrees. Additional relevant aspect that can be observed in Figure 10 are the multiple peaks in the roll and pitch plots, those are results of the non-steady phase of the test. It is relevant to mention that the center of Figure 11 represents the TJ's initial position (origin) and due to the constant misalignment correction process, it has a small error.

With the purpose to reduce the synchronization errors, two actions were taken. The first one was rescaling the TJ reconstructed time vector taking in consideration timestamps attributed by the MATLAB to confirmations that were sent by the TJ's microcontroller, such process is represented by the box number 3 in Figure 9.

The second action consists of removing the constant delay between each DFM output and the reconstructed TJ orientation by calculating the highest cross-correlation lag between those two signals, then removing the calculated lag, represented by box number 4 in Figure 9. Similar approach was also adopted by Kok et al.[98].

The gyroscope calibration is explained at Section 4.1.3 while the magnetometer calibration was realized using the algorithm developed by Mucciaccia [99] using as reference a pre-collected set of magnetometer (LIS) data.

The next chapter will present the results of all experiments that were performed, aiming to evaluate the TJ as a reference and the RIMU performance over different aspects, enumerating: three different movement profiles at the TJ, long-term performance with temperature variation, when it is exposed to magnetic disturbances, and a static performance evaluation.

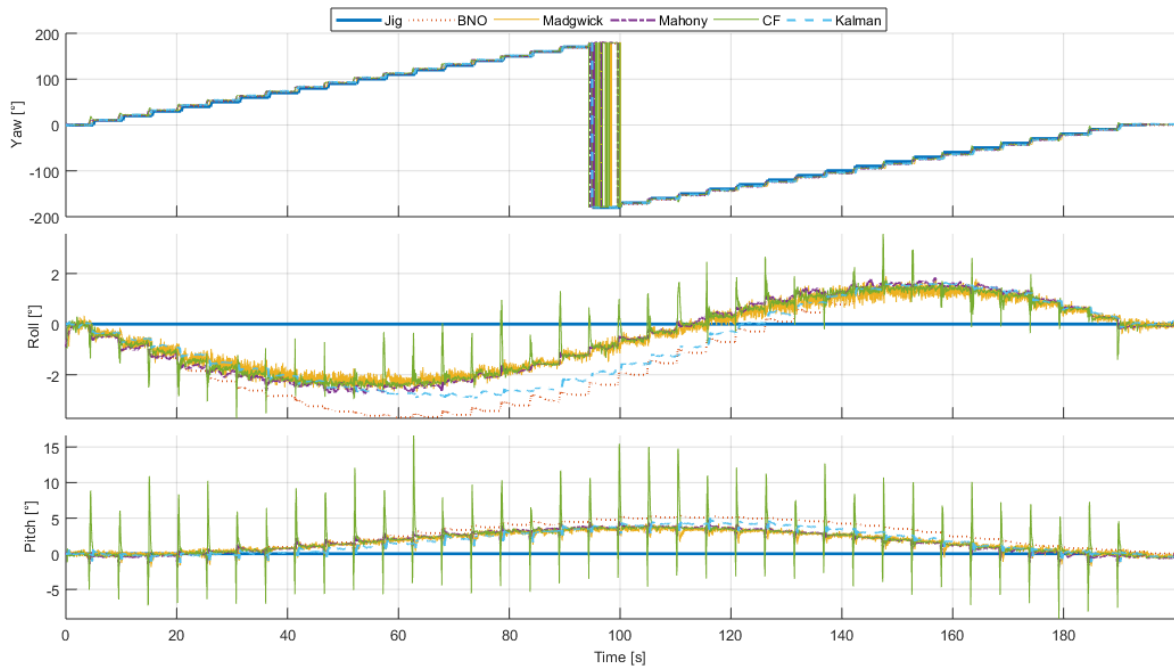


Figure 10: Excitation data for the Yaw-alignment process.

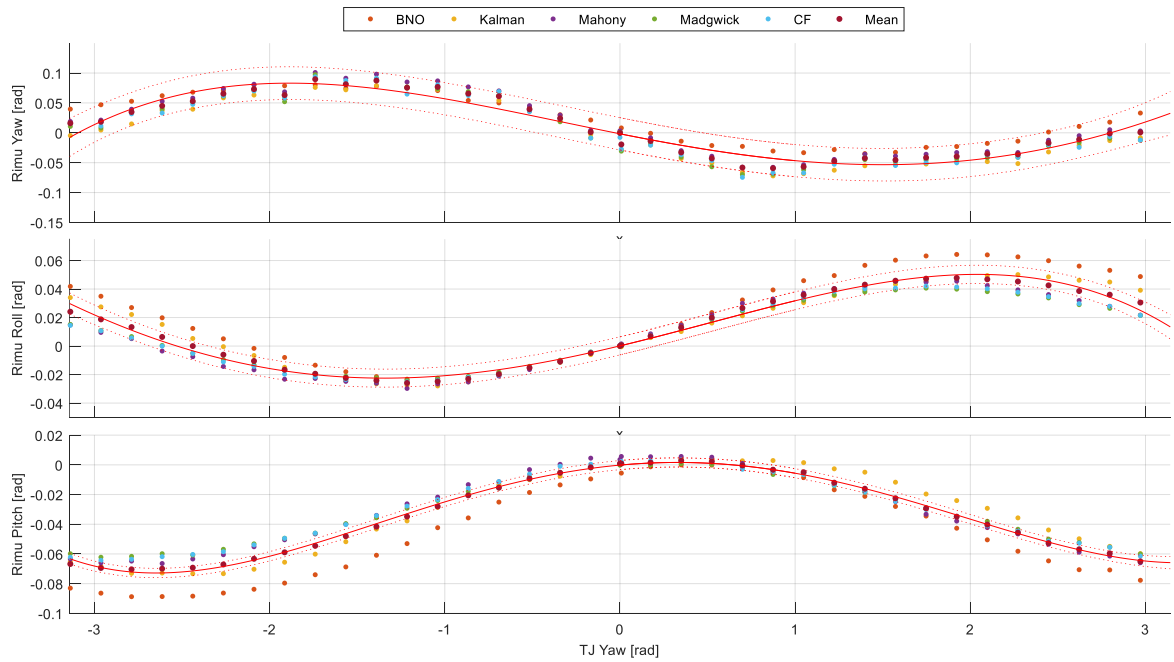


Figure 11: Orientation-dependent misalignment as function of TJ Yaw orientation. Each vertical coordinate of the plots represents the respective orientation error. The red line represents the fourth order fit while the red dashed line represents the 95% confidence intervals.

4 EXPERIMENTS AND PERFORMANCE EVALUATION

4.1 TEST JIG EVALUATION

A natural and necessary phase of an item development process is the evaluation of the performance of this specific item. Regarding the TJ, two aspects must be analyzed: the capability to perform and reconstruct a given movement, and, the influence of motors over the sensor measurements.

4.1.1 Kinematic reconstruction and Jig speed control performance evaluation

The first intrinsic TJ's limitation is the capability to rotate at a given angular speed; such limitation is imposed by its principle of operation: steps motors controlled by a digital system. Such restriction comes from the truncation of microcontroller's clock, allowing only a specific set of angular speed.

The digitalization of the motor speed control results in an error during the offline speed reconstruction phase, such error is expressed in Figure 12. When the angular speed rises, the time interval and the number of the microcontroller's clock cycles between consecutive steps are reduced, increasing the remainder after the division of ideal step interval and the practical step interval (the last is directly related to clock interval). The described behavior causes the rise of error module for higher angular speed, as can be observed in Figure 12.

It is relevant to mention that the angular speed error, introduced by such digitalization does not exert influence over the angle described by the motors nor by those estimated by the kinematic reconstruction script. The control and reconstruction are based on the number of steps that are performed by the motors, therefore, the final angular displacement of each motor is estimated precisely.

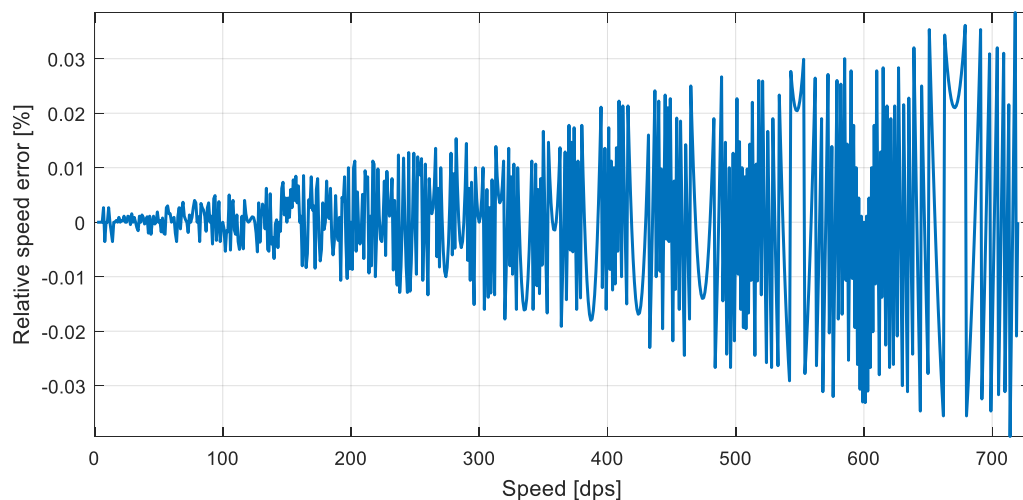


Figure 12: Relative TJ speed error over its all speed range.

Instead, the estimation uncertainty is expressed in terms of a task duration, which is latter minimized in the TJ-RIMU synchronization phase as it was explained in Section 3.2.

In addition, the angular speed error has a positive mean of only $3.11e-4$ degrees per second, such a low deviation from zero angular speed assures also a very small deviation in the final time estimation, especially if different angular speeds are selected throughout an experiment.

4.1.2 Motor influence over Magnetometer readings

The objective of this experiment is to evaluate the influence of the motors coil current and motors presence itself over the magnetometers' readings. It is important to remember that the Test Jig uses step motors and this kind of motor has permanent magnets in its rotors.

The setup consists of executing the BNO's magnetometer calibration procedure near to its final position, which is exhibited by Figure 13. Then, the sensor was positioned in a steady and non-magnetizable platform, which is placed near the motors. The experiment follows the subsequent order, which is easily visualized in the recorded video⁷:

- a) Start the RIMU data collection;
- b) Energize the motors keeping both steady for 7 seconds;
- c) Turn the base motor 360 degrees counterclockwise (CCW) at 60 dps (degrees per second) maintaining the top motor steady;
- d) Small pause;
- e) Turn the top motor 360 degrees CCW at 60 dps preserving the base motor steady;
- f) Small pause;
- g) Turn the base and top motors 360 degrees clockwise and CCW, respectively, and simultaneously, both at 60 dps;
- h) Repeat the steps from **b)** to **g)** inverting the motor turning direction.

Figure 14 presents the LIS and BNO's magnetometers readings. To simplify the visualization and comparison, the signals presented in Figure 14 had their average removed. Moreover, the BNO is set to the NDOF_FMC_OFF⁸ fusion mode [47], while LIS readings are calibrated according to the algorithm proposed by Mucciaccia [99] using as reference a set of pre-collected samples. The calibrated data from BNO and LIS magnetometers are used throughout the tests of this dissertation.

⁷ Video available at <https://youtu.be/m4sgaolz10Y>, accessed in 18/05/2018.

⁸ Bosch proprietary fusion mode with Fast Magnetometer Calibration turned off [47]

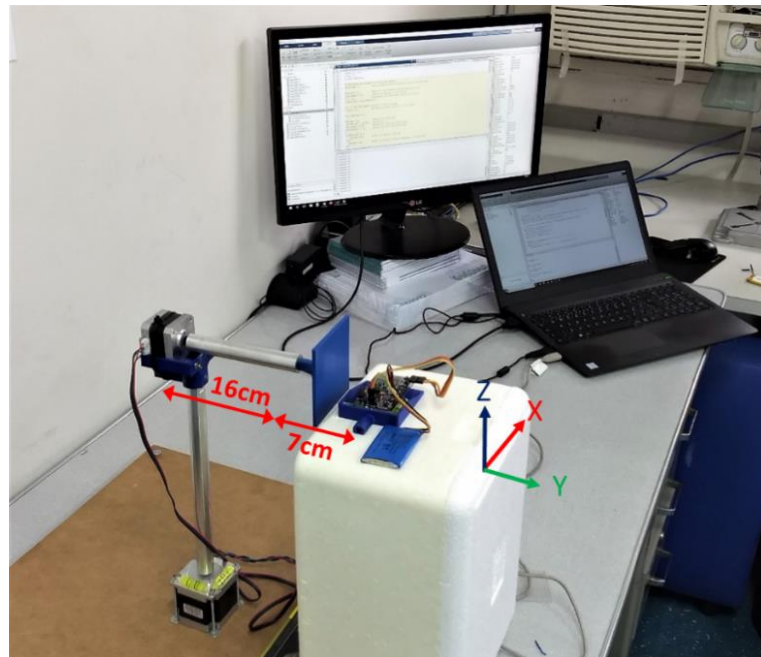


Figure 13: Setup of the experiment to evaluate the influence of the motors over the magnetometer readings.

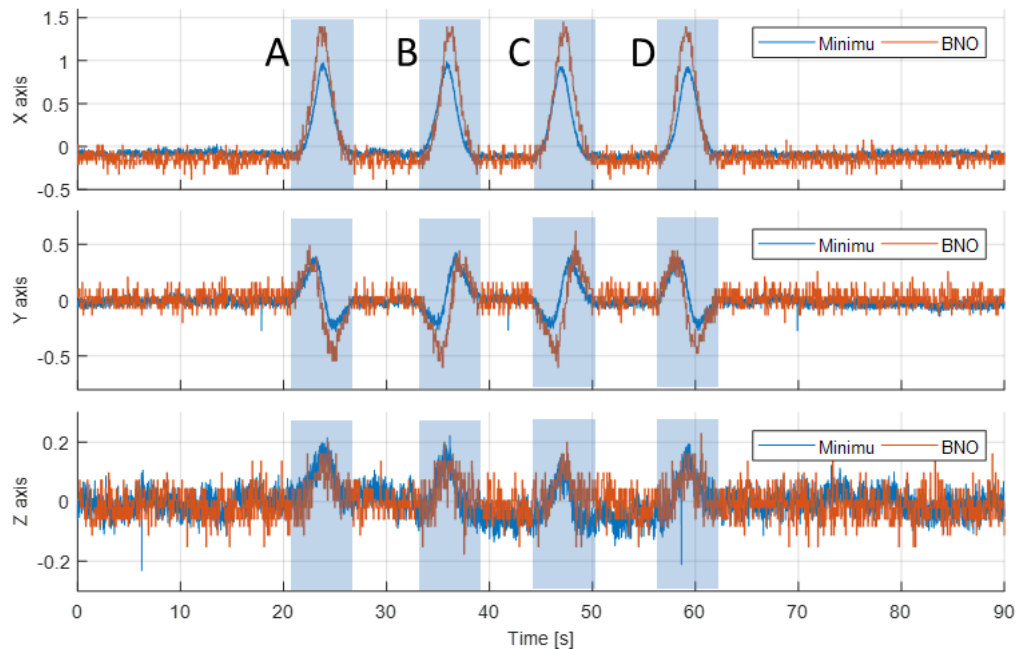


Figure 14: Magnetometer readings with average removed, a lower resolution of BNO magnetometer can be noticed. The coordinate axes are dimensionless. Minimu represents the LIS magnetometer.

It is possible to note only four substantial signals perturbations in all axes, they are the consequence of the **c**) phase (Figure 14, **A** and **C** perturbations) and **g**) phase (Figure 14, **B** and **D** perturbations). Disregarding the blue zones in Figure 14, there is not a significant deviation from the mean. Considering this, one can conclude that both motors coil current does not exert influence over the magnetometer readings.

That is because there is not a significant change in the initial and final phases of the signal exhibited in Figure 14 nor during the **e**) phase. In all those listed moments, only the motor current varies, but not the magnetometer readings. The factor that exerts a major influence over the magnetometers readings is the orientation of the top motor in relation to the RIMU position, what actually is varying during the **A, B, C** and **D** phases of Figure 14.

The position of the top motor relative to the sensor during the orientation experiments, as observed in Figure 6, is constant. Therefore, it is possible to minimize the motor orientation influence through a correct calibration process. Otherwise, the yaw deviation angle can be as large as 22 degrees, which is the deviation found for the BNO's proprietary algorithm during this experiment.

4.1.3 Jig vibration evaluation and gyroscope calibration

Step motor vibration is a long-date and well-known issue [100]. It is mainly related to the principle of operation of step motors and winding currents [101], thus its characteristics change for each motor-load pair.

Aiming to describe the effects of TJ motor vibration over the accelerometer and gyroscope measurements, a rotation test over the full motor angular speed range was performed.

For the purpose of evaluating the vibration characteristics during a specific angular speed, Angular Uniform Motion should be achieved and maintained for a reasonable period. Then, the RIMU was exposed to seven angular speed steps with an acceleration and deceleration phase between each step, as can be noticed in the Y-axis of Figure 15.

Due to the physical connection that must exist between the top motor and the power source (see the power cable in Figure 13), it is not possible to turn the base motor multiple times, making it impossible to the base motor to reach and maintain Angular Uniform Motion for the full range of angular speed. Hence, only the top motor had its vibration characteristics analyzed. The sensor configurations are set as follows:

- BNO was configured in NDOF_FMC_OFF. BNO also had its sensors (magnetometer, accelerometer, and gyroscope), locally calibrated just before the experiment.
- LSM experienced two configurations:
 - First, gyroscope and accelerometer raw data were directly transmitted to the server at a rate of 100 Hz (named *LSM non-filtered*).
 - Second, gyroscope and accelerometer raw data were sampled at a rate of 1 kHz, the microcontroller applies a second order Butterworth low-pass filter with cutoff frequency of 50 Hz (half of sampling rate). The data were then resampled and sent to the server at a rate of 100 Hz. The choice of Butterworth filter was made because this kind of filter has the frequency response as flat as possible in the passband. This process is presented as *LSM filtered*.

Figures 15 and 16 present the results of the previously described experiment for the gyroscope and accelerometer measurements, respectively. Examining these figures, it is possible to observe that the LSM has a high sensibility to the noise generated by the motors, and, the positive effect of the filtering process over its data quality.

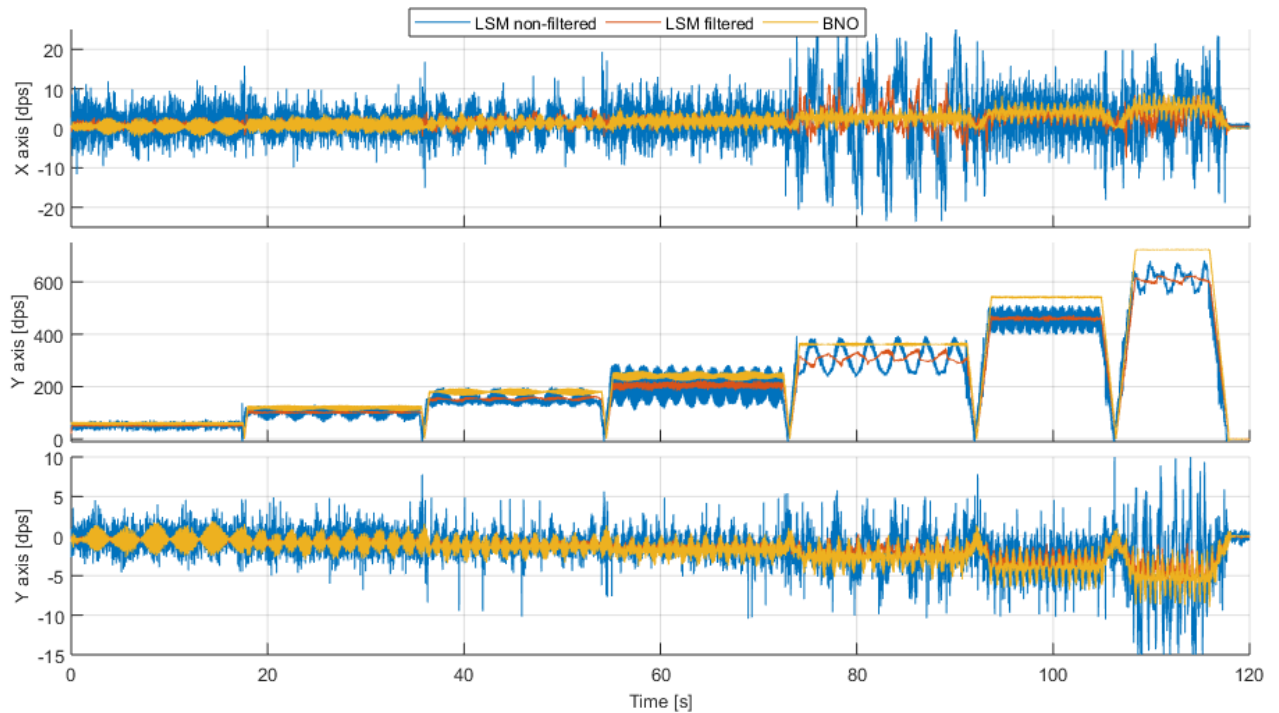


Figure 15: Gyroscope measurements during the vibration evaluation test.

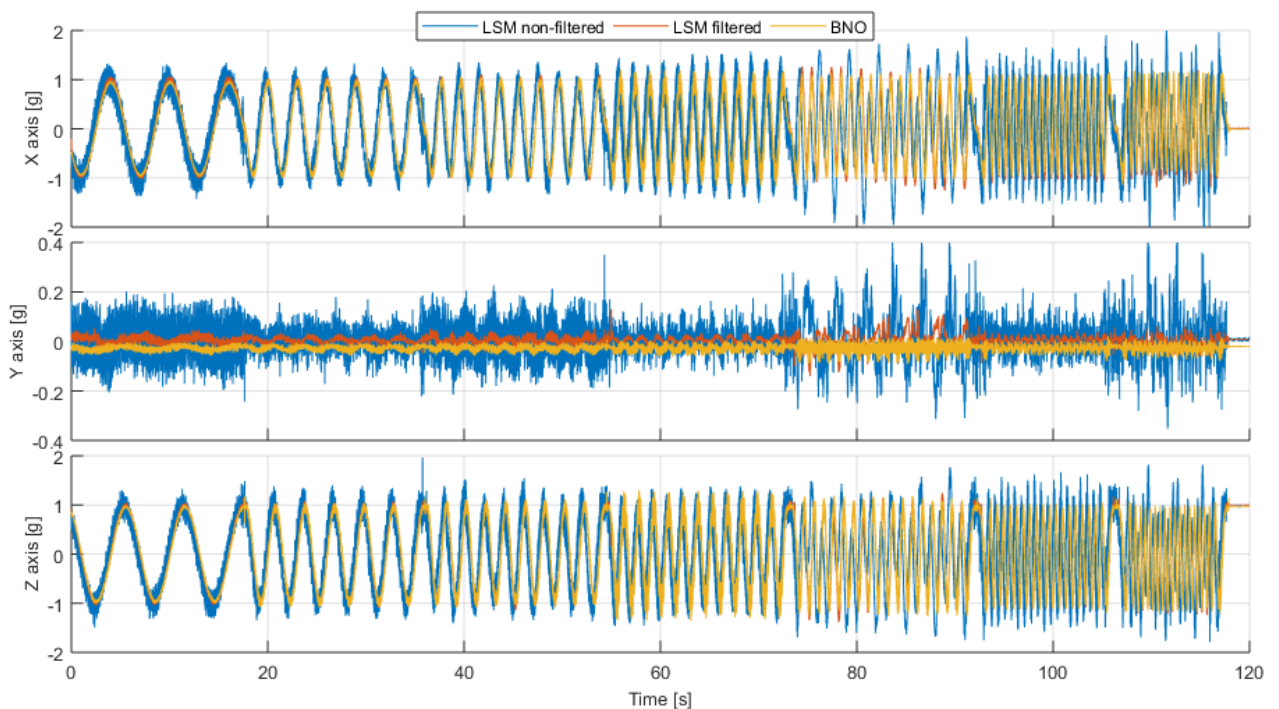


Figure 16: Accelerometer measurements during the vibration evaluation test.

It is relevant to mention the presence of Cross Axis Sensitivity (CAS), which expresses itself by the correlation between the measurements of two axes, in this case, the correlation between the Y-axis and the other axes of Figure 15. The CAS can also be observed in the Y-axis of Figure 16.

Even though the BNO presents in its datasheet [47] high levels of CAS (2%) and Sensor Alignment Error (2°), it is not possible to conclude that the previous BNO's characteristics are the source of such an error since a perfect TJ alignment is not guaranteed. The LSM datasheet [102] does not provide information related to CAS nor to Sensor Alignment Error.

Analyzing BNO Y-axis data in Figure 15 it is also possible to extract, through a linear fit, that the angular acceleration module is $359.6 \pm 1.4 \text{ }^\circ/\text{s}^2$ (95% confidence bounds). Such fact is one more indicator of the correct functionality of the TJ.

Additionally, it was possible to observe, in preceding stages, that the use of internal LSM filters creates signal distortion, more precisely, some LSM samples had their values drastically altered during a single sample, returning after, to normal levels. As consequence, no internal LSM filter was used.

Another evident conclusion that may be made analyzing Y-axis data of Figure 15 is that LSM and BNO gyroscopes do not measure the same angular speed, such discrepancy is quantified in Table 4. Indeed, previous work [103] has also pointed out such discrepancy, solving the problem adjusting the LSM output through a linear regression fit.

The implemented process to adjust the LSM gyroscope output consists of removing the static sensor output (bias) and calculate a first order fit between the LSM-filtered mean (presented in Table 4) and the programmed motor speed. The result of this process is Equation (4.1), where ω_{cal} is the compensated angular speed, while ω_{LSM} is the raw angular speed read from LSM. The calibrated LSM angular speed was used in all DFM instead of LSM raw angular speed data.

$$\omega_{cal} = 1.1692\omega_{LSM} - 6.7045 \text{ (dps)} \quad (4.1)$$

Table 4: Mean of angular speed (in degrees per second – dps) for each step of Figure 15.

TJ angular speed	BNO mean	LSM mean non-filtered	LSM mean filtered	LSM calibrated
60	60.15	56.63	56.75	59.65
120	120.38	108.01	107.97	119.53
180	180.38	158.88	158.51	178.63
240	240.55	209.85	210.11	238.96
360	361.04	312.39	319.39	366.73
540	541.34	464.64	464.69	536.61
720	721.85	617.63	621.44	719.88

4.2 SENSOR PERFORMANCE AT THE TEST JIG

Section 3.3 presented the methodology used to evaluate and optimize the DFMs. This section presents the results of such evaluation.

4.2.1 Slow-range profile experiment

Before compare the DFMs performances, it is necessary to determine which set of sensor readings would be used as DFMs inputs, henceforth named Input Data Set (IDS). Such selection was completed analyzing the best performance of CF, Mahony's and Madgwick's algorithms according to different data sets from different sensors. Eight scenarios were tested:

1. Data solely from BNO.
2. Linear acceleration and angular speed from LSM, magnetic field acquired from LIS.
3. Linear acceleration and angular speed from BNO, magnetic field acquired from LIS.
4. Linear acceleration from LSM, angular speed from BNO and magnetic field acquired from LIS.
5. Linear acceleration from BNO, angular speed from LSM and magnetic field acquired from LIS.
6. Linear acceleration and angular speed calculated through simple average of LSM and BNO readings while the magnetic field was acquired from BNO.
7. Similar to 6, but the magnetic field was acquired from LIS.
8. Data calculated through simple average of all sensors.

Due to its high number (six) of optimizable parameters, the implemented version of Kalman Filter demands a heuristic method to be optimized. As consequence, the optimized set of parameters change for every GA execution, changing also the Kalman performance. As a result, statistical methods are required to compare the performance of each scenario, demanding also long execution times. Therefore, for sake of simplicity, the Kalman Filter was left out of the selection of the best IDS among the proposed scenarios.

Table 5 summarizes the performance, in terms of KTE, while it presents the best-found coefficients values for each DFM according to the input data scenario. At this same table, it is possible to note that the best value of the optimizable parameter (Crossover factor, Kp and Beta) changes according to the excitation data, therefore, indicating that the best-case value is directly linked with the data precision. Still at Table 5, it is possible to observe that the sensor redundancy, alone, can reduce the KTE up to nearly 51% (Madgwick scenario 2 vs scenario 8).

Figure 17 presents the KTE as a function of optimizable parameters, namely, Crossover Factor, Beta and Kp for, respectively, the Complementary Filter, Madgwick's and Mahony's Algorithms. The abrupt variations presented in all plots and for all IDS are, probably, results of the time synchronization stage, that analyzes the cross-correlation among the TJ reference and the DFMs

output as it is explained in Section 3.3.3. Such abrupt variations were not present before the time synchronization stage.

Table 5: Best-case filter parameter according to the input data scenario for the slow-range movement profile.

Scenario	CF		Mahony		Madgwick	
	Crossover	KTE	Kp	KTE	Beta	KTE
1	0.990	2.625	0.620	2.419	0.030	2.484
2	0.970	2.701	0.770	2.455	0.240	2.817
3	0.963	2.837	0.310	2.841	0.830	3.133
4	0.973	2.590	0.420	2.408	0.020	2.784
5	0.950	2.882	0.960	3.024	0.920	3.050
6	0.990	2.540	0.400	2.055	0.020	2.208
7	0.967	2.159	0.800	2.257	0.590	2.355
8	0.977	1.532	2.630	1.507	0.210	1.391

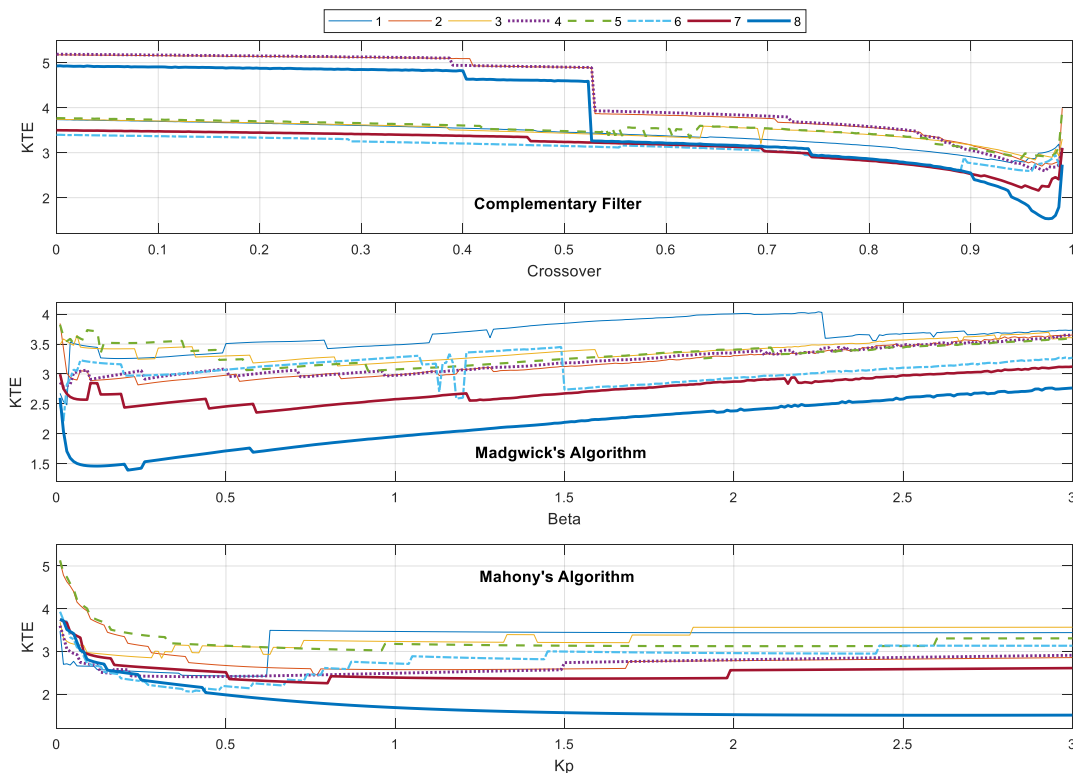


Figure 17: Kinematic Tracking Error as function of each optimizable parameter for their respective input data scenarios (1 to 8) for the slow-range profile.

Figure 17 also demonstrates how important it is to correctly tune the optimizable parameters, for instance, the CF performance improvement of more than 3 times taking into consideration the IDS proposed by the scenario 8. Likewise, Madgwick's and Mahony's Algorithms had gains of approximately twice.

Additional relevant aspect regarding the DFM analyzed in Figure 17 is how critical it is to tune a particular DFM. A qualitative analysis can be done by simply analyzing how the DFM error evolves according to the parameter variation. In other words, one must analyze the performance derivative near the best-case performance point. Hence, it is possible to conclude that the Mahony's Algorithm is easier to tune compared to CF and Madgwick's Algorithm since its performance is not drastically changed for a small change in the Kp value. Alternatively, the CF is heavily impacted by even a small change in the Crossover Factor.

Figure 18 displays the DFM outputs for the slow-range movement experiment⁹, including the already optimized (using GA) version of the implemented MEKF. All DFM estimates the orientation using quaternions as mathematical representation. The output quaternions are transformed into Euler angles using the `quat2angle` MATLAB function, as it was already mentioned in Section 2.1.3, with the `zxy` rotation order. This rotation order was chosen to avoid gimbal lock for the specific configuration of the experiments described in this section. The `zxy` rotation order limits the angles representation to $\pm 180^\circ$ for the yaw and pitch axes and $\pm 90^\circ$ for the roll axis, then any discontinuities such the one presented in the yaw axis (first plot) of Figure 18 near 20 seconds are caused by the formerly mentioned truncation process.

Figure 19 details the deviations of each DFM. It is relevant to note that the error signal of every DFM has many peaks, which are strongly correlated with moments when the TJ moves (rotation and translation).

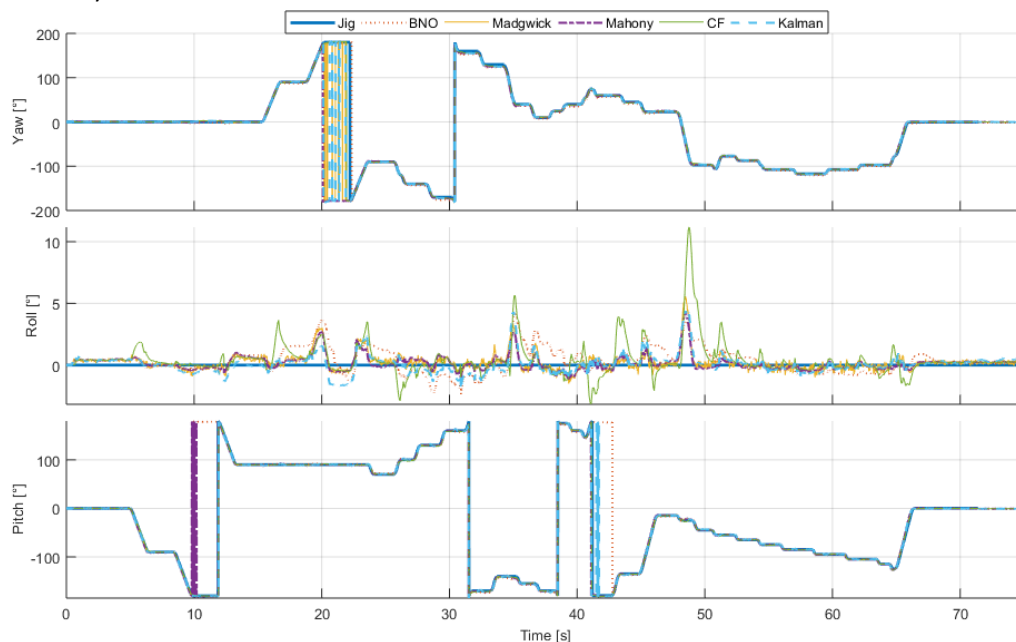


Figure 18: DFM performances for the slow-range motion profile using as input the data composition according to scenario 8. Euler angles represented in the `zxy` rotation order.

⁹ Slow-range experiment video: <https://youtu.be/G5aqPF1DhF0>, uploaded at 15/08/2018.

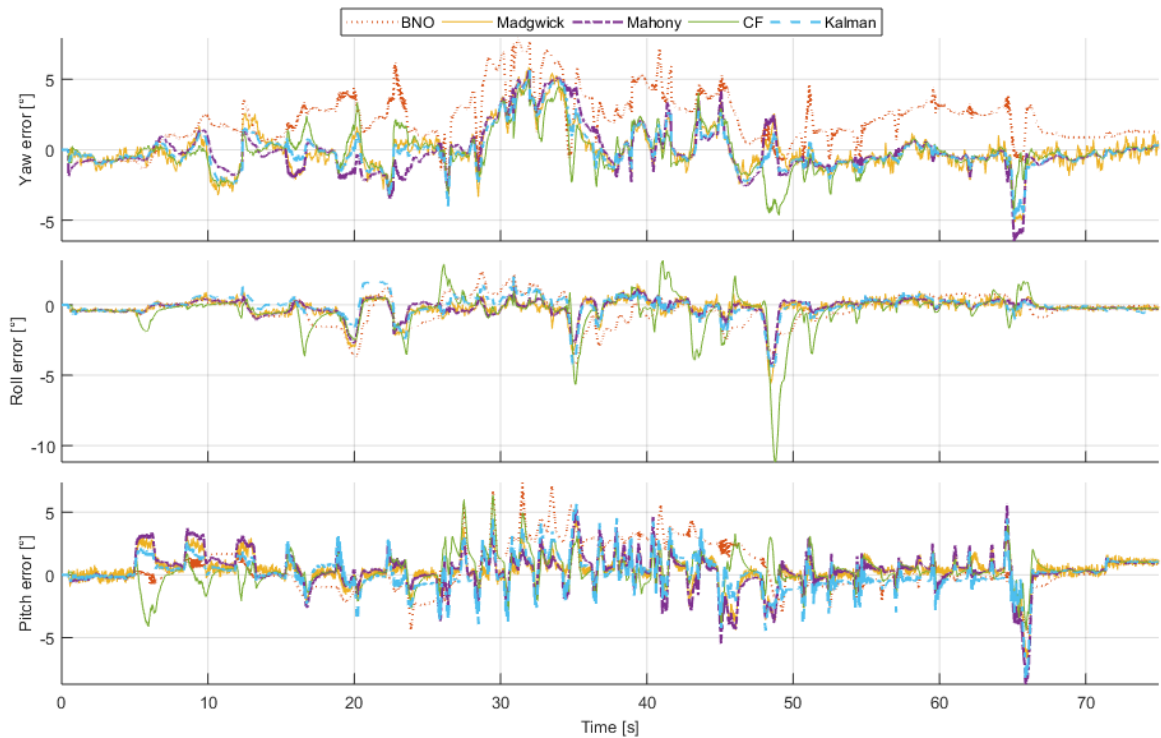


Figure 19: Deviations from the reference for each DFM for the slow-range motion profile using as input the data composition according to scenario 8.

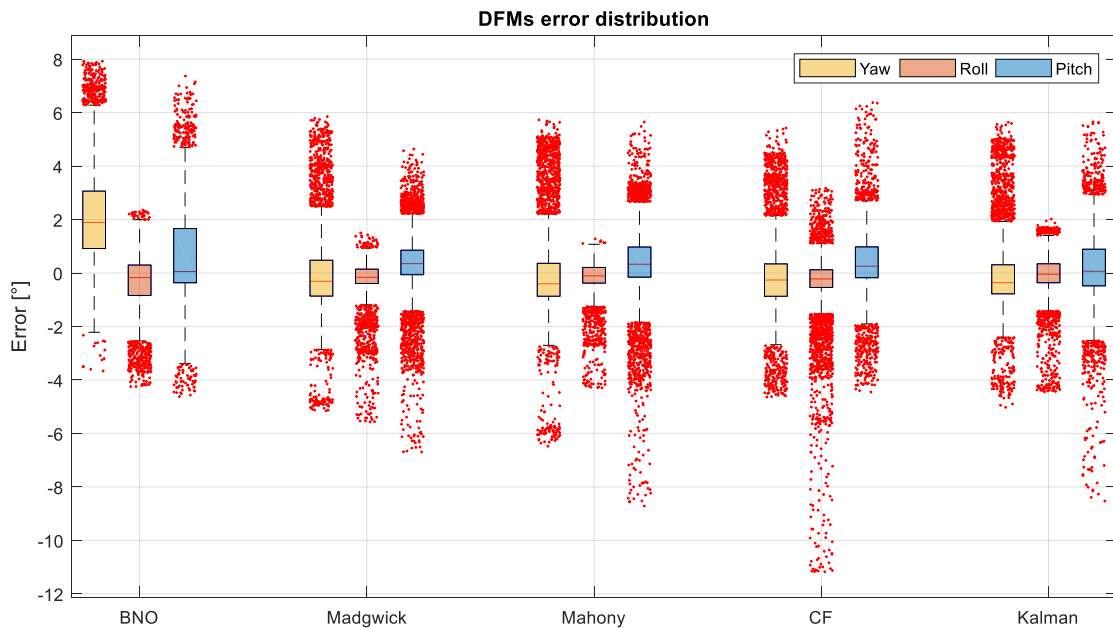


Figure 20: Boxplot of error distribution for each DFM axis considering the slow-range profile as IDS. A total of 7500 samples are represented in each axis of each DFM.

Figure 20 presents the boxplot of the deviations presented in Figure 19. Boxes of Figure 20 represent 25th and 75th percentiles of the sample's error, the center red line of each box represents the median of each error set; whiskers are extended up to ± 2.7 times the data

standard deviation, what represents 99.3 percent coverage if the data is normally distributed. The remaining errors are considered outliers. All samples are represented.

In an attempt to resume the best-found performance of all evaluated DFMs, Table 6 exhibits the KTE and RMSE for each axis as well as their mean values. The presented values are calculated using as IDS the configuration proposed by scenario 8, since it has shown to has the best performance among the studied data configurations.

Table 6: KTE and RMSE values for each axis and each DFM for the slow-range profile experiment. RMSE errors are presented in degrees.

	BNO	Madgwick	Mahony	CF	MEKF
KTE Yaw	2,96	1,85	2,03	1,74	1,75
KTE Roll	1,26	0,83	0,73	1,49	0,92
KTE Pitch	2,20	1,49	1,77	1,44	1,67
Mean KTE	2,14	1,39	1,51	1,54	1,45
RMSE Yaw	2,81	1,51	1,67	1,46	1,44
RMSE Roll	1,06	0,74	0,63	1,40	0,77
RMSE Pitch	1,85	1,25	1,49	1,25	1,37
Mean RMSE	1,91	1,17	1,26	1,37	1,20

Comparing the system performance presented in Table 6 with those of commercial modules illustrated in Table 1, it is not straightforward, because there is not a clear definition of “dynamic performance”.

Disregarding the factors just mentioned, if one may consider that the slow-range profile represents sufficiently well dynamic movements, then, it is possible to argue that the RIMU system had performance similar to the Mti-3 [76], AHRS380ZA [79], AHRS-8 [81] and VN100 Rugged [83].

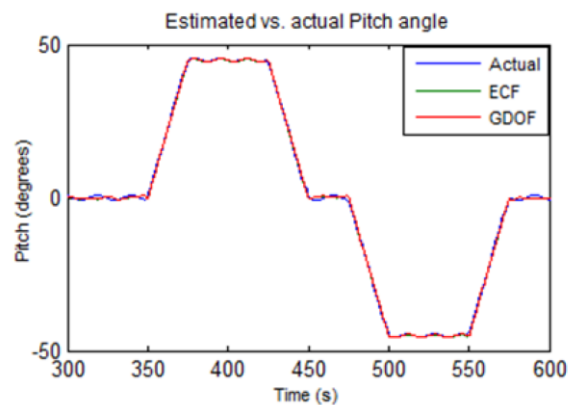


Figure 21: Pitch estimation by the system proposed by Alam et al. (Source: Alam et al. 2014 [58]).

Alam et al. [58] reach lower levels of RMSE noise, in their best case the RMSE values were as low as 0.54° for pitch and roll. Although, Alam et al. used a set of artificial data computationally

generated and simulated with much slower movements as it is illustrated in Figure 21. The relative slower movements profile also reflects in the best values of Beta and Kp for the Mahony's and Madgwick's algorithms, which are, respectively, 0.281 and 0.044 versus 2.630 and 0.210 found at this dissertation for the slow-range profile experiment.

4.2.2 Mid-range profile experiment

With the objective to analyze the system response when it is excited by faster movements (in relation to the ones presented in Section 4.2.1), a second experiment was executed. With the main characteristic of a mean angular speed equals to 44.38 degrees per second (against 13.45 of the previous section), it was named as mid-range profile experiment.

The methodology through this section is the same as the one used in the previous one (Section 4.2.1), so it is the methodology used to present the results.

Table 7 resumes the DFM performance according to the same scenarios proposed in 4.2.1, again the best input data configuration is that one provided by scenario 8. Figure 22 presents the DFMs performance as function of the coefficients values. Similarly to the slow-range profile, the CF demonstrated to be the most critical to tune, while the Mahony's Algorithm is still being the less critical.

Table 7: Best-case filter parameter according to the input data scenario for the mid-range movement profile.

Scenario	CF		Mahony		Madgwick	
	Crossover	KTE	Kp	KTE	Beta	KTE
1	0.990	3.448	0.280	3.218	0.050	3.353
2	0.987	3.577	1.180	3.282	0.070	3.369
3	0.990	3.452	1.640	3.133	0.200	3.249
4	0.987	3.410	0.490	3.080	0.020	3.156
5	0.987	3.738	2.370	3.211	0.120	3.347
6	0.987	3.234	0.990	3.043	0.060	2.995
7	0.987	3.394	1.530	2.842	0.120	2.893
8	0.987	3.205	1.720	2.782	0.100	2.757

Figure 23 displays the DFMs outputs in a manner similar to Figure 18, but now for the mid-range experiment¹⁰. With the increase of mean angular speed, a DFM characteristic plays an important role in its final performance: the phase response. Figure 24 presents a zoom in of the orange zone in Figure 23, it is possible to observe a lag between the DFMs response and the TJ reference. Such lag imposes errors on all methods, but it is most prominent for the BNO estimation reaching errors up to almost 18° for the referred region.

¹⁰ Mid-range experiment video: <https://youtu.be/wQQRgsb8XQM>, uploaded at 15/08/2018.

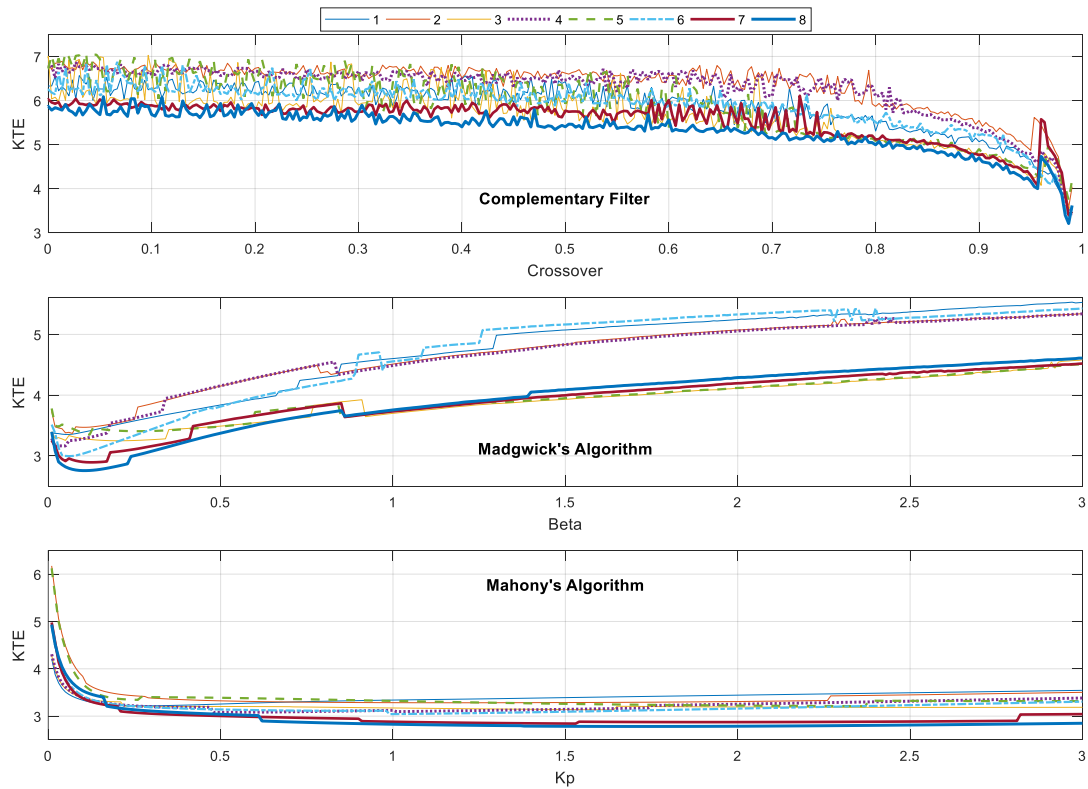


Figure 22: Kinematic Tracking Error as function of each optimizable parameter for their respective input data scenarios (1 to 8) for the mid-range profile.

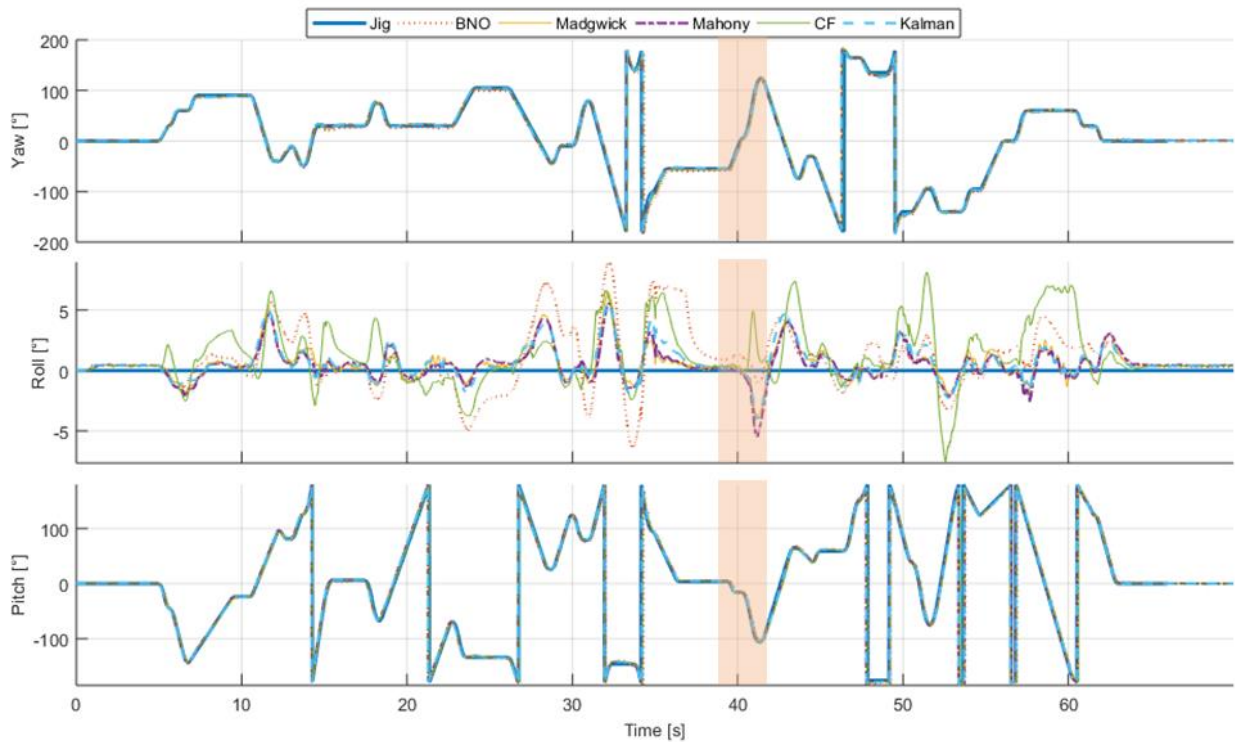


Figure 23: DFM performances for the mid-range motion profile using as input the data composition according to scenario 8. Orange zone is zoomed-in and exhibited in Figure 24. Euler angles represented in the zxy rotation order.

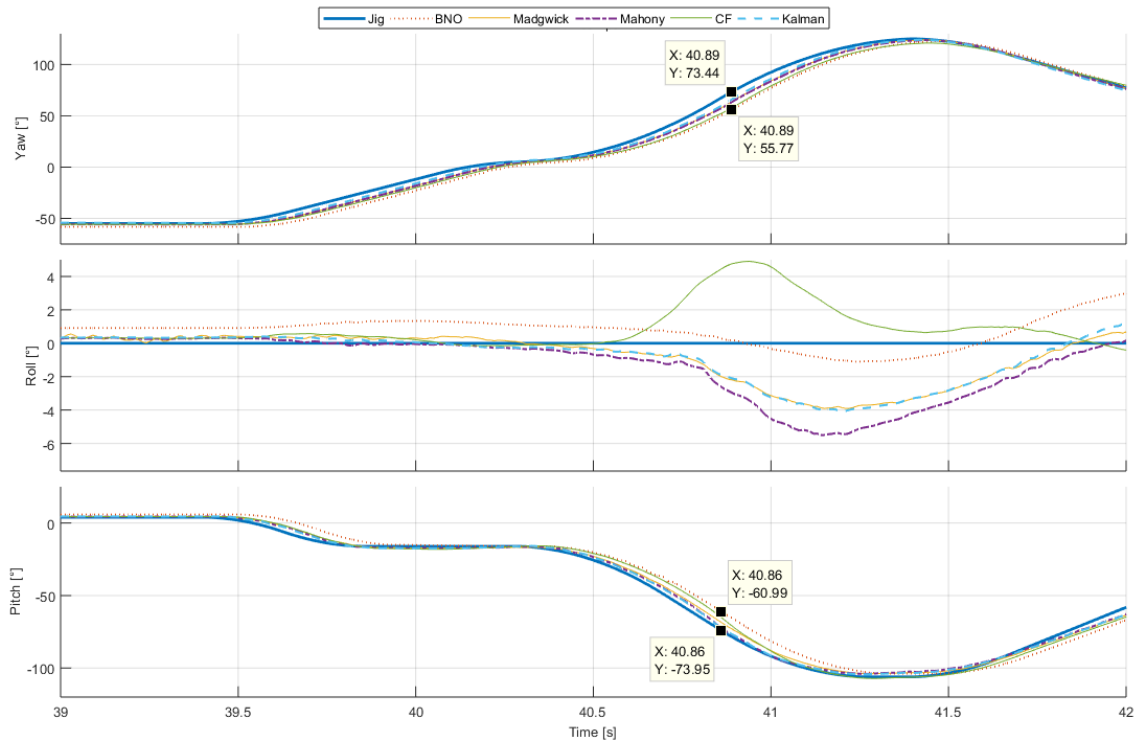


Figure 24: Zoom of orange zone exhibited in Figure 23. In detail the difference between the TJ's reference (solid blue) and the BNO (orange dashed) estimation during TJ rotation.

The time synchronization phase described in 3.3.3 is not capable of completely remove the errors caused by the filter response because the DFM phase response is not constant over the angular speed range. In the best-case scenario, the time synchronization phase may be able to remove the mean lag caused by the DFM phase response.

Different applications are influenced differently by a lag caused by the phase response. For instance, Gait Analysis applications may not be heavily impacted by a lag because the main interest of such application is to estimate the angles between joints, or sensors. Considering that all sensors have approximately the same lag, the error vanishes.

However, for applications which have as main interest translations instead of rotations, in other words, the final output may be a location (position) in a Cartesian plane, the phase response may play an important role in the final estimation error.

It is important to mention that no reference to phase response was found in any commercial AHRS datasheet or brochure during the literature review.

Figure 25 presents the DFMs deviations using as reference the TJ orientation, while Figure 26 exhibits the errors distributions in a boxplot form. It is clear that the peak error values for all DFMs have increased when compared to the slow-range profile. Such fact is attributed to the increase of maximum angular speed, associated with wider rotation angles and non-constant phase response.

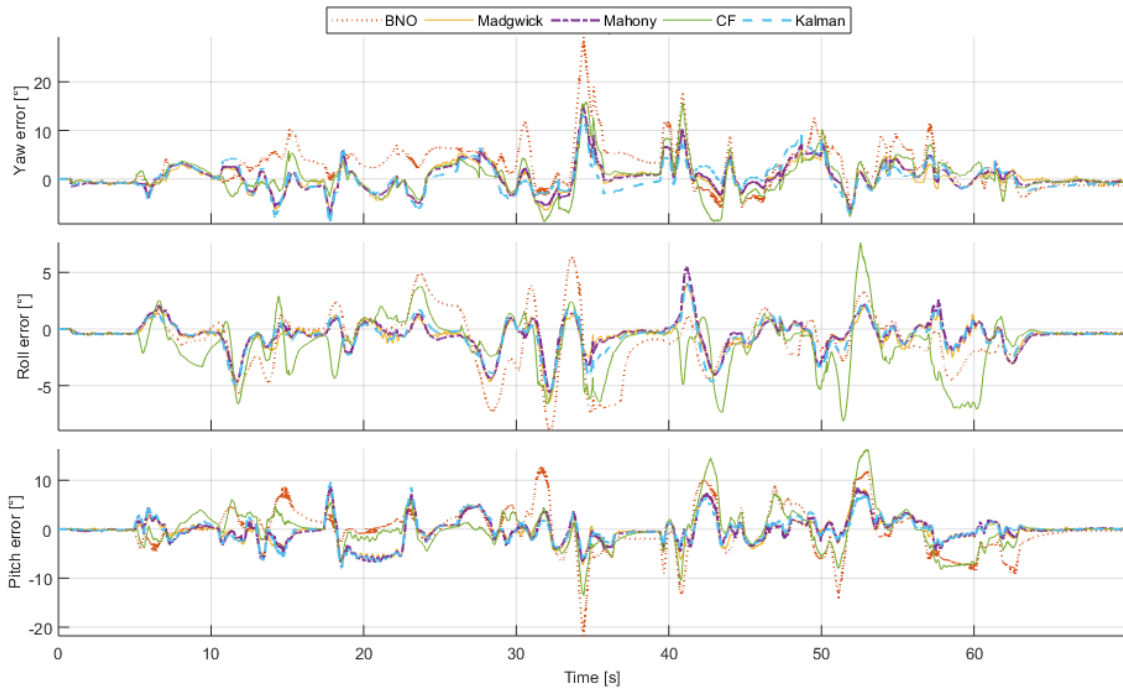


Figure 25: Deviations from the reference for each DFM for the mid-range motion profile using as input the data composition according to scenario 8.

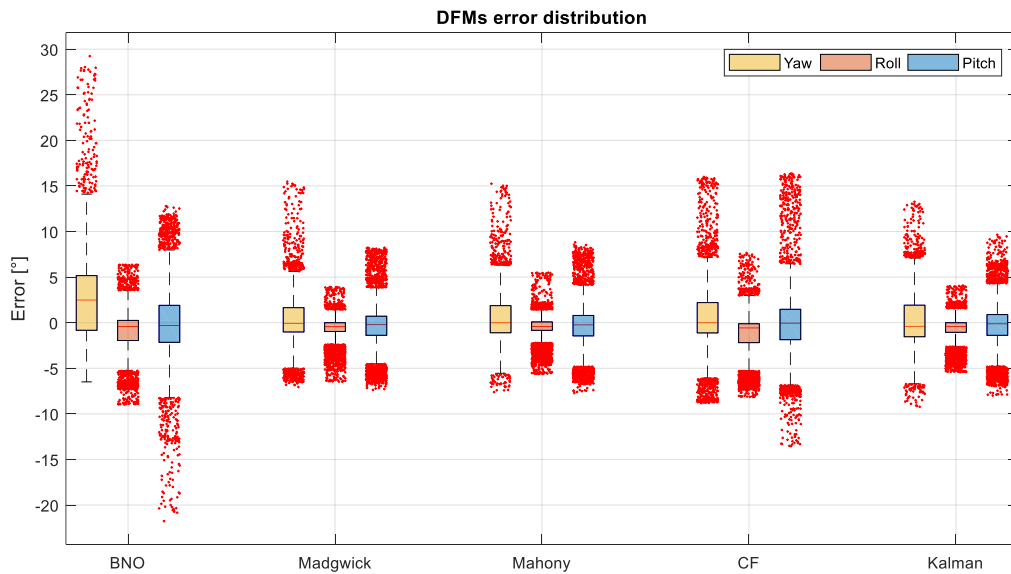


Figure 26: Boxplot of error distribution for each DFM axis considering the mid-range profile as IDS. A total of 7000 samples are represented in each axis of each DFM.

Table 8 exhibits the KTE and RMSE for each axis as well as their mean values. The presented values are calculated using as IDS the configuration proposed in scenario 8, the best-found coefficient values were also used.

Comparing the values of Table 8 with those of Table 6, it is possible to notice that the mean errors (KTE and RMSE) have almost doubled for an experiment that has nearly three times larger mean

angular speed. Again, the performance comparison between the RIMU and commercial systems presented in Table 1 is not straightforward, but if one considers that the “dynamic test” of commercial systems is equivalent to the mid-range profile experiment, then, it is possible to conclude that the RIMU system has performance approximately two times worse than those of most commercial systems listed in Table 1.

Table 8: KTE and RMSE values for each axis and each DFM for the mid-range profile experiment. RMSE errors are presented in degrees.

	BNO	Madgwick	Mahony	CF	MEKF
KTE Yaw	5.87	3.48	3.55	3.49	3.70
KTE Roll	3.06	1.63	1.63	2.41	1.71
KTE Pitch	5.34	3.17	3.17	3.71	3.16
Mean KTE	4.76	2.76	2.78	3.21	2.85
RMS Yaw	5.22	2.85	2.89	2.87	2.96
RMS Roll	2.62	1.43	1.40	2.14	1.49
RMS Pitch	4.37	2.63	2.61	3.12	2.60
Mean RMES	4.07	2.30	2.30	2.71	2.35

4.2.3 Fast-range profile experiment

One last experiment aiming to analyze the RIMU system performance over even higher mean angular speed has been performed and named fast-range profile. It has the setup similar to the slow and mid-range profile, but with a relevant difference: the mean angular speed for this experiment is equal to 66.72 degrees per second, approximately 5 and 1.5 times, respectively, those of the slow and mid-range profiles.

Table 9 shows the DFM performance according to the same scenarios proposed in 4.2.1, the best input data configuration for the Mahony’s and Madgwick’s Algorithms is the one provided by the scenario 8, however, for this specific experiment, the CF had a slightly better performance for the IDS proposed in scenario 4.

Table 9: Best-case filter parameter according to the input data scenario for the Fast-range movement profile.

Scenario	CF		Mahony		Madgwick	
	Crossover	KTE	Kp	KTE	Beta	KTE
1	0.990	4.509	0.090	3.871	0.010	3.992
2	0.983	4.951	2.070	4.526	0.170	4.328
3	0.990	4.473	0.100	3.893	0.010	3.911
4	0.990	3.958	0.330	3.875	0.050	3.972
5	0.983	5.235	3.000	4.758	0.280	4.533
6	0.990	3.933	0.660	3.914	0.070	3.863
7	0.987	4.339	1.660	3.936	0.140	3.738
8	0.990	4.080	1.220	3.790	0.120	3.610

Comparing Tables 5, 7 and 9 is possible to notice that the Crossover factor consistently increases along with the mean angular speed of each experiment. Such fact is not observed in the optimization coefficients (Kp and Beta) of the Mahony's and Madgwick's Algorithms. Table 10 presents the best-found coefficients for the MEKF found after the GA optimization phase for each movement profile. It is also not possible to draw a general evolutionary scenario for the MEKF coefficients.

Table 10: Kalman Filter coefficients reached during the GA optimization for each experiment.

	X_1	X_2	X_3	X_4	X_5	X_6
Slow	0,0482	0,1099	5,81E-03	7,80E-03	6,82E-03	1,01E-06
Mid	0,0587	0,7571	5,18E-03	9,47E-03	9,56E-04	1,28E-06
Fast	0,0629	0,1110	6,60E-03	5,61E-03	1,01E-03	3,80E-06

Figure 27 presents the DFMs performance as a function of the coefficients values. The plots of Madgwick's and Mahony's Algorithm performance have an elevated number of discontinuities, what might be an indicator of the high criticality of the time synchronization stage. As has been demonstrated to the mid-range profile, the phase response of each DFM plays a major role in the final error performance of each DFM.

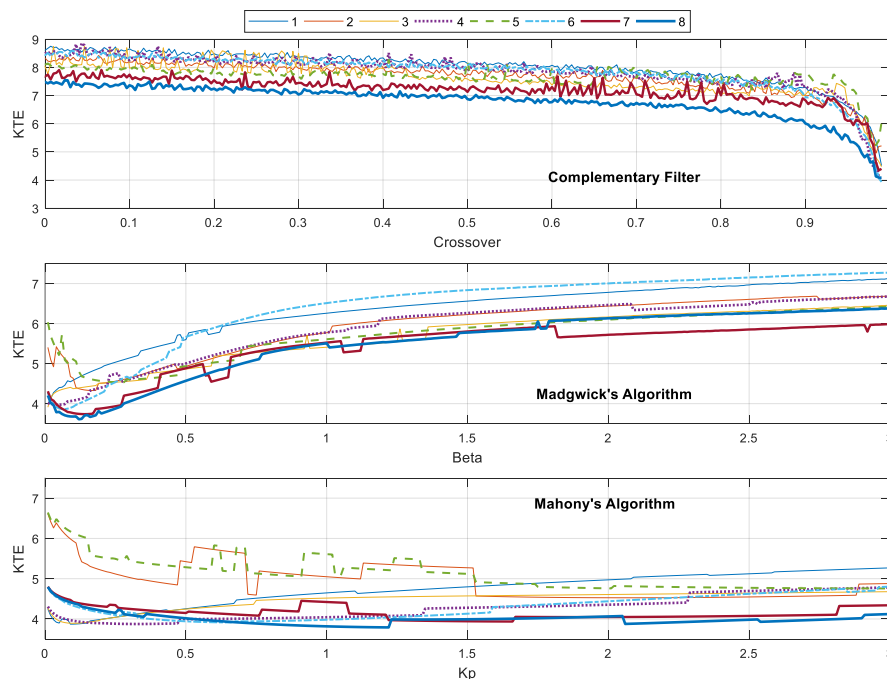


Figure 27: Kinematic Tracking Error as function of each optimizable parameter for their respective input data scenarios (1 to 8) using as IDS the fast-range profile.

Figure 28 presents the DFM orientation estimation for the fast-range profile experiment¹¹, using as IDS the configuration proposed in scenario 8. Figure 29 presents the deviations of each DFM

¹¹ Fast-range experiment video: <https://youtu.be/s53OG844FJ8>, uploaded at 15/08/2018.

estimation from the reference TJ. Figure 30 exhibits the boxplot of the deviations presented in Figure 29.

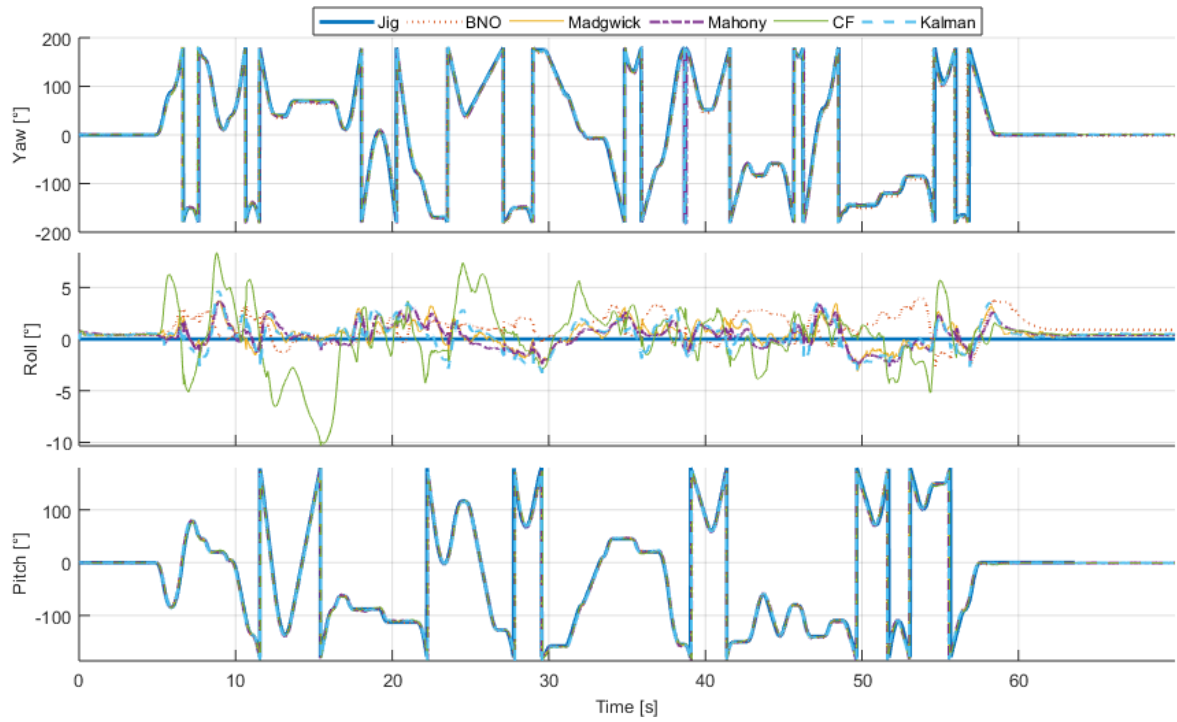


Figure 28: DFM performances for the fast-range motion profile using as input the data composition according to scenario 8. Euler angles represented in the zxy rotation order.

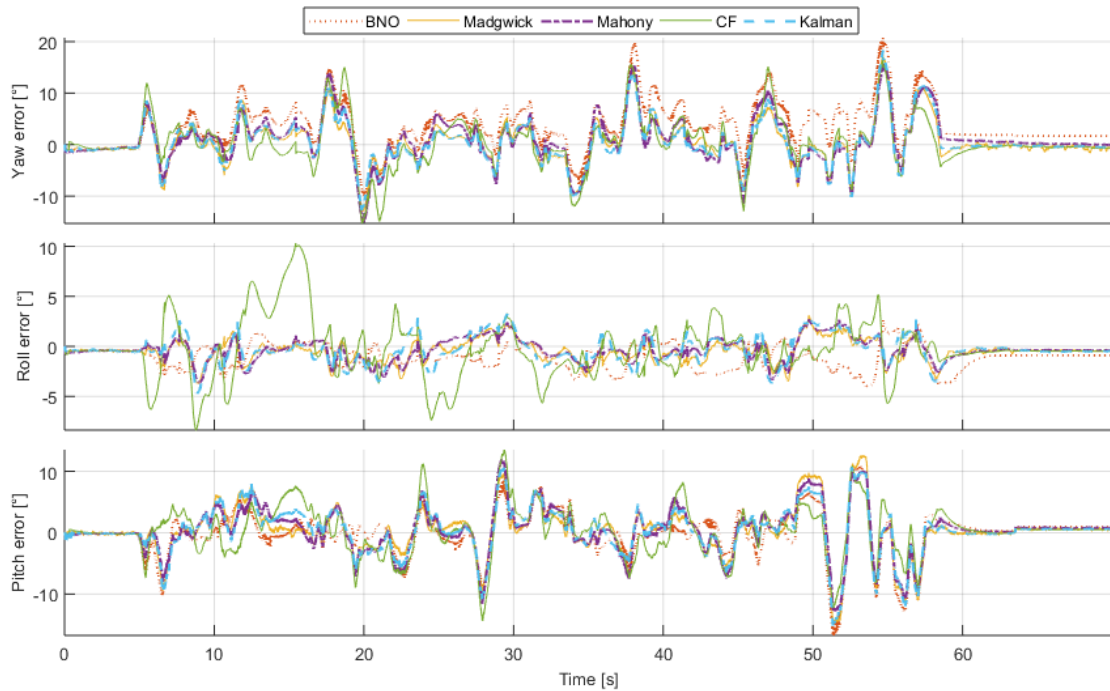


Figure 29: Deviations from the reference for each DFM for the fast-range motion profile using as input the data composition according to scenario 8.

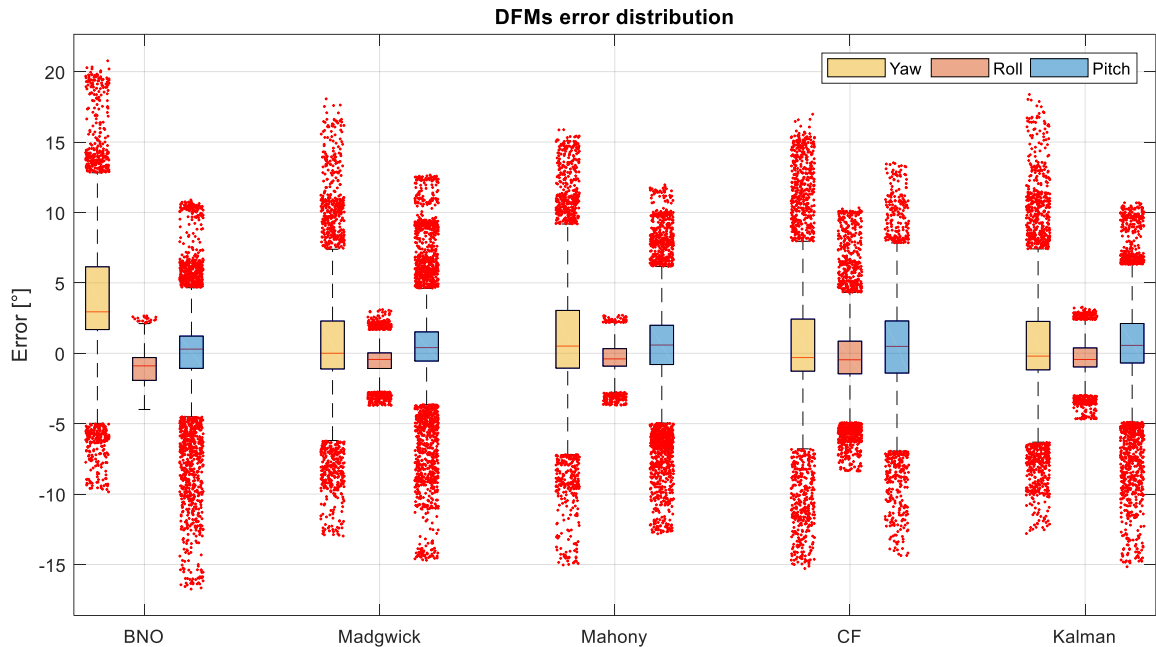


Figure 30: Boxplot of error distribution for each DFM axis considering the fast-range profile as IDS. A total of 7000 samples are represented in each axis of each DFM.

The peak error did not significantly grow in a comparison between the mid and fast-range profile as shown in Figures 29 and 30. Table 11 exhibits the KTE and RMSE for each axis as well as their mean values. The presented values are calculated using as IDS the configuration proposed in scenario 8, the best-found coefficient values were also used. It is possible to conclude that there is a correlation between the DFM error amplitude and the TJ mean angular velocity: increasing the mean angular velocity entails in the increase of the error amplitude.

Table 11: KTE and RMSE values for each axis and each DFM for the fast-range profile experiment, with their optimizable parameters already adjusted, using as IDS the configuration proposed in scenario 8. RMSE errors are presented in degrees.

	BNO	Madgwick	Mahony	CF	MEKF
KTE Yaw	6.46	4.92	5.39	5.03	4.99
KTE Roll	1.73	1.39	1.43	3.04	1.71
KTE Pitch	4.37	4.52	4.55	4.16	4.53
Mean KTE	4.19	3.61	3.79	4.08	3.74
RMS Yaw	5.89	4.10	4.51	4.20	4.16
RMS Roll	1.58	1.17	1.16	2.40	1.37
RMS Pitch	3.68	3.83	3.76	3.41	3.76
Mean RMES	3.71	3.03	3.14	3.36	3.10

4.3 RIMU LONG-TERM STABILITY – DATA FUSION METHODS PERFORMANCE OVER TEMPERATURE VARIATION

As it is broadly referenced, the gyroscopes and accelerometers bias have a correlation with temperature [1], [4], [38], [46], [51]. In an effort to evaluate how the sensors and the DFMs behave during a long-term experiment, along with temperature variation, the following experiment was proposed:

The RIMU was rigidly attached to the glass of a non-moving window with its Y-axis pointing vertically along with the gravity. It is appropriate to mention that the RIMU was at least 1.5 meters far from any power cable. The data acquisition procedure started at 11 PM, during the evening (totalizing 7 hours) the RIMU experienced a small temperature gradient (avg of $-0.25^{\circ}\text{C}/\text{hour}$).

With the sunrise (which is marked as a red line in Figure 31 bottom plot), the RIMU PCB bottom (not the sensors) was directly illuminated by the sunlight for 1.5 hours, such period is highlighted by the bottom plot yellow zone. The sensors experienced then a larger temperature gradient (with a maximum of approximately $18^{\circ}\text{C}/\text{hour}$). After this period, the RIMU was not directly illuminated by the sunlight and the temperature drop until reach a relatively stable point.

The data was collected for a total of 16 hours, which is already four times longer than the data collection length proposed by Nogueira [104] in his thesis, where he also characterizes the inertial sensor thermo-sensitivity.

The gyroscopes and accelerometers readings are exhibited in Figures 31 and 32. Among them, the only sensor that has passed through a calibration procedure is the BNO gyroscope, which calibrates itself whenever the BNO is static. This might be the reason for a practical BNO's gyroscope zero drift during the complete experiment data collection. In an opposite way, the BNO's accelerometer was not calibrated and presented, along with LSM data, a relevant deviation closely correlated with temperature variation.

A pertinent characteristic among the data recorder is that LSM and BNO behave differently to the temperature variation, as can be detected in the first and second plots of Figure 32. Such characteristic may be used to compensate, or at least identify, an eventual drift caused by temperature fluctuation.

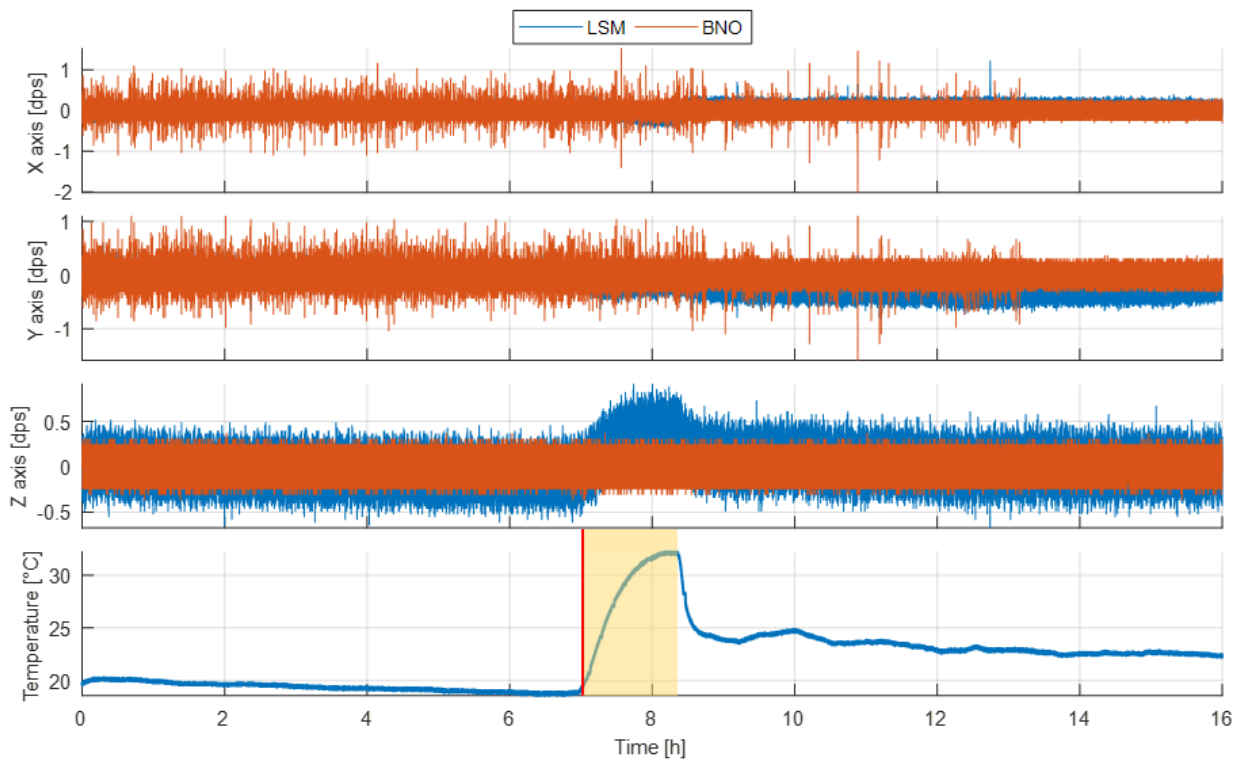


Figure 31: LSM and BNO gyroscopes signals (three first plots) and temperature plot (last graph) during the long-term experiment. The red line indicates the sunrise and the yellow zone the period when the RIMU's bottom side was exposed to direct sunlight.

Figure 33 presents the DFMs orientation estimations for the input data presented by the Scenario 8. The output data was filtered using a 10-second moving average window, which has the aim to remove excessive fluctuations and ease the data comparison.

In an attempt to access and classify the amount of random noise present in the DFMs outputs, the short-term and long-term local average of each orientation estimation was removed using a moving median filter with, respectively, 30-second and 15-minute windows. Such process is similar to the one proposed to remove the baseline wander in electrocardiogram signals [105]. After the aforementioned process, the signal variance was calculated and is exhibited in Table 12. The goal of using two different window sizes is to provide an indicator of the energy of short and long duration random noise.

As can be observed in Figure 33 and in Table 12, the implemented Kalman Filter version has high long-term deviations, behavior that was not demonstrated in the previous experiments on the TJ, as can be noticed, for instance, in Figure 18 and it is evidenced in Figure 19. Notwithstanding, the fluctuations of the implemented Kalman Filter did not diminish even for moving average filters with a window size as long as 100 seconds, contrasting with the others DFM methods. An outstanding performance was obtained by the BNO proprietary fusion algorithm, which has the smallest random noise energy.

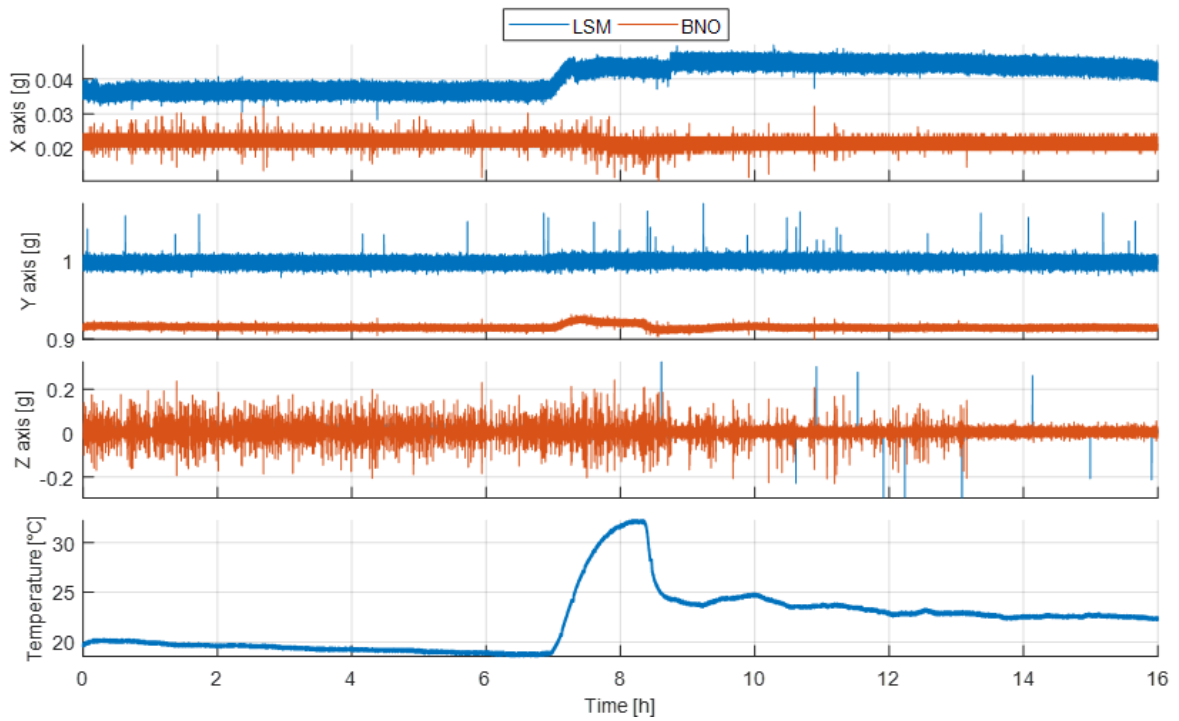


Figure 32: Accelerometers original and uncalibrated data recorded from LSM and BNO confronted against the temperature variation for the long-term experiment.

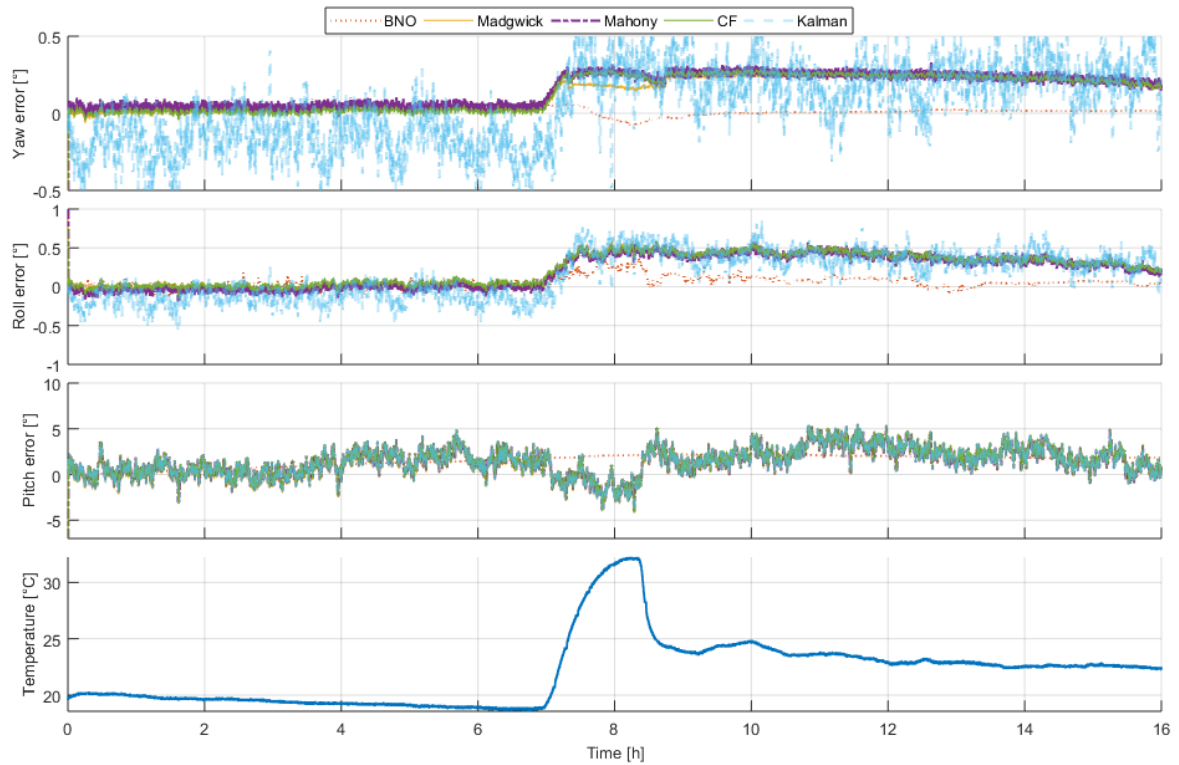


Figure 33: DFM outputs presented after a 10-second moving average window for the long-term experiment. DFM parameters are those selected by the slow-range experiment.

Table 12: Noise energy according to the DFM and the window size. Units in square degrees.

		BNO	Madgwick	Mahony	CF	MEKF
30-second window	Yaw	3.68E-10	1.54E-05	1.78E-06	5.23E-08	5.58E-06
	Roll	1.00E-07	3.74E-05	7.03E-06	4.25E-07	4.07E-06
	Pitch	9.32E-10	4.60E-04	2.62E-04	2.39E-04	2.37E-04
15-minute window	Yaw	1.88E-06	2.11E-05	5.25E-05	6.16E-05	9.86E-03
	Roll	4.81E-04	3.81E-04	3.81E-04	3.76E-04	6.10E-03
	Pitch	6.98E-06	3.29E-01	3.29E-01	3.30E-01	3.29E-01

Considering the average DFM output between the hours 5 and 6 as our reference orientation, and, the average DFM output between the hours 7.5 and 8.5 as our deviated orientation estimation (both cases referred to Figure 33), it is possible to calculate the mean deviation instigated by the temperature variation, that is presented in Table 13. Once more, the BNO had a differentiated performance.

Table 13: Mean orientation deviation due the temperature variation during the long-term experiment. Units in degrees.

	BNO	Madgwick	Mahony	CF	MEKF
Yaw	-0.09	0.15	0.22	0.24	0.41
Roll	0.22	0.43	0.42	0.40	0.58
Pitch	0.67	-2.95	-2.95	-2.98	-2.97

4.4 PERFORMANCE EVALUATION AT EXPOSURE OF FAST MAGNETIC DISTURBANCE

With the purpose of evaluating the magnetometers and DFMs performance in the presence of fast magnetic disturbance caused by an external source, three simple tests were performed:

1. Translate a cell phone (Moto Z2 play) through X and Y axes with a minimum distance of approximately 35 cm.
2. Repeat the last step but for a minimum distance of 5 cm.
3. Translate a 500 VA 220/127 electrical transformer through X and Y axes and return through the same path, with a minimum distance of approximately 5 cm. The setup of this process is illustrated in Figure 34.

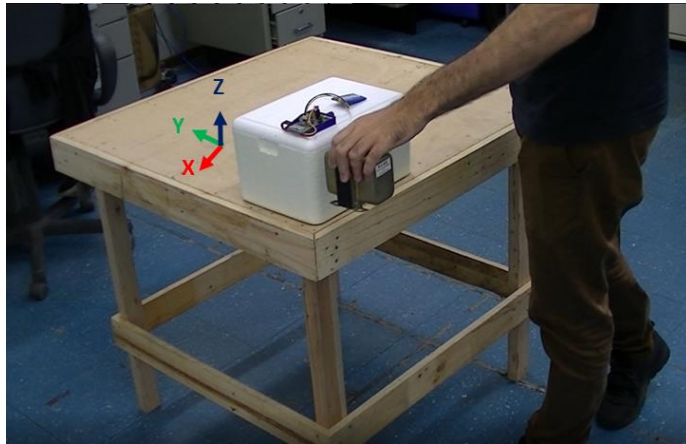


Figure 34: Setup to test the system performance when it is exposed to ferromagnetic materials.

The magnetometer reading, as well as the DFMs outputs, were analyzed and no significant deviation was found for the approximation of the cell phone (first and second tests). However, when the electrical transformer (third test) was the source of magnetic disturbance the magnetometers readings (Figure 35) as well as the orientation estimation of all DFM were affected. Figure 36 exhibits such deviation for the optimizable parameters found in the slow-range experiment, while Figure 37 exhibits the DFM performance when the optimizable parameters found in the mid-range experiment are used. These analyses were performed using as DFM input the data composition described in Scenario 8, according to Section 4.2.1.

The performance exception was the BNO's proprietary algorithm, which has absolutely no deviation during the complete experiment. Such fact creates opportunities to use the BNO as reference during magnetic field distortion events.

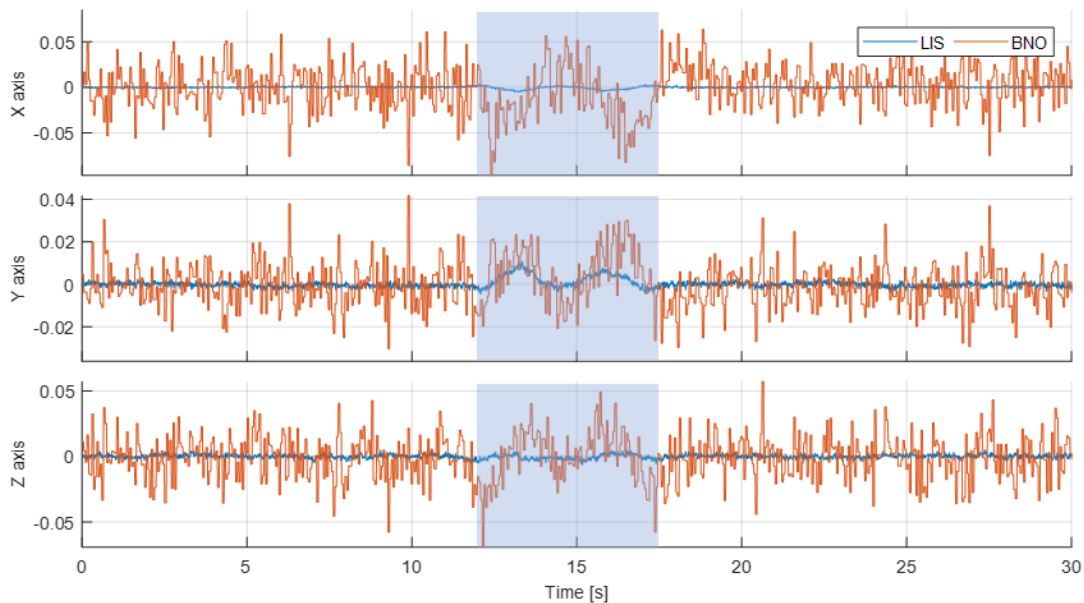


Figure 35: LIS and BNO readings with their mean value removed. The blue zone indicates the time length when the transformer is close to the RIMU board.

From the analysis of Figures 36 and 37, it is possible to conclude that all DFMs were capable to return to the initial orientation estimation after ceasing the influence of the magnetic disturbance. Therefore, it is possible to conclude that this level of magnetic disturbance did not permanently affect the measurements.

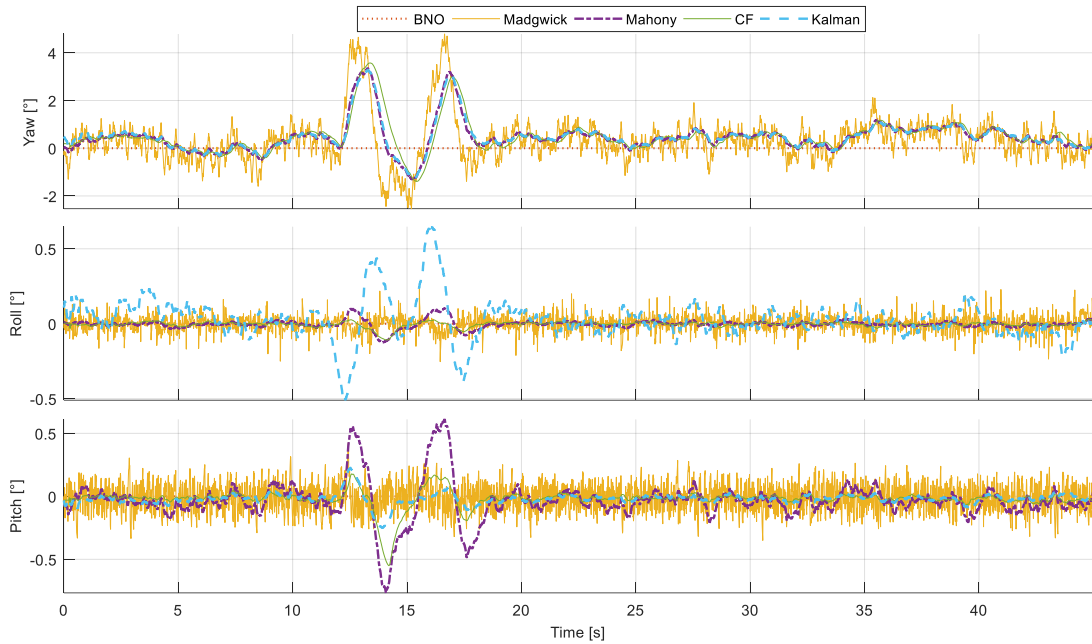


Figure 36: Data Fusion Methods performance while the magnetometers are approximated to a ferromagnetic object. The slow-range (see Section 4.2.1) coefficients are used.

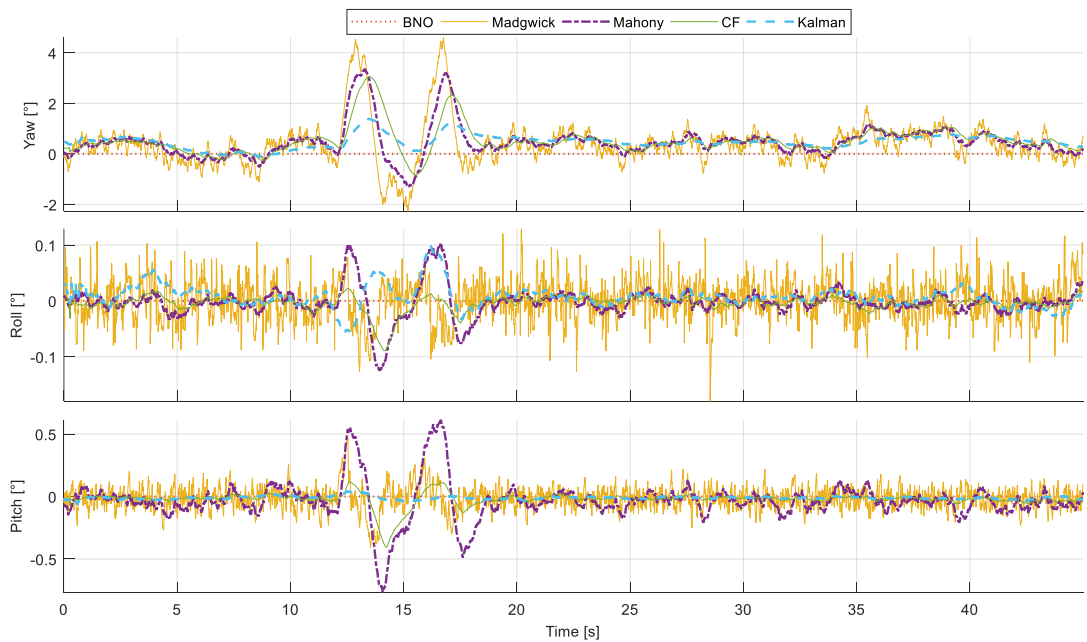


Figure 37: Data Fusion Methods performance while the magnetometers are approximated to a ferromagnetic object. The mid-range (see Section 4.2.2) coefficients are used.

It is also possible to perform a quantitative analysis evaluating, basically, how much each method deviate from the initial zero orientation, based on the results presented in Figures 36 and 37, such analysis is provided in Table 14. It is also relevant to point out the influence of the optimizable parameters over the DFM performance during a magnetic disturbance, as it was briefly discussed in Section 3.3.1.

Table 14: Peak deviation during the magnetometer disturbance experiments for two different DFMs parameters sets. Values are presented in degrees.

		BNO	Madgwick	Mahony	CF	MEKF
Slow-range Parameters	Yaw	0,00	5,14	3,51	3,72	3,43
	Roll	0,00	0,25	0,12	0,11	0,58
	Pitch	0,00	0,44	0,70	0,54	0,26
Mid-range Parameters	Yaw	0,00	4,90	3,51	3,10	1,30
	Roll	0,00	0,18	0,12	0,09	0,08
	Pitch	0,00	0,48	0,70	0,39	0,05

If a DFM is optimized to strongly trust in the accelerometer and magnetometer data, as it is the case for the slow-range set of parameters, this DFM will have its performance severely affected by an eventual magnetic disturbance. Using as an example the implemented MEKF performance, which has the deviation reduce by more than 5 times for pitch and roll estimations, it is possible to conclude that, for at least the implemented MEKF, it is possible to drastically reduce the influence of a magnetic disturbance by correctly choosing the MEKF parameters.

Nevertheless, the Mahony's and Madgwick's algorithms did not have their performance strongly affected by the variation of their optimization coefficients. Furthermore, it is possible to notice that the Mahony's algorithm has the orientation estimation of all axes strongly affected by the magnetic disturbance.

4.5 STATIC DFM PERFORMANCE EVALUATION

In an effort to provide some degree of comparison of this work to others found in the literature, A simple and illustrative experiment, similar to the proposed by Picerno et al. [106] and also performed by Alam et al. [58], Vargas-Valencia [26] and Sánchez [41], was performed.

The setup consists of placing the RIMU over a non-metallic table, far enough from electrical cables and objects that might cause magnetic field distortion, as it is demonstrated in Figure 38. On this table was attached an angle reference that had a resolution of one degree. The BNO was properly calibrated in-locus while the LIS was calibrated using as reference a set of 30 seconds of magnetic data collected prior the experiment.

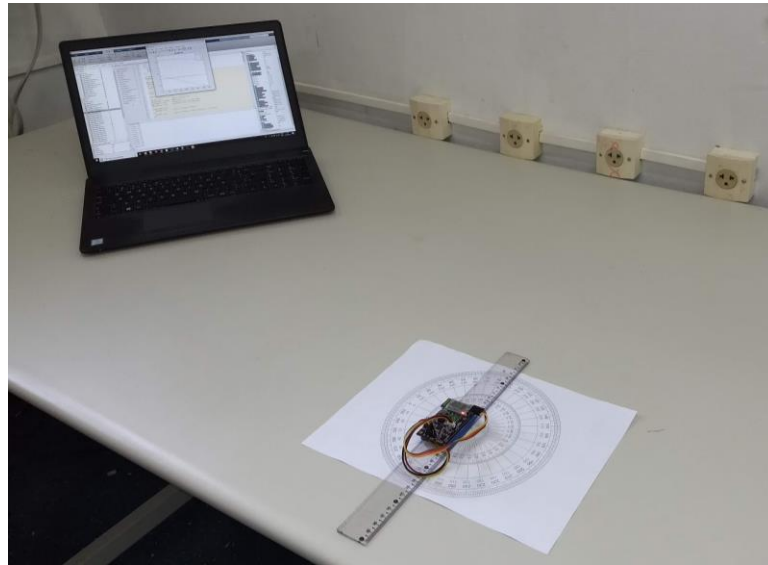


Figure 38: Static perform evaluation experiment setup.

Then, the RIMU was rotated at steps of 10 degrees and left in a stationary position for around 40 seconds, only the last 20 seconds of each position were analyzed. The communication between the RIMU and the server was made through Bluetooth, while the RIMU was powered by the same battery used in all previous experiments.

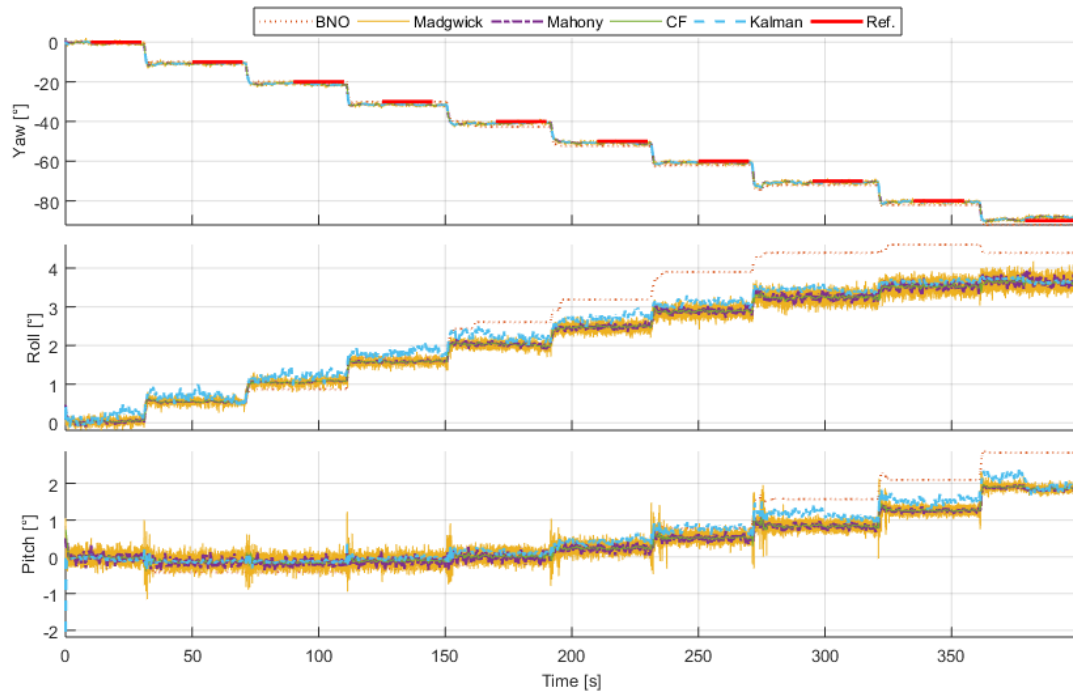


Figure 39: DFMs performance during the Static experiments.

Figure 39 presents the DFM outputs obtained from the data collected during Static Experiment as well as the reference orientation, whereas the Figure 40 presents the angle deviation for each RIMU orientation. It was not possible to assure that neither the table nor the RIMU had no

deviation from the horizontal plane, in this regard, even though all axes are exhibited in Figure 39, only the yaw axis is considered during the error calculation, as it is exhibited in Figure 40. Table 15 resumes the error deviation presenting the KTE and RMSE error for each DFM.

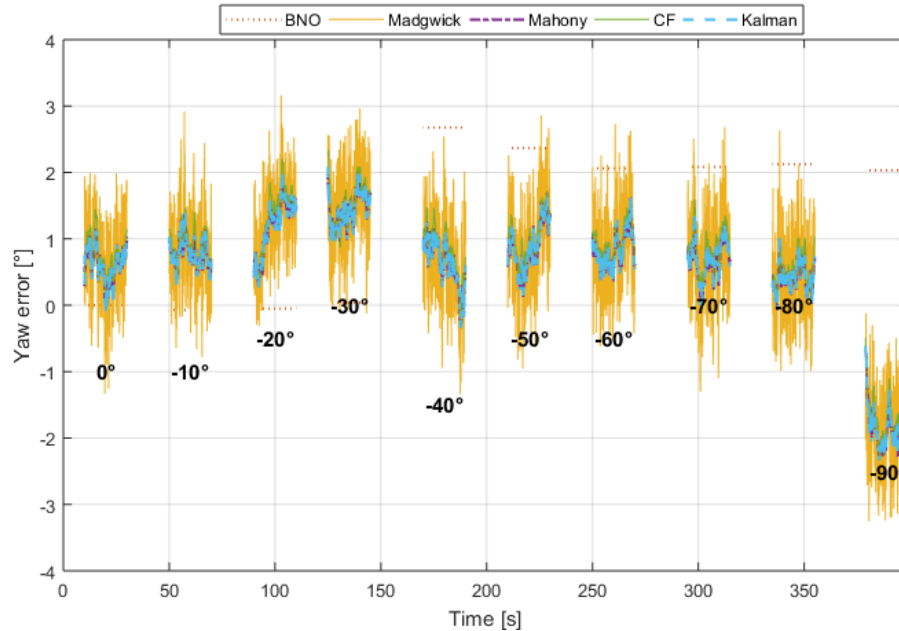


Figure 40: DFMs yaw deviations for each consecutive RIMU orientation. Transition periods are omitted.

Table 15: KTE and RMSE error for the Static experiment. σ stands for error standard deviation.

	BNO	Madgwick	Mahony	CF	MEKF
KTE Yaw	1.75	1.44	1.29	1.36	1.29
RMSE Yaw	1.73	1.19	1.06	1.13	1.05
σ Yaw	1.15	0.97	0.89	0.88	0.81

It is appropriate to mention that it is common, or even expected, that the orientation error in the yaw axis will be greater than those found in the roll and pitch axes, as it can be observed in Table 1 located at Section 2.4. In fact, the analysis of the yaw axis rather than pitch and roll has the objective to provide the worst-case scenario for the Static experiment.

As long as only the results of this experiment are taken into account, the RIMU solution performed better than the MTI-3 (Xsens) [76], STT-IWS (STT) [80], VN100 (VectorNav) [83] and UM7-LT (Redshift Labs) [78]. Moreover, the RIMU had a comparable performance of high-end modules, such as MTI-30 [77] and MTI-300 [4] (Xsens), AHR5380ZA (Acceina) [79] and InertiaCube4 (Intersense) [82], modules that can cost from many hundreds to few thousands of dollars. However, such direct comparison is not feasible once their manufactures do not provide enough (or even none) information about their test routine.

When comes to academic work, Sánchez [41] presented RMSE deviations smaller than one degree for the yaw axis, however the standard deviation found by him was larger than three degrees.

Alam et al. [58] reach lower RMSE, more exactly 0.54° , for their version of Kalman Filter, while Picerno et al. [106] observed mean RMSE among 8 IMUs equals to $2,5^\circ$. But again, it is not that simple to compare the performance of their systems against the one proposed in this dissertation because the final error is dependent of, along with other parameters, the quality of data provided by the inertial and magnetic sensors.

5 CONCLUSIONS AND FUTURE WORK

5.1 CONCLUSIONS

Throughout the First Chapter of this dissertation, a variety of applications involving the use of inertial and magnetic sensors that are developed using the MEMS technology were identified. The strengths of this technology were remarked as well as the reasons that do hamper or even prevent the complete adoption of MEMS systems.

With the objective to understand the issues regarding the use of MEMS systems, Chapter 2 proceeds presenting the mathematical formalism to represent rotation, discussing inclusive the positive and negative aspects of each method. A review of the most used data fusion methods related to the MEMS-IMU scenario is provided, as well as a comparison of the state-of-the-art of commercial MEMS AHRS and MEMS sensors. At the end of Chapter 2, a brief review of the literature that has used sensor redundancy as a mean to improve the system orientation accuracy is presented along with each of their contributions.

The RIMU system is presented in Chapter 3 along with the Test Jig reference system and the complete methodology to classify the performance of the system. Chapter 4 presents the results of an extensive array of experiments, whose aims are to validate the TJ, quantify the influence of the TJ over the RIMU performance and, finally, evaluate the RIMU orientation estimation performance in different configurations and scenarios.

It was identified, throughout the literature review, that a great issue regarding MEMS systems is their high characteristic orientation error. This dissertation proposes three actions to reduce such error: the use of sensor redundancy, which can, alone, reduce the orientation error to values down to 49% of the original error; the study and comparison of different DFMs, which if correctly selected may drastically reduce the orientation error; and, for the last, methods to properly optimize the DFM parameters, what is an essential part of the orientation estimation process, since a set of inappropriate values may lead to an estimation that does not even converge.

Regarding the hypothesis arose in Section 2.5, that indicates the possibility to reduce not only the additive the Gaussian, but also, non-linearity noise when sensors of two different vendors are used to provide the redundancy, this work provides a good indication that such hypothesis is correct. Although a broader analysis, with a larger number of sensors, is still necessary.

Finally, it was possible to observe that the system performance is strongly correlated with the experiment movement profile. Generally speaking, considering the results obtained from the TJ experiments (Section 4.2) the Madgwick algorithm slightly outperformed the others DFMs. When the Quasi-Static experiment is analyzed (Section 4.5) the proposed MEKF has a slightly better accuracy. Conversely, the BNO has performed better during the static (Section 4.3) and the magnetic disturbance experiments (Section 4.4). The presented performance comparison is

restricted to the proposed system (RIMU) and the extension of the results to other sensors may not be simple. However, this dissertation provided indications that the proposed system (RIMU) may perform as well as high-end commercial AHRS.

The proposed system has met the basic requirements that were raised in the beginning of the project and that are part of the Objectives of this M.Sc. dissertation (Section 1.2), such as high sampling rates (for some configurations it has sampling rates of 1kHz, see Section 3.1), reduced size, sensor redundancy and performance improvement over the system with one single inertial sensor. Additionally, the inertial data and the TJ reference is available at the author's Github page¹² for future comparisons, as well as the TJ firmware and the MATLAB scripts that were used to control it and reconstruct its cinematic.

The comparison of the execution time length of each DFM is relevant, however, at this phase, a comparison of this gender would be biased because neither the MEKF nor the CF has its code written in an efficient manner, what would drastically harm the comparison.

5.2 CONTRIBUTIONS

This dissertation has contributed in the areas related to the development of AHRS and those regarding the study of algorithms to fuse inertial and magnetic data, like those DFMs presented throughout the body of this work. In an effort to fairly compare the RIMU performance with that of commercial and academic systems, a two DoF reference system and optimization methods were also developed and implemented, additionally, five relevant DFMs were investigated. It is expected, at this point, that the reader has improved their understanding of the state of the art of IMUs, AHRS and DFMs. Therefore, this dissertation aims also to contribute to the development of systems that perform better in real-world applications, and not only for/during bench applications. Simultaneously, this dissertation details a trustful package of hardware and software which future researchers can use.

5.2.1 Hardware update: FULL RIMU

In an attempt to develop a complete system that would meet user application requirements besides solving the issues of the first RIMU version, a second version, illustrated in Figures 41 and 42, was developed and named FULL RIMU.

¹² <https://github.com/FelipeSchneider> accessed at 20/08/2018.

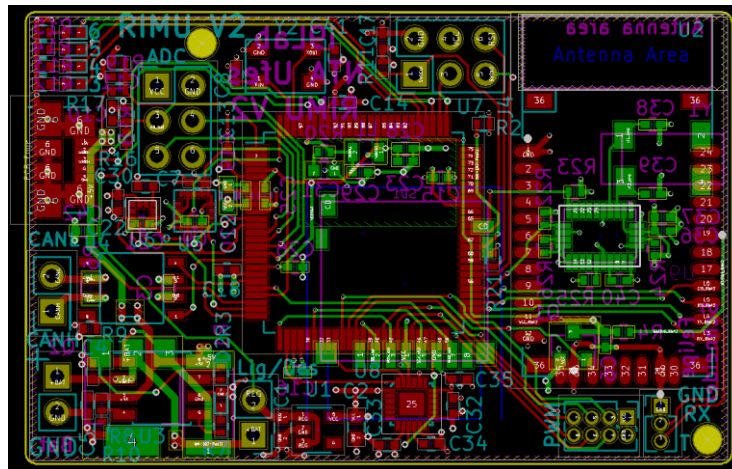


Figure 41: Illustration of the Full RIMU PCB. Top trails are represented in red color while bottom trails are in green. Blue lines represent top silkscreen while bottom silkscreen is in pink. Internal copper layers (second [3.3V] and third [GND]) are hidden.

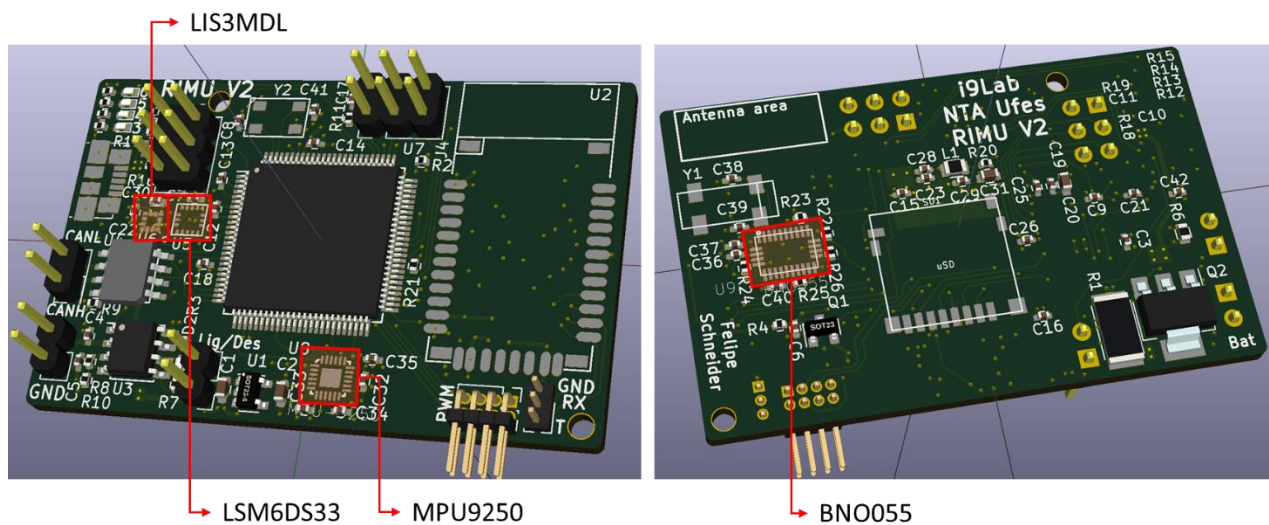


Figure 42: Illustrative 3D model of Full RIMU.

Measuring 51x32mm, this version has as main characteristics:

- The Atmel Cortex M4F SAM4E16E microcontroller selected because of the following key characteristics: dedicated FPU, higher clock frequency (120MHz), dedicated and independent CAN, USB, SPI (3x), I²C, and UART peripherals.
- Three 9 DoF sensors:
 - LSM6DS33 and LIS3MDL (STMicroelectronics), communicating through 10 MHz SPI with a maximum sampling rate of 6.66 kHz (accelerometer).
 - BNO055 (Bosch), communicating through 400 kHz I²C with a maximum sampling rate of 100Hz. BNO along with LSM and LIS preserve the sensing features of RIMU v1 while the adoption of SPI protocol solves the Minimu I²C communication bottleneck.

- MPU9250 (InvenSense) is a 9 DoF SoC that communicates through 20MHz SPI with maximum sampling rate of 32kHz (gyroscope) [46]. This sensor was chosen for its small size, high sampling rate and for being indicated by Winer [107] as the best sensor among the LSM9DS0 (ST Microelectronics), MAX21100 (Maxim) and BMX055 (Bosch).
- Embedded μ SD card.
- Embedded RN-42 Bluetooth 2.0 module (Microchip).
- Battery charger circuit that can automatically switch the power source from USB to the battery, and vice-versa.
- Available auxiliary pins for PWM control and a 12-bit ADC converter.

Due to the time restrictions, it was not possible to solder an example of the second version of the RIMU system. However, the hardware project is complete. The PCB and electronic component cost for a single unit of the FULL RIMU board is approximately 74 USD, more than the double of the first RIMU version (35 USD).

5.2.2 Applications

The RIMU was used as the sensor platform in four different works, all of them with different approaches and objectives.

The first application is presented by Schneider et al. [12] who used the RIMU to improve the assessment of phase durations of a specific test: the Timed Up and Go (TUG), which is usually applied to appraise the motor condition of elderly and the ones who suffer from Parkinson's disease and frequently has as single output the total test duration.

The second application is presented by Leal-Junior et al. [108], who have developed a low cost and highly reliable system for angle measurement based on a sensor fusion between inertial and fiber optic sensors. The system consists of the sensor fusion through Kalman filter of two IMUs and an intensity variation-based polymer optical fiber (POF) curvature sensor. The proposed system was used to measure the knee angle during gait cycles.

The third application is presented by Romero-Laiseca et al. [103], who used the RIMU to measure the angular speed and angular position of an exercise bike's crank arm.

The last, and not yet published application, consisted of estimating relevant parameters (i.e. time-of-flight and dorsal-inclination) of the Counter-Movement Jump, performed by athletes and healthy women. The RIMU was positioned in the lower back of the volunteers and the time-of-flight and peak force, both, estimated by the RIMU were then compared with those estimated by a commercial force-platform.

5.3 PUBLICATIONS

Publication in Peer Reviewed Journals:

- A.G. Leal-Junior, L. Vargas-Valencia, W.M. dos Santos, **F.B.A. Schneider**, A.A.G. Siqueira, M.J. Pontes, A. Frizera “POF-IMU sensor system: A fusion between inertial measurement units and POF sensors for low-cost and highly reliable systems,” *Opt. Fiber Technol.*, vol. 43, no. March, pp. 82–89, 2018.

Publications in conferences proceedings:

- **F.B.A. Schneider**, L.S. Vargas-Valencia, T. F. Bastos-Filho, P. M. Ciarelli, and A. Frizera, “Automated Time Up and Go Test with Redundant IMU System,” in *ENEBI, 6° Encontro Nacional de Engenharia Biomecânica*, 2018, pp. 1–6.
- M.A. Romero-Laiseca, L.A. Pereira da Silva, V.C. Scardua, **F.B.A. Schneider**, L.S. Vargas-Valencia, A. Frizera, T.F. Bastos-Filho. “Software Interface for Online Monitoring of Pedaling on an Exercise Bike,” in *The 6th Brazilian Meeting of Biomechanical Engineering-ENEBI*, 2018.

5.4 FUTURE WORK

The following tasks are indicated as possible future works of this M.Sc. dissertation:

- To solder a FULL RIMU unit.
- To adapt the existent firmware to the FULL RIMU hardware.
- To analyze how the redundancy can be used in the estimation domain, in other words, how the system precision can be improved when orientation estimations are fused.
- To evaluate the relation between computational performance gain and precision degradation because of the use of simplified mathematical operations by the DFMs.
- To develop and implement criteria to evaluate the data corruption level of magnetic and linear acceleration data. For instance, measure if the module of the accelerometer reading is larger than 9.8m/s^2 (or 1g).
- To test the RIMU against gold standard systems when it is used in real world application, i.e. Gait Analysis.
- To implement a sensor network communicating through CAN Bus.

REFERENCES

- [1] V. M. N. Passaro, A. Cuccovillo, L. Vaiani, M. De Carlo, and C. E. Campanella, "Gyroscope Technology and Applications: A Review in the Industrial Perspective," *Sensors*, vol. 17, no. 10, p. 2284, 2017.
- [2] C. C. Yang and Y. L. Hsu, "A review of accelerometry-based wearable motion detectors for physical activity monitoring," *Sensors*, vol. 10, no. 8, pp. 7772–7788, 2010.
- [3] A. Sabato, C. Niezrecki, G. Fortino, and S. M. Ieee, "Wireless MEMS - Based Accelerometer Sensor Boards for Structural Vibration Monitoring : A Review," vol. 17, no. 2, pp. 226–235, 2016.
- [4] Xsens, "MTi 100-series," 2018. [Online]. Available: <https://www.xsens.com/products/mti-100-series/>. [Accessed: 30-Apr-2018].
- [5] Sparton, "AHRS-8," 2018. [Online]. Available: <https://www.spartonnavex.com/product/ahrs-8/>. [Accessed: 26-Apr-2018].
- [6] P. Clausen *et al.*, "Position accuracy with redundant MEMS IMU for road applications," *Eur. J. Navig.*, no. 1, 2015.
- [7] A. Filippeschi, N. Schmitz, M. Miezal, G. Bleser, E. Ruffaldi, and D. Stricker, "Survey of Motion Tracking Methods Based on Inertial Sensors: A Focus on Upper Limb Human Motion," *Sensors*, vol. 17, no. 6, p. 1257, 2017.
- [8] J. B. Bancroft and G. Lachapelle, "Data fusion algorithms for multiple inertial measurement units," *Sensors*, vol. 11, no. 7, pp. 6771–6798, 2011.
- [9] E. Bergamini, G. Ligorio, A. Summa, G. Vannozzi, A. Cappozzo, and A. M. Sabatini, "Estimating orientation using magnetic and inertial sensors and different sensor fusion approaches: Accuracy assessment in manual and locomotion tasks," *Sensors (Switzerland)*, vol. 14, no. 10, pp. 18625–18649, 2014.
- [10] A. Waegli, S. Guerrier, and J. Skaloud, "Redundant MEMS-IMU integrated with GPS for performance assessment in sports," in *Record - IEEE PLANS, Position Location and Navigation Symposium*, 2008, pp. 1260–1268.
- [11] A. Muro-de-la-Herran, B. García-Zapirain, and A. Méndez-Zorrilla, "Gait Analysis Methods: An Overview of Wearable and Non-Wearable Systems, Highlighting Clinical Applications," *Sensors*, vol. 14, no. 2, pp. 3362–3394, Feb. 2014.
- [12] F. B. A. Schneider, L. S. Vargas-Valencia, T. F. Bastos-Filho, P. M. Ciarelli, and A. Frizera, "Automated Time Up and Go Test with Redundant IMU System," in *ENEBI, 6° Encontro Nacional de Engenharia Biomecânica*, 2018, pp. 1–6.
- [13] A. D. Alessandro, R. D. Anna, L. Greco, G. Passafiume, S. Scudero, and S. Speciale, "Monitoring Earthquake through MEMS Sensors (MEMS project) in the town of Acireale (Italy)," pp. 2–5, 2018.
- [14] Dairymaster, "MooMonitor, Health and Fertility Monitor," 2018. [Online]. Available: <http://moomonitor.dairymaster.com/>. [Accessed: 21-Jun-2018].

- [15] E. T. Benser, "Trends in inertial sensors and applications," *Inert. Sensors Syst. (ISSS), 2015 IEEE Int. Symp.*, pp. 1–4, 2015.
- [16] I. Skog, J. O. Nilsson, and P. Handel, "An open-source multi inertial measurement unit (MIMU) platform," *1st IEEE Int. Symp. Inert. Sensors Syst. ISSS 2014 - Proc.*, 2014.
- [17] CTI-Reviews, "Applications of Linear Operators," in *Algebra: Mathematics, Mathematics*, 2nd ed., C. T. Reviews, Ed. Cram101 Textbook Reviews, 2016, p. 74.
- [18] J. Diebel, "Representing Attitude : Euler Angles , Unit Quaternions , and Rotation Vectors," Stanford, California, 2006.
- [19] J. B. Kuipers, *Quaternions and Rotation Sequences: A Primer with Applications to Orbits, Aerospace, and Virtual Reality*. Princeton University Press, 1999.
- [20] N. H. Hughes, "Quaternion to Euler Angle Conversion for Arbitrary Rotation Sequence Using Geometric Methods," Colorado Springs, Colorado, 2009.
- [21] R. L. Pio, "Euler Angle Transformations," *IEEE Trans. Automat. Contr.*, vol. 11, no. 4, pp. 707–715, 1966.
- [22] J. B. Kuipers, "Quaternions and Rotation Sequences," *Geom. Integr. Quantization*, pp. 127–143, 2000.
- [23] GuerrillaCG, *Euler (gimbal lock) Explained*. Youtube, 2009.
- [24] A. J. Hanson, *Visualizing Quaternions: Series in interactive 3D technology*. San Francisco, CA: Morgan Kaufman, 2006.
- [25] J. L. Marins, X. Yun, E. R. Bachmann, R. B. Mcghee, and M. J. Zyda, "An Extended Kalman Filter for Quaternion-Based Orientation Estimation Using MARG Sensors," *Intell. Robot. Syst. 2001. Proceedings. 2001 IEEE/RSJ Int. Conf.*, pp. 2003–2011, 2001.
- [26] L. S. V. Valencia, "Sensor-to-body calibration procedure and definition of anatomical references for Gait analysis based on inertial sensors.," Ufes, 2015.
- [27] L. Vargas-Valencia, A. Elias, E. Rocon, T. Bastos-Filho, and A. Frizera, "An IMU-to-Body Alignment Method Applied to Human Gait Analysis," *Sensors*, vol. 16, no. 12, p. 2090, 2016.
- [28] A. M. Sabatini, "Quaternion-based extended Kalman filter for determining orientation by inertial and magnetic sensing," *IEEE Trans. Biomed. Eng.*, vol. 53, no. 7, pp. 1346–1356, 2006.
- [29] P. I. Corke, "Angdiff code," 2014. [Online]. Available: <https://github.com/petercorke/toolbox-common-matlab/blob/master/angdiff.m>. [Accessed: 09-Jul-2018].
- [30] R. Mahony, T. Hamel, and J.-M. Pflimli, "Nonlinear Complementary Filters on the Special Orthogonal Group," *IEEE Trans. Automat. Contr.*, vol. 53, no. 5, pp. 1203–1218, 2008.
- [31] S. O. H. Madgwick, "An efficient orientation filter for inertial and inertial/magnetic sensor arrays," 2010.
- [32] S. O. H. Madgwick, A. J. L. Harrison, and R. Vaidyanathan, "Estimation of IMU and MARG

- orientation using a gradient descent algorithm,” *2011 IEEE Int. Conf. Rehabil. Robot.*, pp. 1–7, 2011.
- [33] F. L. Markley, Y. Cheng, J. L. Crassidis, and Y. Oshman, “Averaging Quaternions,” *J. Guid. Control. Dyn.*, vol. 30, no. 4, pp. 1193–1197, 2007.
- [34] T. Birdal, “Averaging_Quaternions,” 2015. [Online]. Available: <https://www.mathworks.com/matlabcentral/fileexchange/40098-tolgabirdal-averaging-quaternions>.
- [35] W. F. Phillips, C. E. Hailey, and G. A. Gebert, “A review of attitude kinematics for aircraft flight simulation,” *AIAA 2000-4302 Model. Simul. Technol. Conf.*, no. c, pp. 1–20, 2000.
- [36] J. Lovren, N. Pieper, “Error Analysis of Direction Cosines and Quaternion Parameters Techniques for Aircraft Attitude Determination,” *IEEE Trans. Aerosp. Electron. Syst.*, vol. 34, no. 2, pp. 983–989, 1998.
- [37] C. S. Draper, “Origins of inertial navigation,” *J. Guid. Control. Dyn.*, vol. 4, no. 5, pp. 449–463, 1981.
- [38] XSens, “Gyroscopes Characterization,” 2018. [Online]. Available: https://www.xsens.com/tags/gyroscopes/?gclid=Cj0KCCQjwh7zWBRCiARIsAId9b4rxyWV4Cr4nO648xMXBkcuwiduZ5-OsZPIODKmJsEnt6Tl1VHRNqK0aAnjNEALw_wcB. [Accessed: 16-Apr-2018].
- [39] Engineering360-News-Desk, “Specifying an Accelerometer: Function and Applications,” 2015. [Online]. Available: <https://insights.globalspec.com/article/1263/specifying-an-accelerometer-function-and-applications>. [Accessed: 17-Apr-2018].
- [40] Xsens, “Accelerometers - How to choose your accelerometer?” [Online]. Available: https://www.xsens.com/tags/accelerometers/?gclid=Cj0KCCQjwttbWBRDyARIsAN8zhbLJu5WFqC713kbSAZDCbAx0gy_wwmMrKDGq6VT0h36sHN3lv-pZpXwaAiS9EALw_wcB. [Accessed: 17-Apr-2018].
- [41] M. R. A. Sánchez, “Desenvolvimento de Sensor MARG para Análise de Movimento,” Ufes, 2014.
- [42] A. S. Rosa, “Sistema para análise de marcha online baseado em IMUs,” Ufes, 2017.
- [43] N. F. Ribeiro and C. P. Santos, “Inertial measurement units: A brief state of the art on gait analysis,” in *2017 IEEE 5th Portuguese Meeting on Bioengineering (ENBENG)*, 2017, pp. 1–4.
- [44] Pololu, “MinIMU-9 v5 Gyro, Accelerometer, and Compass (LSM6DS33 and LIS3MDL Carrier).” [Online]. Available: <https://www.pololu.com/product/2738>. [Accessed: 20-Apr-2018].
- [45] Inertial-Labs, “Attitude & Heading Reference Systems key performance,” 2017. [Online]. Available: <https://inertiallabs.com/ahrs.html>. [Accessed: 12-Apr-2018].
- [46] Invensense, “MPU-9250, 9DOF accelerometer, gyroscope and magnetometer.” Datasheet, p. 42, 2016.

- [47] Bosh, “BNO055 Intelligent 9-axis absolute orientation sensor.” Datasheet, p. 105, 2014.
- [48] S. Microelectronics, “LSM9DS1 iNEMO inertial module: 3D accelerometer, 3D gyroscope, 3D magnetometer.” Datasheet, pp. 1–72, 2015.
- [49] STMicroelectronics, “STMicroelectronics Gyroscopes,” 2018. [Online]. Available: http://www.st.com/content/st_com/en/products/mems-and-sensors/gyroscopes.html?querycriteria=productId=SC1288. [Accessed: 18-Apr-2018].
- [50] STMicroelectronics, “STMicroelectronics Accelerometers,” 2018. [Online]. Available: http://www.st.com/content/st_com/en/products/mems-and-sensors/accelerometers.html?querycriteria=productId=SC444. [Accessed: 18-Apr-2018].
- [51] Bosch-Sensortec, “Bosch Sensortec Motion Sensing,” 2018. [Online]. Available: https://www.bosch-sensortec.com/bst/products/motion/overview_motion. [Accessed: 18-Apr-2018].
- [52] InvenSense, “InvenSense Motion,” 2018. [Online]. Available: <https://www.invensense.com/technology/motion/>. [Accessed: 18-Apr-2018].
- [53] Analog Devices, “Analog Devices Accelerometers Portfolio,” 2018. [Online]. Available: <http://www.analog.com/en/parametricsearch/11175>. [Accessed: 18-Apr-2018].
- [54] Analog Devices, “Analog Devices Gyroscopes Portfolio,” 2018. [Online]. Available: <http://www.analog.com/en/parametricsearch/11176>. [Accessed: 18-Apr-2018].
- [55] M. Zamani, J. Trumppf, and R. Mahony, “Nonlinear Attitude Filtering: A Comparison Study.” Cornell University Library, 2015.
- [56] R. Schneider and C. Georgakis, “How to NOT make the extended kalman filter fail,” *Ind. Eng. Chem. Res.*, vol. 52, no. 9, pp. 3354–3362, 2013.
- [57] Acutronics, “Acutronic Motion Simulators,” 2018. [Online]. Available: <http://www.acutronic.com/ch/products.html>. [Accessed: 25-Apr-2018].
- [58] F. Alam, Z. Zhaihe, and H. Jiajia, “A Comparative Analysis of Orientation Estimation Filters using MEMS based IMU,” *Int. Conf. Res. Sci. Eng. Technol.*, pp. 86–91, 2014.
- [59] A. Cavallo *et al.*, “Experimental Comparison of Sensor Fusion Algorithms for Attitude Estimation,” *IFAC World Congr.*, vol. 19, no. 1, pp. 7585–7591, 2014.
- [60] J. L. Crassidis, F. L. Markley, and Y. Cheng, “Survey of Nonlinear Attitude Estimation Methods,” *Journal of Guidance, Control, and Dynamics*, vol. 30, no. 1. pp. 12–28, 2007.
- [61] F. L. Markley, J. Crassidis, and Y. Cheng, “Nonlinear Attitude Filtering Methods,” *AIAA Guidance, Navigation, and Control Conference and Exhibit*. 2005.
- [62] A. Pascoal, I. Kaminer, and P. Oliveira, “Navigation system design using time-varying complementary filters,” *IEEE Trans. Aerosp. Electron. Syst.*, vol. 36, no. 4, pp. 1099–1114, 2000.
- [63] D. Comotti, “9 DoF Orientation Estimation Source Code,” *31/03/2017*, 2017. [Online]. Available: <https://github.com/danicomo/9dof-orientation-estimation>. [Accessed: 24-Jun-

- 2018].
- [64] R. Mahony, T. Hamel, P. Morin, and E. Malis, "Nonlinear complementary filters on the special linear group," *Int. J. Control*, vol. 85, no. 10, pp. 1557–1573, 2012.
 - [65] R. E. Kalman, "A New Approach to Linear Filtering and Prediction Problems," *J. Basic Eng.*, vol. 82, no. 1, p. 35, 1960.
 - [66] B. Friedland, "Kalman Filters: Optimum Observers," in *Control System Design, An Introduction to State-Space Methods*, Mineola, New York: Dover Publications, inc., 2005, pp. 411–469.
 - [67] G. Welch and G. Bishop, "An Introduction to the Kalman Filter," Chapel Hill, TR 95-041, 2006.
 - [68] F. L. Markley, "Attitude Error Representations for Kalman Filtering," *J. Guid. Control. Dyn.*, vol. 26, no. 2, pp. 311–317, 2003.
 - [69] P. Martin, E. Salaün, and Others, "Generalized multiplicative extended Kalman filter for aided attitude and heading reference system," *Proc. AIAA Guid. Navig. Control Conf*, no. August, pp. 1–13, 2010.
 - [70] F. L. L. Markley, "Multiplicative vs . Additive Filtering for Spacecraft Attitude Determination Quaternion estimation," *J. Guid. Control. Dyn.*, vol. 26, no. 2, pp. 311–317, 2003.
 - [71] IEEE, "An extended Kalman filter for quaternion-based orientation estimation using MARG sensors - Citations," 2018. [Online]. Available: <https://ieeexplore.ieee.org/document/976367/citations>. [Accessed: 22-Apr-2018].
 - [72] IEEE, "Quaternion-based extended Kalman filter for determining orientation by inertial and magnetic sensing - Citations," 2018. [Online]. Available: <https://ieeexplore.ieee.org/document/1643403/citations?tabFilter=papers>. [Accessed: 22-Apr-2018].
 - [73] K. Feng *et al.*, "A new quaternion-based kalman filter for real-time attitude estimation using the two-step geometrically-intuitive correction algorithm," *Sensors (Switzerland)*, vol. 17, no. 9, 2017.
 - [74] x-io Technologies, "Open source IMU and AHRS algorithms." xio Technologies, 2012.
 - [75] Technaid, "Tech IMU V4 Series." [Online]. Available: <http://www.technaid.com/products/inertial-measurement-unit-tech-imu-biomechanichs/#!> [Accessed: 24-Apr-2018].
 - [76] Xsens, "Mti 1-series." [Online]. Available: <https://www.xsens.com/products/mti-1-series/>. [Accessed: 24-Apr-2018].
 - [77] Xsens, "MTi 10-series." [Online]. Available: <https://www.xsens.com/products/mti-10-series/>. [Accessed: 28-Apr-2018].
 - [78] Redshift Labs, "UM7-LT Orientation Sensor." [Online]. Available: <https://www.redshiftlabs.com.au/um7-lt-orientation-sensor>. [Accessed: 24-Apr-2018].

- [79] Aceinna, “Aceinna Inertial Systems,” 2018. [Online]. Available: <http://www.aceinna.com/inertial-systems/>. [Accessed: 30-Apr-2018].
- [80] STT-Systems, “STT-IWS High-end wifi IMU for developrs.” [Online]. Available: <https://www.stt-systems.com/products/inertial-motion-capture/stt-iws/>. [Accessed: 24-Apr-2018].
- [81] Sparton, “Sparton Navigation and Exploration - AHRS-8,” 2018. [Online]. Available: <https://www.spartonnavex.com/product/ahrs-8/>. [Accessed: 29-Apr-2018].
- [82] Intersense, “InertiaCube4,” 2018. [Online]. Available: <http://www.intersense.com/pages/18/234>. [Accessed: 01-May-2018].
- [83] Vectornav Embedded Navigation Solutions, “VN-100 Rugged,” 2018. [Online]. Available: <https://www.vectornav.com/products/vn-100/specifications>. [Accessed: 22-Jul-2018].
- [84] Analog Devices, “ADIS16465 Precision MEMS IMU Module,” 2018. [Online]. Available: <http://www.analog.com/en/products/sensors-mems/inertial-measurement-units/adis16465.html#product-overview>. [Accessed: 26-Apr-2018].
- [85] Analog Devices, “ADIS16490 – Tactical Grade, Six Degrees of Freedom Inertial Sensor,” 2018. [Online]. Available: <http://www.analog.com/en/products/sensors-mems/inertial-measurement-units/adis16490.html#product-overview>. [Accessed: 26-Apr-2018].
- [86] ST, “LSM9DS1 iNEMO inertial module, 3D magnetometer, 3D accelerometer, 3D gyroscope, I2C, SPI,” 2018. [Online]. Available: <http://www.st.com/en/mems-and-sensors/lsm9ds1.html>. [Accessed: 29-Apr-2018].
- [87] I. Skog, J. O. Nilsson, and P. Handel, “An open-source multi inertial measurement unit (MIMU) platform,” in *1st IEEE International Symposium on Inertial Sensors and Systems, ISISS 2014 - Proceedings*, 2014, pp. 0–3.
- [88] I2C-Bus, “Clock Stretching,” 2018. [Online]. Available: <https://www.i2c-bus.org/clock-stretching/>. [Accessed: 04-Jun-2018].
- [89] D. A. Winter, *Biomechanics and Motor Control of Human Movement*, 4th ed. 2009.
- [90] A. Benini, A. Mancini, and S. Longhi, “An IMU/UWB/vision-based extended kalman filter for mini-UAV localization in indoor environment using 802.15.4a wireless sensor network,” *J. Intell. Robot. Syst. Theory Appl.*, vol. 70, no. 1–4, pp. 461–476, 2013.
- [91] Allegro-MicroSystems, “A4988 - DMOS Microstepping Driver with Translator And Overcurrent Protection,” 2017. [Online]. Available: https://www.pololu.com/file/0J450/a4988_DMOS_microstepping_driver_with_translator.pdf. [Accessed: 04-Jun-2018].
- [92] R. Condit and D. W. Jones, “Stepping Motors Fundamentals - AN907,” *Microchip Technology*, 2004. [Online]. Available: <http://www.bristolwatch.com/pdf/stepper.pdf>. [Accessed: 10-Jun-2018].
- [93] F. B. A. Schneider, “RIMU-Test-Jig Source code,” 2018. [Online]. Available: https://github.com/FelipeSchneider/Rimu_Test_Jig. [Accessed: 10-Jun-2018].

- [94] V. Maximov, "GyroLib - AHRS Library," 2018. [Online]. Available: <https://la.mathworks.com/matlabcentral/fileexchange/63250-gyrolib-ahrs-library>. [Accessed: 24-Jun-2018].
- [95] J. A. Gallego, E. Rocon, J. O. Roa, J. C. Moreno, and J. L. Pons, "Real-time estimation of pathological tremor parameters from gyroscope data," *Sensors*, vol. 10, no. 3, pp. 2129–2149, 2010.
- [96] L. Eshelman and D. Schaffer, "Real-Coded Genetic Algorithms and Interval-Schemata," *Found. Genet. Algorithms*, vol. 2, pp. 187–202, 1993.
- [97] M. Takahashi and H. Kita, "A crossover operator using independent component analysis for real-coded genetic algorithms," *Proc. 2001 Congr. Evol. Comput. (IEEE Cat. No.01TH8546)*, vol. 1, pp. 643–649, 2001.
- [98] M. Kok, J. D. Hol, and T. B. Schön, "Using Inertial Sensors for Position and Orientation Estimation," *Found. Trends® Signal Process.*, vol. 11, no. 1–2, pp. 1–153, 2017.
- [99] S. Mucciaccia, A. Frizera, and E. Salles, "Algoritmo Direto de Calibração de Magnetômetros Triaxiais por Ajuste de Elipsoide Utilizando Distância Algébrica," in *XXI Congresso Brasileiro de Automática*, 2016, pp. 2884–2889.
- [100] R. Kiebertz, "The step motor--The next advance in control systems," *IEEE Trans. Automat. Contr.*, vol. 9, no. 1, pp. 98–104, 1964.
- [101] K. W. H. Tsui, K. C. W. Yuen, and N. C. Cheung, "Novel Modeling and Damping Technique for Hybrid Stepper Motor," *IEEE Trans. Ind. Electron.*, vol. 56, no. 1, pp. 202–211, 2009.
- [102] ST Microelectronics, "LSM6DS3 iNEMO inertial module : " Datasheet, p. 76, 2017.
- [103] M. A. Romero-Laisecca *et al.*, "Software Interface for Online Monitoring of Pedaling on an Exercise Bike," in *The 6th Brazilian Meeting of Biomechanical Engineering-ENEBI*, 2018.
- [104] S. L. Nogueira, "Sistemas Markovianos para Estimativa de Ângulos Absolutos em Exoesqueletos de," Universidade de São Paulo - USP, 2015.
- [105] W. Hao, Y. Chen, and Y. Xin, "ECG baseline wander correction by mean-median filter and discrete wavelet transform," *Proc. Annu. Int. Conf. IEEE Eng. Med. Biol. Soc. EMBS*, pp. 2712–2715, 2011.
- [106] P. Picerno, A. Cereatti, and A. Cappozzo, "A spot check for assessing static orientation consistency of inertial and magnetic sensing units," *Gait Posture*, vol. 33, no. 3, pp. 373–378, 2011.
- [107] K. Winer, "9 DoF Motion Sensor Bakeoff," 2015. [Online]. Available: <https://github.com/kriswiner/MPU6050/wiki/9-DoF-Motion-Sensor-Bakeoff>. [Accessed: 07-Jun-2018].
- [108] A. G. Leal-Junior *et al.*, "POF-IMU sensor system: A fusion between inertial measurement units and POF sensors for low-cost and highly reliable systems," *Opt. Fiber Technol.*, vol. 43, no. March, pp. 82–89, 2018.